UNIVERSITY OF
BIRMINGHAM

FLEXIBLE BOND WIRE CAPACITIVE STRAIN SENSOR FOR A VEHICLE TYRE

by

Siyang Cao

A thesis submitted to

The University of Birmingham

for the degree of

DOCTOR OF PHILOSOPHY

School of Mechanical Engineering

College of Engineering and Physical Sciences

The University of Birmingham

April 2016

I would like to dedicate my work to my parents for their financial aid and unconditional love and to all my family members for their continuous care and assistance throughout my study. I also would like to dedicate this work to Yuecong Liu for her genuine and endless love, support and belief in my accomplishing this research.

ACKNOWLEDGEMENT

I would like to thank my supervisors, Dr. Carl Anthony and Dr. Oluremi Olatunbosu for their continuous guidance throughout this research.

I would like to thank the technician, Simon Pyatt in the School of Physics for his advice and support in the area of bond wire technology.

I also would like to thank the academic and technical staff in the School of Mechanical Engineering and the School of Physics for their advices and supports.

Finally, I would like to thank my sincere friends and office mates for their encouragement and support throughout this research.

'If I have seen further than others, it is by standing upon the shoulders of giants.'

Isaac Newton

ABBREVIATIONS

ABS	Anti-lock Braking System
BR	poly-Butadiene rubber
FBG	Fibre Bragg Gratings
FEA	Finite Element Analysis
IC	Integrated Circuit
IDT	Interdigital Transducers
LED	Light Emitting Diode
MEMS	Microelectromechanical System
NR	Natural Rubber
PCB	Printed Circuit Board
PCX	Piano-Convex
PDMS	Polydimethylsiloxane
PM-PCF	Polarization-maintaining Photonic Crystal Fibre
PSD	Position Sensitive Detector
PVDF	Polyvinylidene Fluoride
RF	Radio Frequency
RFID	Radio Frequency Identification
SAW	Surface Acoustic wave
SBH	Schottky Barrier Height
SBR	Styrene-Butadiene rubber
SNR	Signal-to-Noise Ratio
TCMS	Tyre condition monitoring system
TCS	Traction control system
TPMS	Tyre pressure monitoring system
VSA	Vehicle stability assist

NOMENCLATURE

Literature review

Fibre Bragg Gratings Sensing

l	the length of the Bragg gratings
n_{eff}	refraction index of the material in the Bragg gratings
T	the temperature of the Bragg gratings
λ_B	wavelength of the reflected light in the Bragg gratings
Λ	the spacing in the Bragg gratings
$\Delta\lambda_B$	the variation of the wavelength of the reflected light in the Bragg gratings
Δl	the variation of the length of the Bragg gratings
ΔT	the variation of the temperature of the Bragg gratings

Surface acoustic Wave Sensing

c	the stiffness constant of the substrate
f_c	the frequency of the propagating wave
v_s	the velocity of the surface acoustic wave
p	the spacing of each two reflectors
ρ	the density of the material of the substrate
$\Delta\phi$	the difference of the phases
ω_0	the frequency of the FM signal
μ	the rate of the modulation
t_1	the delayed time for the first reflector
t_2	the delayed time for the second reflector
$\Delta\tau$	the difference between two delayed times
ε	the strain in surface acoustic wave sensing

Capacitive Strain Sensing

a	the overlapping length of the fingers
b	the width of the fingers
c	the length of the fingers

d the depth of the fingers

C_0 the original capacitance of an interdigital capacitive strain sensor

C_p the parasitic capacitance

C_x the changed capacitance of an interdigital capacitive strain sensor

C_{ref} the capacitance of the reference capacitor

V_{in} the input voltage

V_{out} the output voltage

n the number of finger in one comb sturcture

ε_0 the electric constant

ε the dielectric constant of the material around the structure

Sensor Development

Interdigital Capacitor Design

a the gaps in the interdigital capacitor design

A the area of overlapping of two plates in a typical capacitor

c the overlapping length of the fingers

C the capacitance of a typical capacitor

C_{i0} the original capacitance of the interdigital capacitor design

$C_{i,deflected}$ the capacitance of the interdigital capacitor design under a strain

C_p the parasitic capacitance of the interdigital capacitor design

d the distance between the plates in a typical capacitor

d_f the thickness of the fingers

n the number of fingers in one comb structure

Δx the deflection in x-axis direction

Δy the deflection in y-axis direction

ε_0 the electric constant

ε_r the dielectric constant of the material between the plates in a typical capacitor

ε_{PDMS} the dielectric constant of PDMS

Coplanar Capacitor Design

a the gaps in the coplanar capacitor design

c the overlapping length of the fingers

C_{c0} the original capacitance of the coplanar capacitor design

C_{ci} the capacitance that generated by a pair of coplanar capacitor

$C_{c,deflected}$ the capacitance of the coplanar capacitor design under a strain

$K(k)$ the total elliptic integral of the first kind

k_c the elliptic integral for the coplanar capacitor design

$k_{c,deflected}$ the total elliptic integral of the first kind under a strain

n the number of fingers in one comb structure

w the width of the finger

Δx the deflection in x-axis direction

ε_{PDMS} the dielectric constant of PDMS

ε_0 the electric constant

Bond Wire Capacitor Design

C_a the initial capacitance of bond wire capacitor design

$C_{a,deflected}$ the capacitance of bond wire capacitor design under a strain

C_{aI} the capacitance between the a pair of wires that are equivalent with a coplanar structure

$C_{aI,deflected}$ the capacitance between the a pair of wires that are equivalent with a coplanar structure under a strain

C_E the total capacitance of a pair of wires

$C_{E,deflected}$ the total capacitance of a pair of wires under a strain

h the bond height

k the ratio of r_1 and r_2

k_a the elliptic integral for the bond wire capacitor design

$k_{a,deflected}$ the elliptic integral for the bond wire capacitor design under a strain

l the bond length of the wire

L the length of the wire

m half of the distance between two equivalent line charges

N the number of wires in an wire array

q the charge that carried by a wire

r	the radius of the bond wire
r_1	the distance from a point to the left line charge
r_2	the distance from a point to the right line charge
R	the radius of the wire loop
s	the distance between two wires
V	the voltage between the wires
ϕ_{left}	the potential of the left wire
ϕ_{right}	the potential of the right wire
Δx	the deflection in x-axis direction
Δx_i	the deflection between each pair of wire in x-axis direction
ε_{PDMS}	the dielectric constant of PDMS
ε_0	the electric constant
ε_{strain}	the strain

Fabrication Process

W_i	the designed width before wet etching
W_f	the actual width after wet etching
D	the etching depth
U	the undercut of wet etching

Measurements and Calibrations of the Strain Sensor

Bending test on a rod

l_w	the length of the strain sensor
Δl_w	the increased length due to the bending on the rod
R_r	the radius of the rod
h	the height of the strain sensor
ε_{bend}	the strain that generated by bending the sensor on the rod

Cantilever test

D_y	the deflection of the cantilever in y-axis direction
E_c	the Young's Modulus of the cantilever
F	the force at the free end of the cantilever

F_x	the force at the free end of the cantilever in x-axis direction
F_y	the force at the free end of the cantilever in y-axis direction
l_c	the length of the cantilever
I_x	the moments of inertia of the cantilever cross section in x-axis direction
I_y	the moments of inertia of the cantilever cross section in y-axis direction
t	the thickness of the cantilever
x	the x coordinate for the point on the surface of the cantilever
y	the y coordinate for the point on the surface of the cantilever
z	the z coordinate for the point on the surface of the cantilever
σ_z	the stress at the sensor position
ε_z	the strain at the sensor position

LIST OF FIGURES

LIST OF TABLES

TABLE OF CONTENTS

Abstract

This thesis reports a novel flexible wire bond structured capacitive sensor design that can measure the strain in the tyres stably and reliably without any influence or disturbance to the tyre material during the measurement. An industry achievable fabrication method based on the design has been also investigated and it is also believed that there is a possibility of introducing the sensor into mass production.

Bond wire technology, laser machining technology and photolithography technology are adopted to fabricate the strain sensor, in which the wire bonding technology is the most significant process for this design. An array of 25 micrometer bond wires that are normally employed for electrical connections in integrated circuits is built to create an interdigitated structure and generating approximately 10pF capacitance. The array that in an approximately 8*8 mm area consists of 50 wire loops and creates 49 capacitor pairs. The aluminium wires are bonded to a flexible PCB which is specially finished to allow direct bonding to copper surface. The wire array is finally packaged and embedded in a flexible and compliant material, polydimethylsiloxane (PDMS), which acts as the structural material that is strained. The implementations of the bond wire, the flexible PCB and PDMS embedding minimize the stiffness of the strain sensor while the PDMS can also prevent the sensor from any potential damage. When a tensile strain occurs, the wires are stretched further apart reducing the capacitance. On the contrary, the wires move closer and increase the capacitance if the strain sensor is compressed. Different from the traditional interdigital capacitor, the capacitance of

the device is almost in a linear relationship with respect to the strain, which can measure the strain up to at least ±60000 micro-strain (±6%) with the resolution of 111 micro-strain (0.01%).

Chapter 1.
Introduction

1.1 Background

The earliest pneumatic tyre was invented by John Boyd Dunlop in 1888, which initially prevented the noise of the wheels when riding on rough roads. With the development of pneumatic tyres, it has been widely employed in different transportation industries, such as the automobile industry and aerospace industry. It is stated that approximately 60% goods in the world are transported by vehicles that move on rubber tyres [1]. The production of the tyre in Europe was approximately 4.5 million tonnes in 2010 and is keeping increasing in a steady growth rate [2]. The demands of a safe and comfortable driving experience and the requirement of the emission from the vehicles are the catalysts for promoting the development of the tyre industry and tyre research. There were a variety of systems developed that aims at different functions, such as anti-lock braking system (ABS), which prevents the wheels from locking up and avoid skidding of the vehicle, tyre pressure monitoring system (TPMS)/tyre condition monitoring system (TCMS), which detects the pressure in a pneumatic tyre to warn the driver at deflated condition and control the tyre rolling resistance for reducing fuel consumption and the emissions.

The concept of the 'intelligent tyre' emerged as the demands of industry and research groups in tyre technology. By installing different sensors in the tyre, it aims at directly measuring and detecting the physical quantities (such as tyre pressure, temperature in tyres, friction between the tyre and road and strains in tyres) of the tyres and analyzing the information between the

tyre and road [3], which can direct the behaviour of the drivers and finally improves the safety and driving experience, increasing the durability of the tyres, controlling the fuel consumption and reducing the emissions. Additionally, many integrated systems, such as wireless transmitting system and energy harvesting systems, were developed and introduced into the 'intelligent tyre'.

Among these physical quantities that the 'intelligent tyre' detects, the friction force between the surfaces of the tyre and road is one of the most significant physical quantities for the tyre behaviour and plays an important role for vehicle simulation, manoeuvrability of the vehicle and safety of the driving experience [4]. Several models for calculating and analyzing the friction have been developed, such as slip/force model, lumped model and distributed model [5]. Meanwhile, finite element analysis (FEA) software has also been employed for simulating friction based on these models by many researchers [6-8]. However, the friction between the surfaces of tyre and road are affected by many factors, such as the environmental characteristics, the inflation of the tyre, the load of the tyre and are difficult to be measured directly [4]. Alternatively, the strain of the tyre is associated with the friction and has become another possible approach to investigate the friction between the surfaces of the tyre and road [8, 9]. By measuring the strain in tyres, the friction coefficient can be estimated, which provides critical information for anti-lock braking systems or other advanced active safety systems such as traction control systems (TCS) and vehicle stability assist (VSA) [9] and finally controls the fuel consumption, reduces the emissions and prevents extreme accidents.

Different from the friction, the strain or the deformation of a tyre is possible to be measured directly by attaching a strain sensor on the inner surface of the tyre. So, the foiled strain sensor, which is normally used for measuring the strain of metallic and concrete materials, was employed. However, compared with the tyre rubber, the foiled strain sensor has higher stiffness, so it will inevitable have a significant effect on the strain behaviour of the sensing surface of the tyre. The actual strain of the tyre then can hardly measure accurately and reliably. To avoid the high stiffness that might be brought by the commercial strain sensors, there have been several novel strain sensors developed that are specially for measuring the deformation/strain in the tyres, which will be introduced in the literature review in Section 2.3.6. Although these sensing technologies can measure the strain in the tyres, there exists some deficiencies in each design. Meanwhile, there was no development of these strain sensor in recent years. The stiffness of the sensor is still one of the main problems, which always can result unstable and unreliable measurements. A fully flexible and complaint sensor is extremely important for measuring the strain in tyres precisely. Additionally, the maximum strain in some extreme conditions, which might up to approximately 4% (40000 micro-strain) [10], exceeds measuring range of most of the commercial strain sensor. Fabrication and installation process are also desired to be simplified and possible to be adopted by the existed manufacturing systems. What is more, because the strain sensor is enclosed in a wheel when measuring the strain, the sensor has to be capable of being integrated with a wireless transmitting system. In addition, as a soft substrate, the strain behaviour of the tyre rubber may also be influenced by the bonding materials while the adhesive bonding method in most of research has not been clearly stated and explained.

1.2 Objectives

By considering the demand and importance of measuring the strain in the tyres and the deficiencies of the current research on the tyre strain sensing technologies, this study will develop a novel strain sensor that has sufficient small stiffness compared with the tyre rubber and can measure the strain in the tyre stably and reliably without any influence and disturbance to sensing area. The fabrication process of the strain sensor will have a reasonable cost and is possible to be introduced to the industry for mass production. Meanwhile, the strain sensor is capable of being integrated with a wireless transmitting system and an installation method (adhesive bonding method) will be also investigated.

1.3 Structure of the thesis

This chapter is introducing the background of the 'intelligent tyre' and the motivation of developing a tyre strain sensor. The objectives and structure of the thesis is also given in this chapter.

In chapter two, a literature review will be given. The strain behaviour will be investigated first. The study of the strain sensing technologies will then be presented and previous strain sensing system particularly in the tyres that developed by other researchers will be introduced as well. The five main strain sensing techniques that might be employed in the tyres will be compared and finally the capacitive strain sensing is determined as the research target. Based on the modelling of the tyre in the finite element analysis software and the previous study, the requirements of the strain sensor for the tyres will be listed. The last but not the least, an

investigation on a soft and compliant embedding material that is employed for the sensor design will be given at the end of the literature review.

In chapter three, the development of the capacitive strain sensor for the tyres will be presented. There will be three main designs introduced which are sharing the same design idea and concept. The theory of each design will be discussed and the calculation and simulation with respect to each design will be given as well. The wire bond capacitor design will be finally selected as the final design.

In chapter four, the fabrication process of the wire bond capacitor design will be presented in detail. In the beginning, the general fabrication process will be given. The potential problems and the limitation of the original fabrication process will be analysed. Based on several trials tests, a more stable, reliable and industry achievable fabrication process will be given. The wire bond structure will be developed to achieve the best wire bonding condition. The bond wire strain sensor will be shown at the end of the chapter.

In chapter five, the experiments and calibration of the strain sensor will be presented. Firstly, the adhesive bonding method between the surfaces of the tyre rubber and the strain sensor will be investigated. An efficient, easy and low-cost adhesive bonding method that will not influence the strain behaviour of the tyre has been identified. Three calibration methods for the strain sensor will be given and it is believed that the cantilever test is the best calibration method, which can obtain stable and reliable measurements. The comparison on the results

from tests, calculation and simulation will be given and discussed at the end.

In chapter six, the conclusions will be drawn from the study. The findings and developments in each chapter will be listed and summarized. The future work based on the current study process will be highlighted as well.

The following appendixes will explain the general tyre format and list the MATLAB codes that will be introduced in Chapter 3.

Reference

1. Andrzejewski, R. and J. Awrejcewicz, *Nonlinear dynamics of a wheeled vehicle*. Vol. 10. 2006: Springer Science & Business Media.
2. *European Tyre & Rubber Industry Statistics EDITION 2011*. Available from: http://www.etrma.org/uploads/Modules/Documentsmanager/20120612-etrma-statistics-2011.pdf.
3. Arat, M.A., K.B. Singh, and S. Taheri, *An intelligent tyre based adaptive vehicle stability controller.* International Journal of Vehicle Design, 2014. **65**(2-3): p. 118-143.
4. Ray, L.R., *Nonlinear tire force estimation and road friction identification: simulation and experiments.* Automatica, 1997. **33**(10): p. 1819-1833.
5. ENSIEG-INPG, B. and F. ST Martin d'lieres, *Dynamic tire friction models for vehicle traction control.* 1999.
6. Burke, A., *Finite Element Simulation and Experimental Analysis of Stationary and Rotating Tire Behavior*. 1998, PhD Thesis, Department of Mechanical Engineering, University of Birmingham.
7. Ghoreishy, M.H.R., *Finite element analysis of the steel-belted radial tyre with tread pattern under contact load.* Iranian Polymer Journal, 2006. **15**(8): p. 667-674.
8. Yang, X., *Finite element analysis and experimental investigation of tyre characteristics for developing strain-based intelligent tyre system*. 2011, University of Birmingham.
9. Sokolov, S., *Calculation of the stress-strain state of pneumatic tires by the finite*

element method. Journal of Machinery Manufacture and Reliability, 2007. **36**(1): p. 45-49.

10. Bolarinwa, E. and O. Olatunbosun, *Finite element simulation of the tyre burst test.* Proceedings of the Institution of Mechanical Engineers, Part D: Journal of Automobile Engineering, 2004. **218**(11): p. 1251-1258.

Chapter Two.
Literature Review

2.1 Introduction

This chapter firstly presents an overview of tyre strain sensing technology. First of all, the theory of the tyre strain behaviour and the related simulation methods on the tyre is briefly discussed. Then based on the information, the sensor size, sensing speed and measuring range is estimated. Following this, the review of existing strain sensor system is presented, the advantages and disadvantages of each sensing technology is discussed and analyzed. Furthermore, a study on these strain sensor systems that are employed in tyres in previous research is reviewed and the potential problem with respect to each tyre strain sensor system is studied as well. A list of requirements of the tyre strain sensor is then given and a comparison of a variety of possible strain sensing technology is also illustrated. Finally, the capacitive strain sensor is determined as the researching target. To overcome the stiffness problem that might be occurred by the metal structure in capacitive strain sensor, a complaint silicone rubber, polydimethylsiloxane (PDMS), is selected as an embedding material. Hence, an investigation of PDMS is studied as well with respect to its property and bonding methods.

2.2 Strains in tyres

This section will introduce the reason for measuring strain in tyre, tyre straining behaviour and related research methods, such as finite element analysis (FEA) that are employed in studying the behaviour of a tyre. Based on the information, the size of sensing area, the measuring speed and range will be discussed as well.

2.2.1 The reason for measuring strain in tyres

In recent years, the safety and manoeuvrability of the wheeled vehicles have become more and more concerned in the automotive community. The physical parameters in tyres, such as tyre pressure [1, 2] and friction between the tyre and the road [3-6], have been measured, studied and simulated by many researchers. As one of the most important properties in the tyre, the friction between tyre and road indicates the situation of the vehicle when braking, cornering and accelerating and is the key parameter for improving the safety, developing the driving experience, increasing the tyre lifetime and controlling fuel consumption. However, the friction is very difficult to be measured directly, so strain of the tyre has become the alternative property that the researchers focusing on [7-9]. It also has been proved that the straining behaviour in tread area of a tyre can provide accurate and significant information that will be used for analyzing the force in the contact patch between tyre and road [8, 10, 11]. Hence, strain in tyres plays an important role in the issue of safety and manoeuvrability for vehicles and measuring the strain will generate data/signals for analyzing the force between tyre and road in the 'intelligent tyre' [12], and the data/signals will eventually be converted to useful information to guide and correct the behaviour of drivers, which can increase the driving comfort level, extend the tyre lifetime and even prevent vehicles from extreme accidents.

2.2.2 Tyre strain behaviour

As mentioned in last section, when a vehicle is applied a load, the tread part of a tyre on the vehicle will generate a flat surface that contacts the road, which is called the contact patch. As

the strain in tread area is the most important for analyzing the force between the tyre and road [10], the strain in tread area is determined as the sensing area.

For a tyre in an ideal straining situation when rotating in a constant speed, there will be different deforming conditions along the contact patch, as shown in *figure 2.1* [10]. The contact patch is from point B to D, while the deforming area is slightly larger than the contact patch, which is from point F to G. In the circumferential direction the tread is gradually compressed and released at the areas which are before entering (from point F to B) or after leaving the contact patch (from point D to G). At point A and E the compressive strain is maximized. While along the contact patch, the tyre is stretched and at the point C, which is the centre point of the contact patch, the tensile strain is maximized. Moreover, due to the Poisson effect, the strain in axial direction is in a converse trend with respect to the strain in circumferential direction. Hence, the strain in a tyre is in dual directions, both circumferential direction (it is also called longitudinal direction) and axial direction. Therefore, the measuring method has to decouple the strains in one direction or the sensing system is only sensitive to one direction.

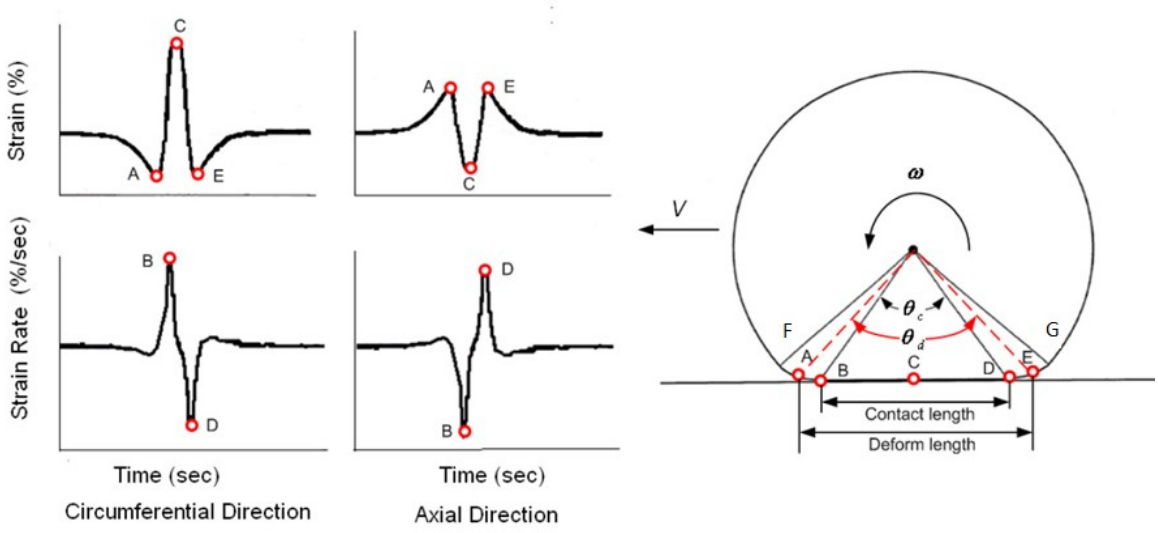

Figure 2.1 Tyre staining behaviour [10]

As shown in *figure 2.2 (a)*, when a tyre is in a traction condition, the tread that is entering the contact patch (from point F to B) is compressed more while the tread that leaving the contact patch (from point D to G) is stretched instead of compressed. The contact patch is still in a stretched condition but the maximum stretched stress/strain point moves to the right side of centre point C. The force that generated between the road and tyre therefore is in a same direction of the movement of the tyre. On the contrary, when a tyre in a braking condition, which is shown in *figure 2.2 (b)*, the tread that entering the contact patch (from point F to B) is stretched while the tread that leaving the contact patch (from pint D to G) is compressed more. And the maximum stretched stress/strain point moves to the left side of centre point C. Hence, the force between the road and tyre is in an opposite direction of the movement of the tyre.

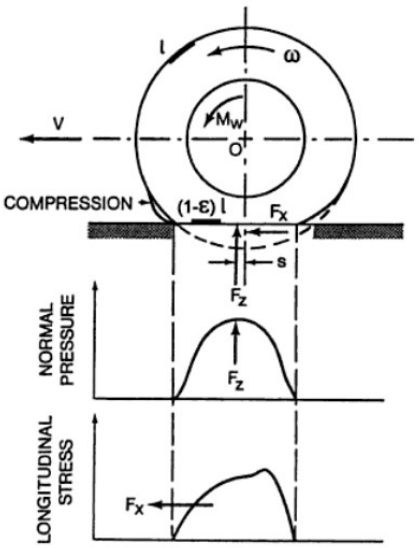

(a)

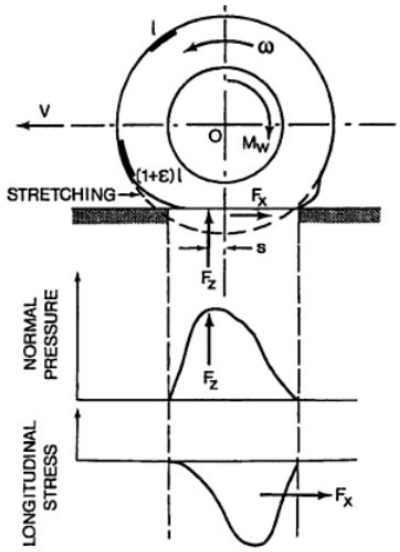

(b)

Figure 2.2 The stress in longitudinal direction when a tyre in a traction condition (a) and in a braking condition (b) [13]

To investigate the mechanical behaviour of the tyres, finite element analysis has been employed by many researchers [14-18]. Mir Harmid Reza Ghoreishy [15] noted that the angle θ_c that is generated by the contact patch and the centre point of the wheel is about 40° in

standard inflation pressure[1]. In his research the angle is also called belt angle, which is $\pm 20°$.

So, for a 175/70 R14 steel-belted radial tyre that simulated in the Ghoreishy's paper, the length of contact patch is approximately 205 mm[2]. The meshed contact patch that simulated by Ghoreishy is shown in *figure 2.3*. Since the sensing area along the contact patch locates in the middle line of the tyre, it can be seen that the number of the elements along the middle line in the contacting area are approximately 18. The size of each element, therefore, can be calculated, which is approximately 11.4 mm by 12.5 mm. So, it could be considered that the sensing area for the strain measurement has to be controlled in this area. An over-sized sensor could hardly measure the strain accurately.

For a vehicle in a normal speed, e.g. 75 km/h, it takes approximately 9.84 ms to go through the contact patch in each revolution. Hence, according to the total number of the elements along the contact patch, the duration of each measurement has to be controlled in 0.55 ms. In other words, the frequency of the measurement has to be higher than approximately 1850 Hz, and for a higher speed (125 km/h), this value will be higher (3050 Hz) as well. Therefore, assuming the maximum speed of the vehicle is 150 km/h (in most situations the speed cannot exceed this value), the measuring speed has to be higher than approximately 3700 Hz.

[1] The standard inflation pressure for a car tyres varies from the year, car manufacturer and models. It usually can be consulted from the car/tyre manufacturer.

[2] See Appendix I

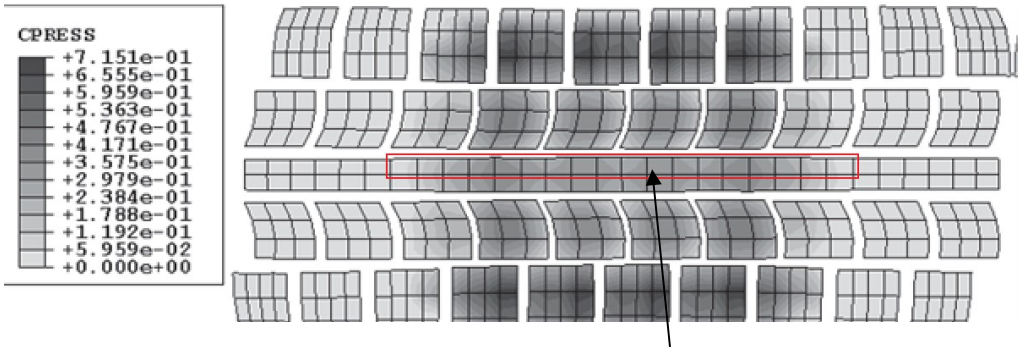

Figure 2.3 The meshed area near and including contact patch and distribution of the contact pressure for belt angle = ±20° [15]

From the simulation in the research of R.Matsuzaki et al [19], the strain range in the tyre can also be determined. As shown in *figure 2.4*, in the static condition, the strain along the contact patch is approximately 15000 micro-strain, it also can be seen that the compressed strain is approximately 6000 micro-strain. Hence, for the safety of the measurement, it can be concluded that the measuring range is approximately in -10000 to 20000 micro-strain.

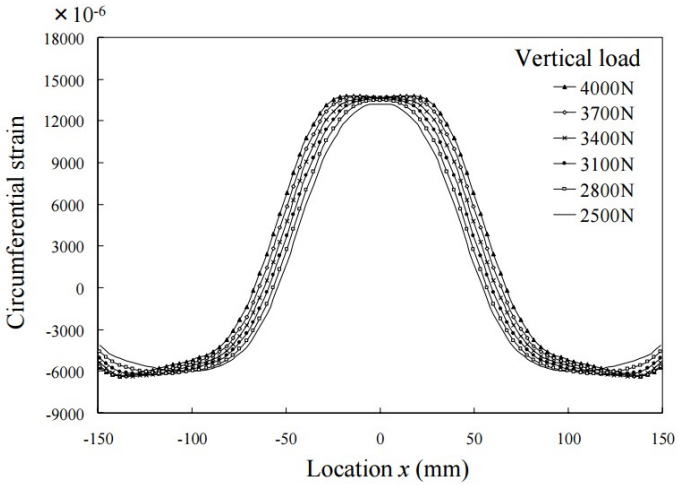

Figure 2.4 The circumferential strain distribution when a tyre in a static condition from the study of R.Matsuzaki et al[19]

2.3 Review of strain sensing technologies

This section introduces, summarises and compares a variety of strain sensing technologies.

Meanwhile, the relevant strain sensing systems that have been employed by past researchers are presented. Based on the information on the known sensing technology in this section and tyre straining behaviour investigated in last section, a list of requirements of the strain sensor in the tyre and the focused measuring method is given at the end of this section.

2.3.1 Basic foil strain sensor

The Foil strain sensor, which is also called foil strain gauge, has a long history since it was invented in 1938 by Edward E. Simmons and Arthur C. Ruge [20]. The sensor consists of an insulating flexible foil substrate and a metallic pattern and it is attached to the measuring area by an appropriate adhesive, such as cyanoacrylate. Hence, the metallic pattern will be deformed when the measuring area deformed, which results of the changes of electrical resistance in the sensor. By detecting the changes in the resistance by using a Wheatstone bridge [21, 22], the related strain will be known. A typical foil strain sensor *figure 2.5 (a)* and a Wheatstone bridge *figure 2.5 (b)* are shown below.

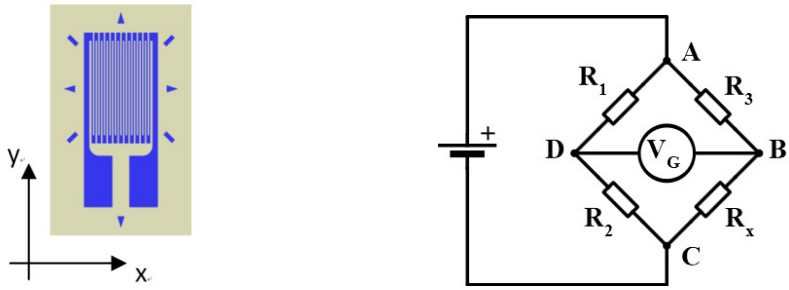

(a) *(b)*

Figure 2.5 A typical foil strain sensor (a) and a Wheatstone bridge (b) [23, 24]

As shown in *figure 2.5 (a)*, although the foil strain sensor could be deform in both directions, the thickness of the metallic pattern can be hardly changed by the deformation in x-axis. Hence, the sensor is only sensitive to the deformation in y-axis. For this characteristic,

combining two or three sensors as a strain rosette is usually employed, this is also presented in many past papers [25-27].

The advantages of the foil strain sensor are cheap and easy for installation. However, the stiffness of the sensor is a problem when measuring strain in soft materials [28]. In addition, the metallic pattern in the sensor is usually made of copper, which means the temperature will also have an effect on the resistance of the sensor. However, the temperature of the air in tyres can rise up to 40℃ in correct inflation condition [29], which means the temperature in the sensing environment approximately varies from 0 to 40℃. So, for this sensor it will be more complicated when measuring strains in tyres.

2.3.2 Fibre Bragg gratings optical strain sensor

Fibre optical sensors, which have been studied for almost forty years, are widely employed in measuring physical quantities, such as strain, temperature, humidity, and pressure [30-34]. In various fibre optical sensor technologies, fibre Bragg gratings (FBG) optical sensors are considered as the sensing mechanism and there has been much research in their design application [35]. Normally fibre Bragg gratings were manufactured in germanium-doped silica fibres or special polymer fibres [36-38]. As the photosensitive characteristics of the germanium-doped silica or the polymers, the Bragg gratings are 'written' by exposure to UV light. In an FBG optical sensor, micro-structured Bragg gratings are installed in the core of crystal fibres, which is shown below in *figure 2.6*. These gratings are arranged with a specific nano-scaled spacing that can create variations in refractive index. When the input light

containing a variety of wavelengths is irradiated from one end of the sensor, the light with a specific wavelength, which is called Bragg wavelength in some papers [39, 40], will be reflected while rest of the light can get transmitted to the other end. The wavelength of the reflected light λ_B has a relationship with the spacing in the Bragg gratings, which is given by [41]:

$$\lambda_B = 2 \cdot n_{eff} \cdot \Lambda \qquad Eq.\,2.1$$

Where n_{eff} is the refraction index of the material in the Bragg gratings, and Λ is the spacing in the Bragg gratings

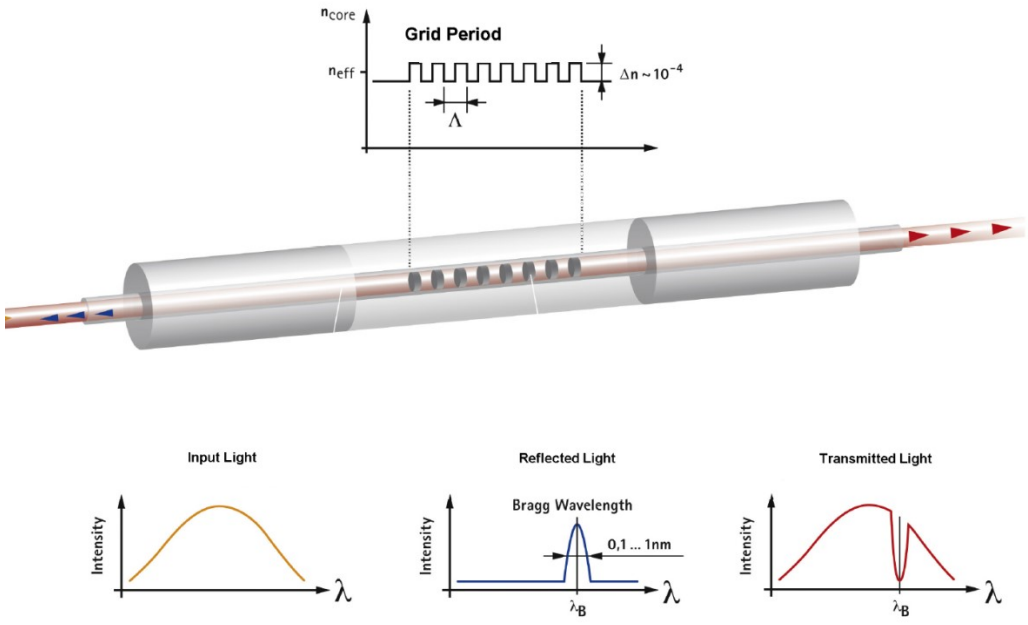

Figure 2.6 Theory of micro-structured optical Bragg gratings [41]

Hence, if the sensor is in a strained condition, the gratings in the sensor is be compressed or expanded, then the Bragg wavelength will be increased or decreased respectively. Meanwhile, the Bragg gratings are also sensitive to the thermal signal, such as temperature. Therefore, according to [41], the variation of the wavelength of the reflected light $\Delta\lambda_B$ is given by:

$$\Delta\lambda_B = 2\left(\Lambda\frac{\partial n_{eff}}{\partial l} + n_{eff}\frac{\partial\Lambda}{\partial l}\right)\Delta l + 2\left(\Lambda\frac{\partial n_{eff}}{\partial T} + n_{eff}\frac{\partial\Lambda}{\partial T}\right)\Delta T \qquad Eq\ 2.2$$

As it given by the equation (*Eq 2.2*), the spacing in the Bragg gratings is influenced by two main factors, which are mechanical and thermal signals. In order to discriminate between the effects of these two signals, a ultralow thermal sensitivity material, which is called polarization-maintaining photonic crystal fibre (PM-PCF), is employed in a temperature insensitive strain sensor [42].

However, there are also some limitations in this technology. The Bragg grating based sensor is only sensitive to the direction that is perpendicular to the gratings, the measuring range of most of the Bragg grating based sensor is only around $\pm$1% ($\pm$ 10,000 micro-strain) [41]. And this is also be mentioned in the information data sheet for a commercial fibre Bragg gratings sensor from Smart Fibre [43]. Additionally, since the sensor is based on a variety of lasers in different wave lengths to detect small variations in the gratings, there are at least one laser generating device and one laser capturing device in the measuring system, which will bring some difficulties when installing on MEMS platforms and also more costs. The material of FBG optical sensors is also a potential problem due to the high stiffness.

2.3.3 Surface acoustic wave (SAW) sensor

SAW sensor, which is known as surface acoustic wave sensor, always consists of a piezoelectric substrate with interdigital electrodes and some reflectors on the surface. The piezoelectric substrate, which is normally made of quartz or lithium tantalate, and to a lesser degree, lithium niobate [44], will generate an electric field when applied an appropriate

mechanical stress. When a radio frequency (RF) voltage is applied to the interdigital transducers (IDT) on the sensor at a specific frequency f_c, the IDT will generate an oscillating electric field which creates a mechanical wave that propagates on the surface of the substrate. The wave will be reflected by the reflectors, which are an additional set of electrodes, and the response is maximized if it can satisfy [45, 46]:

$$f_c = \frac{v_s}{2p} \qquad Eq.\,2.3$$

Where v_s is velocity of the surface wave and p is the spacing of each two reflectors

When a strain is applied to the substrate, the spacing of each two reflectors will be expanded or compressed. Meanwhile, the density of the substrate is also changed due to the strain energy, which results of changing the velocity of the surface wave [47]. The velocity can be given by:

$$v_s = \sqrt{\frac{c}{\rho}} \qquad Eq.\,2.4$$

Where c is the stiffness constant of the substrate and ρ is the density of the material of the substrate.

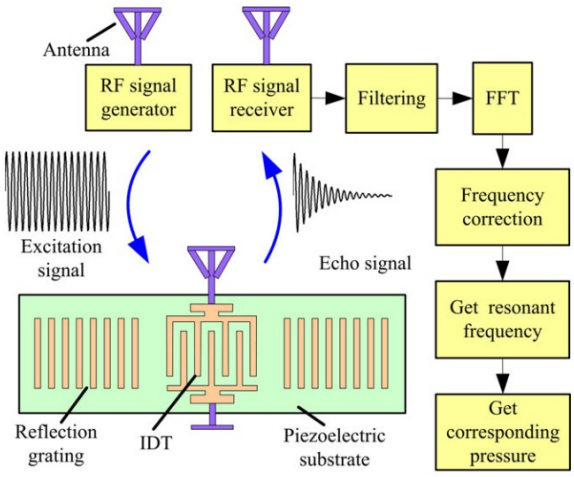

Figure 2.7 A schematic principle of measurement of a SAW sensor [45]

Hence, if the IDT can generate a series of waves in different frequency, the resonant

frequency f_c in a specific straining condition will be captured by the IDT and detected finally by the external device. Based on the changes of the resonant frequency, the strain can be calculated. *Figure 2.7* briefly shows a principle of measurement of a SAW sensor.

Meanwhile, there is an alternative measuring method in SAW sensor technology. Two reflectors are located in different distance from the IDT. When two same pulse signals are transmitted from the IDT, the delayed response from the reflectors will be different due to the different propagating distance for each reflector. As shown in *figure 2.8*, the difference of the phases $\Delta\phi$ can be given by [48]:

$$\Delta\phi = \left[\omega_0 - \frac{\mu(t_1 + t_2)}{2}\right]\Delta\tau \qquad Eq.\,2.5$$

And

$$\Delta\tau = t_2 - t_1 \qquad Eq.\,2.6$$

Where ω_0 is the frequency of the FM signal, μ is the rate of the modulation and t_1 and t_2 are the delayed time for first and second reflector, respectively.

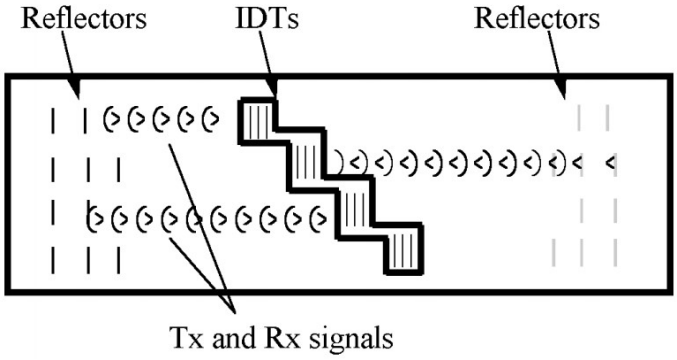

Figure 2.8 A schematic diagram of a SAW sensor using differences of the phases [48]

Since

$$\omega_0 \gg \frac{\mu(t_1 + t_2)}{2} \qquad Eq.\,2.7$$

The equation can be simplified as:

$$\Delta\phi = \omega_0 \Delta\tau \qquad Eq.\,2.8$$

When stress applied to the substrate, the distance between the reflectors will be changed, which results of the changes of the difference of the phases. If neglecting the effect of the variation of the velocity, the strain ε will be in a linear relationship with the difference of the phase, which is given by:

$$\Delta\phi = \omega_0(1+\varepsilon)\Delta\tau_0 \qquad Eq.\,2.9$$

Where $\Delta\tau_0$ is the difference of the time delay when strain is zero.

So by detecting the changes of the difference of the delayed time, the strain can be calculated. The advantage of a SAW sensor is that the signal in this sensing technology is capable of being transmitted and read at a long distance with radio frequency identification (RFID) systems while the SAW sensor itself is passive and powerless [49, 50]. And similar with the fibre optical sensor, the SAW sensor is sensitive to the thermal signals [7, 44, 51-53]. This thermal sensitivity can be minimized by special crystal cuts of the piezoelectric substrate [44, 51]. However, most of the piezoelectric materials have high Young's modulus, which means although these material can generate significant signal when bent, they can hardly be compressed or expanded. Hence, it is difficult for a SAW sensor to measure the strain in a direction that is totally parallel to the substrate. Also, due to the high stiffness of the substrate, the sensor will disturb the straining behaviour of soft samples.

2.3.4 Piezoelectric strain sensor

As introduced in 2.3.3, piezoelectric materials will generate electrical charge under an applied mechanical stress, and it is easy to be deflected but difficult to be compressed or expanded. So, most of traditional piezoelectric sensors are employed for measuring pressures in different situations [54, 55].

In order to minimize the influence of the stiff material that often employed in the commercial piezoelectric sensor, Jun Zhou et al. [56] developed a strain sensor based on individual ZnO piezoelectric fine-wires. These wires were eventually fully embedded in polydimethylsiloxane (PDMS) to achieve flexibility of the sensor. It was proved that the characterization of the I-V behaviour of the piezoelectric material would change when a strain occurred to the sensor due to the change in Schottky barrier height (SBH). As shown in *figure 2.9,* the I-V curves moves downward with a compressive strain while moves upward with an extended strain. Meanwhile, it is also found that the strain had a linear relationship with the change of SBH. Similar with this, a flexible piezoelectric ZnO-Paper Nano-composite strain sensor was developed by Hemtej Gullapalli et al. [57]

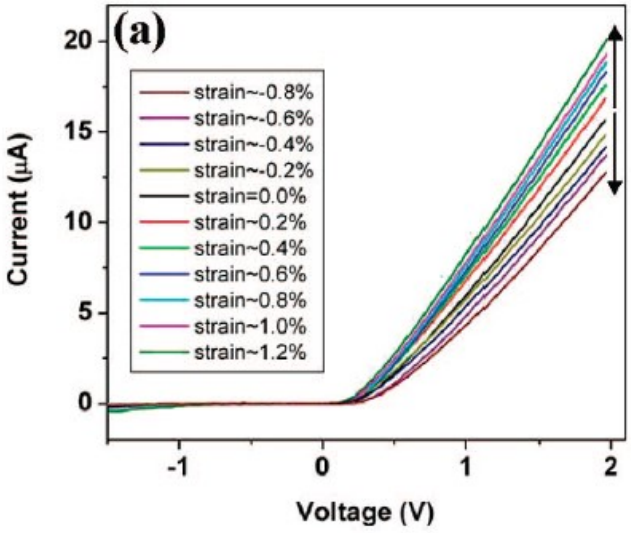

Figure 2.9 The I-V behaviour for piezoelectric material in different strains [56]

However, the applied strains in those two papers are known. Although the I-V curve varies based on different strain conditions, there is no an equation that can related the strain with the electrical signals, which means that it is difficult to measure the exact strain only from the I-V behaviour of the piezoelectric material. The strain is only estimated by fitting the measured I-V curve with the standard I-V curve that is generated by known strains. Therefore, it is necessary to acquire a huge data base to support an accurate measurement, which will inevitably result in a complicated calibration process for the sensor.

2.3.5 Capacitive strain sensor

Capacitive strain sensor is commonly employed in different sensing systems. Physical quantities, such as pressure, strain/stress, can change the distance between the electrodes in the capacitive structure, and result the variations in the capacitance. In microelectromechanical system (MEMS), capacitive strain sensors are usually based on the concept of an interdigital electrode structure. As shown in *figure 2.10,* this structure combines

two comb shape electrodes to generate a significant capacitance in a relatively small space. The original capacitance C_0 of this structure is given by [57]:

$$C_0 = (2n-1)\varepsilon_0\varepsilon\frac{ad}{g} + C_p \qquad Eq.2.10$$

Where the n is the number of fingers in one comb, d is the depth of the fingers, ε_0 is the electric constant, ε is the dielectric constant of the material around the structure and C_p is the parasitic capacitance. As shown in $Eq.2.10$, the capacitance at the end of every finger is neglected in some research.

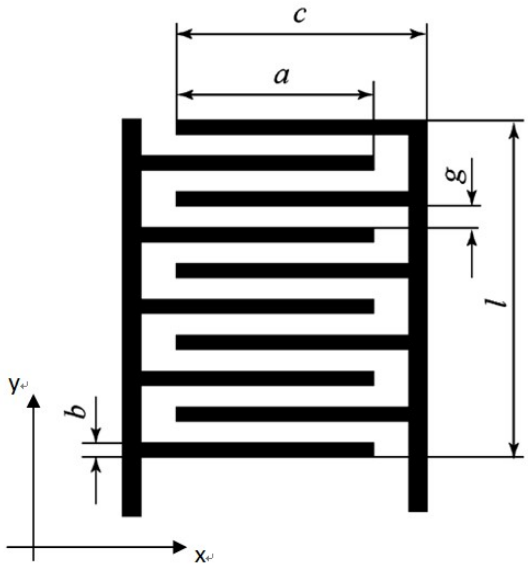

Figure 2.10 The configuration of interdigital electrodes [58]

According to equation $Eq.2.10$, the capacitive strain sensors are sensitive to the strain in both directions. It has been stated that the changes of the capacitance is linear to the strain in x-axis direction while is non-linear to the strain in y-axis direction [68]. The calculation is also carried out in MATLAB, which will be discussed in detail in Section 3.3.1. In some research papers [59, 60] the depth of the fingers is reduced to a sufficiently small value, which is called a co-planar capacitor, the equation will be not applicable since most of electrical field will be created upon or under the fingers rather than in the gaps between fingers. The

method of calculating the capacitance will be introduced and discussed in Section 3.3.2.

The cheap cost and varied measuring methods are the advantage of capacitive sensors. The wet etching process or photolithography process can achieve different features in this kind of capacitor in millimetre or micrometre scale sizes. Meanwhile, the electrical signal that is captured by the sensor can be transmitted wirelessly by many methods, such as the SAW technique [52], radio frequency identification (RFID) technique [61] and oscillating circuit [62, 63].

However, the fingers in the interdigital capacitive sensors are always made of metallic materials, which will inevitably result of the high stiffness of the sensor. Meanwhile, the capacitance of the sensor is not in a one-to- one correspondence relationship with the strain due to symmetry of the interdigital structure, which will be discussed in detail in Section 3.3.1.2.

2.3.6 Summary of strain sensing technologies

As introduced previously, *table 2.1* is illustrated to summarize and compare the advantages and disadvantages between foiled strain sensor, fibre optical strain sensor, surface acoustic wave sensor, piezoelectric strain sensor and capacitive sensor.

Table 2.1 The comparison of possible strain sensing technologies

No.	Type of sensor	Advantage	Disadvantage
1	Foil strain sensor	• Cheap cost • Easy for installation	• High stiffness • Sensitive to the temperature
2	Optical fibre strain sensor	• Accurate • Fast response to the variables	• High stiffness • More cost due to the laser generating and receiving systems as well as the installation • Sensitive to the thermal signals
3	Surface acoustic wave sensor	• Cheap cost • Easy for installation • Capable of transmitting signal remotely	• High stiffness
4	Piezoelectric strain sensor	• Could be flexible • Easy for installation	• Difficult to calibrate • The strain is not related to the measurements directly
5	Capacitive strain sensor	• Cheap cost • Easy for fabricating different features • Capable of multiple wireless transmitting methods	• High stiffness (could be reduced)

2.3.7 Past research on strain sensors in tyres

There have been several sensing techniques for measuring the strain in tyres developed in these years, which will be introduced from the aspects of sensing theory, transmitting method, cost and capability of mass production in this section. The advantages and disadvantages of each technique will be discussed and analyzed as well.

As mentioned previously, most of the piezoelectric materials have high stiffness, so some researchers employed a piezoelectric film which is made of polyvinylidene fluoride (PVDF) to minimize the rigid effect to the straining area. Jingang Yi employed a 20mm × 3mm × 110 μm PVDF sensor to estimate the wheel slip in mobile robotic platform [64]. G Erdogan, L Alexander and R Rajamani also developed a novel PVDF-based piezoelectric sensor which can measure the lateral deformation in tyres [65]. As shown in *figure 2.11*, one end of the piezoelectric beam is fixed on the rim, and thanks to the cylindrical component which is parallel to the lateral direction but perpendicular to the other end of the piezoelectric beam, the deformation in lateral direction will bend the beam while the deformation in the other two directions will be decoupled.

Additionally, the signal transmission is achieved by a voltage-to-frequency converter and a frequency-to-voltage converter, as shown in *figure 2.12*. The voltage signals in the PVDF due to the lateral deflections are first converted to a square wave in a modulated carrier frequency. Then it is transmitted by the antennas and converted back to voltage signals, which is eventually recorded by the data acquisition board.

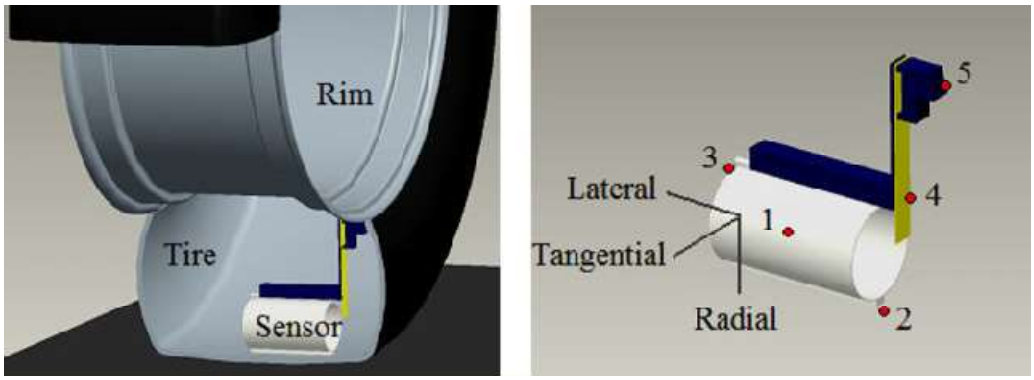

(a) *(b)*

Figure 2.11 The installation and the design of the sensor. (a) Sensor location. (b) the design of the sensor, (1) elastic cylindrical component, (2) sensor base, (3) slider mechanism, (4) elastic cantilever beam, (5) root of the cantilever beam [65]

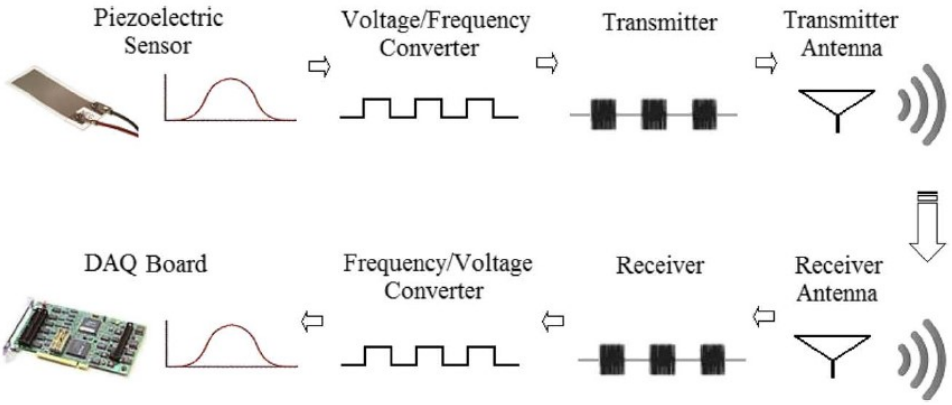

Figure 2.12 The wireless transmitting method for the piezoelectric strain sensor[65]

Although the design can successfully measure the deformation by using the piezoelectric sensor and decouple the deformation in other two directions perfectly, the deformation in the tangential and radial cannot be measured in this method. Additionally, the sensor itself is a PVDF-based piezoelectric sensor, which is in a low cost and capable of mass production. However, the complementary structure, which is the cylindrical component, brings a more complicated installation and an increasing cost.

Since in tyres there are many steel wire loops for strengthening and supporting the tyre structure, M.Sergio et al. [66] and R. Matsuzaki et al. [67] adopted the steel wires in the tyre itself as a part of sensing element, as show in *figure 2.13*. When the tyre is deflected, the distance between the sensing wires and the length of the sensing wires will be compressed or expanded, which will change in the capacitance and resistance. By measuring the variations, the strain in the sensing area is calculated. The calculation of capacitance between two arrays of wires with respect to the strain will be further discussed in Section 3.3.3.2. R. Matsuzaki et al. employed a simplified passive tuning circuit for transmitting the electrical signal out from the tyre wirelessly. As shown in *figure 2.14*, a series of reference signals (white noise) in radio frequency are emitted from the function generator, the tuned radio signal is captured by the external receiver. When the sensing part of the tyre is under an applied strain, the capacitance and resistance between the steel wires are changed, which results of a different resonant frequency and a peak power spectrum. The strain, then can be calculated by the measuring the changes of the resonated frequency and the peak power spectrum.

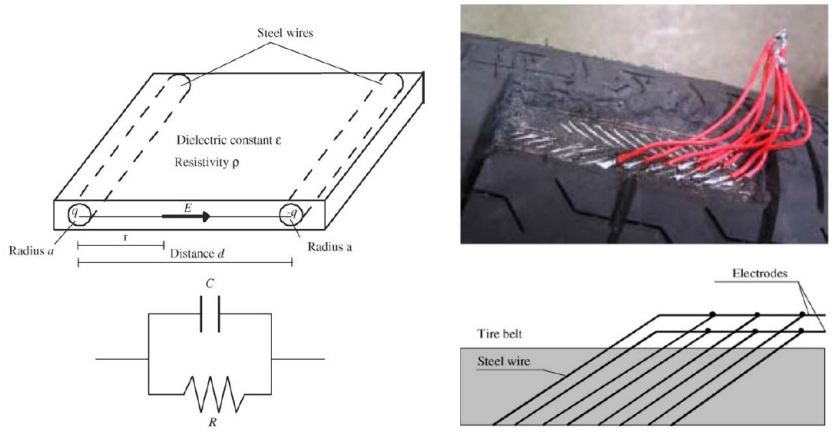

Figure 2.13 Steel wires in a tyre employed as a part of sensing element by R.Matsuzaki et al.[67]

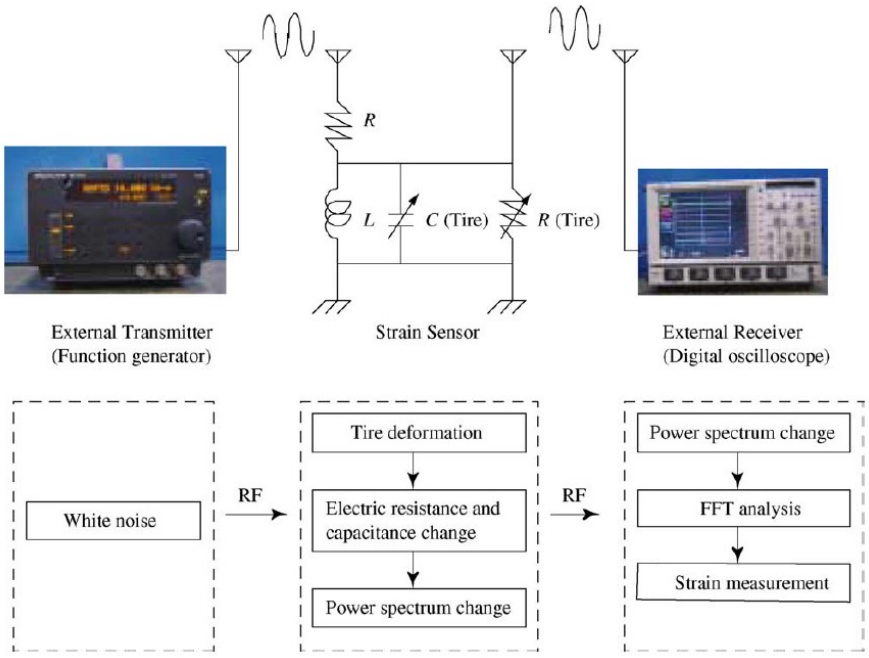

Figure 2.14 Wireless transmitting method employed in research by R. Matsuzaki et al[67]

This method is purely using the component of the tyre itself, which reduces the cost of sensor part dramatically. However, the steel wires are initially embedded in the tyre rubber, so there have to be some additional process to connect these sensing wires out, which probably results of damaging the tyre and is not capable of mass production.

A. J. Tuononen employed a position sensitive detector (PSD) to measure the deformation in a tyre carcass [68]. As shown in *figure 2.15*, a light emitting diode (LED) was installed on the inner tread of the tyre and a Piano-Convex (PCX) Lens is used to focus the light from the LED to the PSD. Based on the calculation of the position of the light spot on the tread when tyre deflected, the deformation of the tyre will be known.

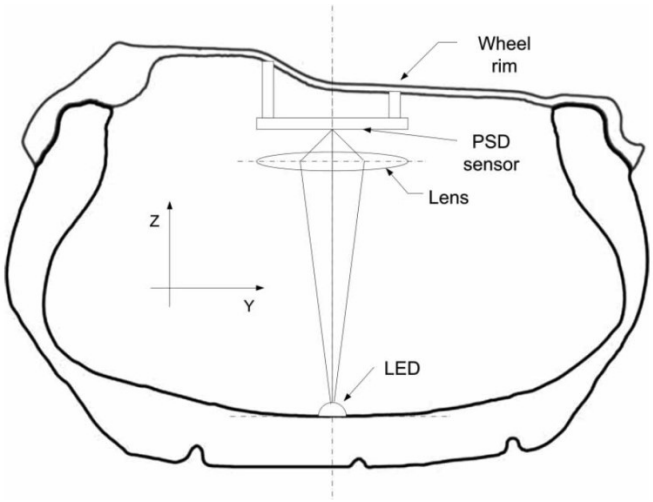

Figure 2.15 The assemblage of the optical sensor in tyre [68]

However, there are some potential problems in this system. As the signal that obtained in the PSD is transmitted wirelessly to the external receiver and the LED is installed inside of the tyre, there must be a battery to support them as a power supply, which brings more difficulties in the tyre maintenance. Otherwise, an energy harvesting system has to be employed if the system works in a sustainable condition, and whichever option results of a more complicated installation. Additionally, the position of the LED has to locate in a stable spot at the inside tread of the tyre, but after one hard braking, the LED probably deviates from the original position, which leads the inaccuracies of the measurements [68].

R. Matsuzaki et al. also developed an interdigital capacitive sensor to measure the strain in tyres [58, 69]. As mentioned, the metal fingers in the interdigitated structure results of high stiffness of the sensing device. Hence, to reduce the stiffness of the sensor itself, an ultra-flexible epoxy was employed. As shown in *figure 2.16*, two flexible printed circuit board (PCB) were etched down to specific patterns and the polyimide substrates were cut down along the edges of the interdigitated structure. After that, the two cut PCBs were combined

and bonded together by ultra-flexible epoxy.

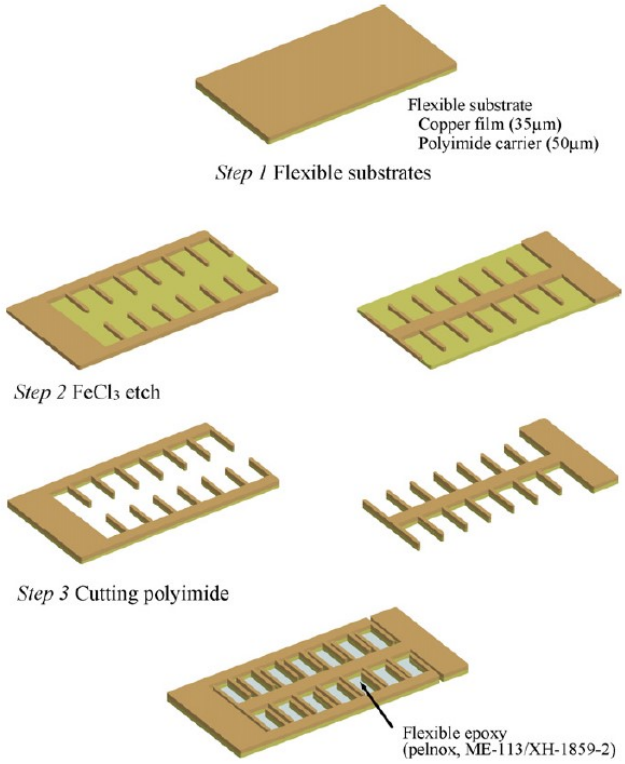

Figure 2.16 A schematic diagram of fabricating an interdigital strain sensor in an ultra-flexible epoxy [69]

Meanwhile, in terms of increasing gauge factor and initial capacitance of the device, as shown in *figure 2.17*, the fingers in one electrode were located at a close position to the fingers in the other electrode, which also increases the sensitivity to small strains. Additionally, amplitude modulation was employed in the transmitting system for this design, as shown in *figure 2.18*. The input signal V_{in} has the relationship with the output signal V_{out}:

$$V_{out} = \frac{C_x}{C_x + C_{ref}} V_{in} \qquad Eq. 2.11$$

Where C_x is the capacitance of the sensor and C_{ref} is the capacitance of the reference capacitor with constant value

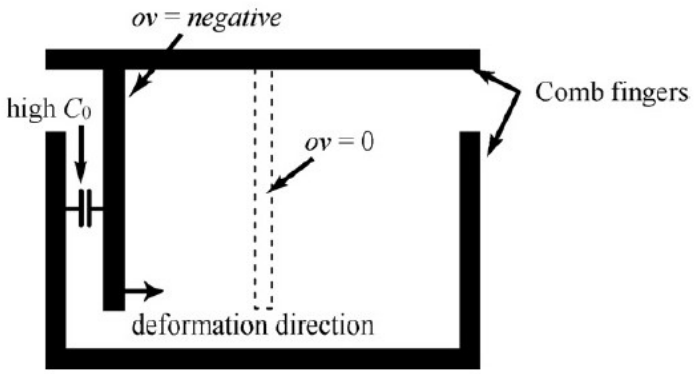

Figure 2.17. The schematic of the sensor configuration for obtaining higher original capacitance and increasing the sensitivity of the sensor [69]

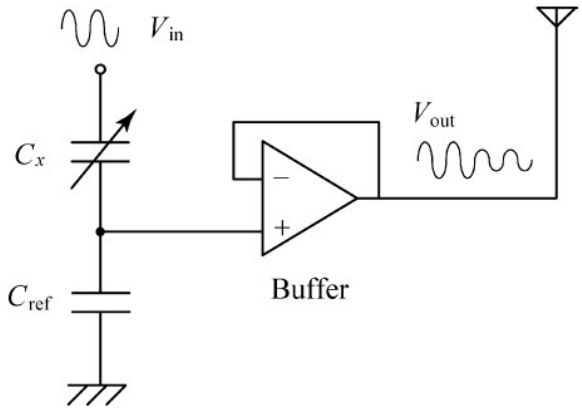

Figure 2.18 Amplitude modulation wireless transmitting method [69]

However, the sensor was also sensitive to the thermal signal, which might be caused by an increase of the dielectric constant of the ultra-flexible epoxy when temperature increases. According to the solution that R. Matsuzaki et al. have made [69], a dummy sensor has to be employed as self-temperature compensation, which results of more complicated installation and measuring process. And the detailed fabrication process was not stated clearly in the paper; it is uncertain whether the process could keep the interdigitated fingers located in the same position for each sensor in a mass production when introduced to the industry.

It has to be admitted that the findings in the tyre strain sensing techniques were limited and

there were no sensors/systems developed in recent five years and there was no commercial product existing in the market. Most of the researchers are still studying the strain in tyres in the FEA modelling area. Hence, a novel strain sensor that is specially employed in tyres is very desirable to design and develop.

2.4 The determination of strain sensing technology in tyres

2.4.1 The requirements of strain sensor in tyres

From the Section 2.3.7 and the tyre straining behaviour that was introduced in Section 2.2.2. The requirements for the tyre strain sensor can be listed in *table 2.2* below.

Table 2.2 Requirements for the tyre strain sensor

No	Requirements	
1	Size	Approximately 10 by 10 mm
2	Thermal stabilization/temperature compensation	Essential
3	Small stiffness	Desirable but for accurate measurement it is essential
4	Measuring directions in tyres	Only sensitive to one direction
5	Measuring speed	Maximum value can reach 3.7 kHz
6	Measuring range	-10000 to 20000 micro-strain
7	Easy installation	Desirable
8	Capable of wireless transmitting	Essential
9	Self powered/supported	Desirable
10	Capable of working in different	Desirable

	environments and climates	
11	Fabrication process	Possibly to be industrialized and mass produced

2.4.2 The determination of focusing on capacitive strain sensor

As shown in the table, most of the sensing techniques have the problem of high stiffness. Piezoelectric strain sensor can be flexible and easy for installation. However, the measurement cannot be directly related to the strain. Additionally, the sensing area will be another potential problem for piezoelectric strain sensor as well. On the contrary, capacitive strain sensor is more competitive, the strain variations can be related to changes of the capacitance directly, and the cheap costs of the material and fabrication process guarantee the capability of mass production. Meanwhile, the interdigitated structure can also meet the requirement of the small sensing area. Therefore, the capacitive strain sensor is then determined as the research focus. Due to the metal structure, high stiffness of the sensor is the only potential problem. Hence, an appropriate embedded material for the sensor is essential and will be introduced later.

2.5 An investigation on embedded material, Polydimethylsiloxane (PDMS)

To minimize the stiffness that might be brought by the metal structure of the sensor, a soft compliant embedding material is desirable. The material, moreover, has to be easy for operation and will not damage the sensor during the embedding process. Most of soft materials, for instance, natural rubber or synthetic rubber, always have to be coagulated,

heated or vulcanized when processing, which probably results of negative effects, such as melting and oxidising, on the sensor, especially on the precise structure. However, Polydimethylsiloxane, which is often called PDMS in short form, is a good alternative material for this case.

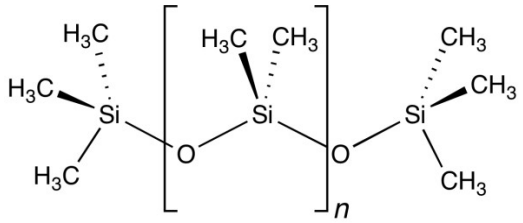

Figure 2.19 The chemical structure of polydimethylsiloxane (PDMS)

The chemical structure of PDMS is shown in *figure 2.19*. Compared with other polymer materials, PDMS has some special physical and chemical attributes: the flexibility (the young's modulus of PDMS could vary from 100kPa to 3MPa [70]), very low loss tangent, temperature stabilization for physical constants except the thermal expansivity [71], high compressibility, the capability in a wide temperature range [72], resistances to corrosiveness and a non-toxic nature. Additionally, PDMS is a viscous liquid that flows slowly and becomes solid when applied with a specific agent for 24 hours at room temperature. The solidification can be accelerated and the duration of the solidification can be reduced dramatically to approximately 20 min when the temperature is increased to 80℃. Due to these attributes, PDMS has become a common silicone rubber in many research applications. It was employed as a flexible interconnection between two wafers for microstructure assembly [73], a mould in most of research on microfluidics based chemistry and biology [74-77], an adhesive between PDMS and other polymer materials in some microfluidics research areas [78-80] and an embedding material in micro/nano scaled structures [81, 82]. Hence, as an embedding

material, PDMS can protect the capacitive sensor from the environment mechanically and chemically without influencing or damaging any structure of the sensor, but also minimize the stiffness of the sensor itself. *Table 2.3* illustrats below that showing the basic properties of PDMS.

Table 2.3 The properties of PDMS

Property	**Value**	**Reference**
Density	0.97 kg/m^3	[83]
Poisson ratio	0.5	
Dielectric constant	2.3-2.8 (normally treated as 2.75 when cross-linked, shown in *table 2.4*)	
Hydrophobicity	Highly hydrophobic (contact angle is 90 -120°)	
Young's modulus	360-870 kPa (shown in *figure 2.20*)	[76]

Table 2.4 The Dielectric constant of PDMS in different viscosity at 25℃ [83]

Viscosity at 25℃	**0.65**	**2.0**	**10**	**100**	**1000**	**12500**	**60000**
Dielectric constant, at 10^2-10^4 Hz	2.2	2.45	2.72	2.75	2.75	2.75	2.75

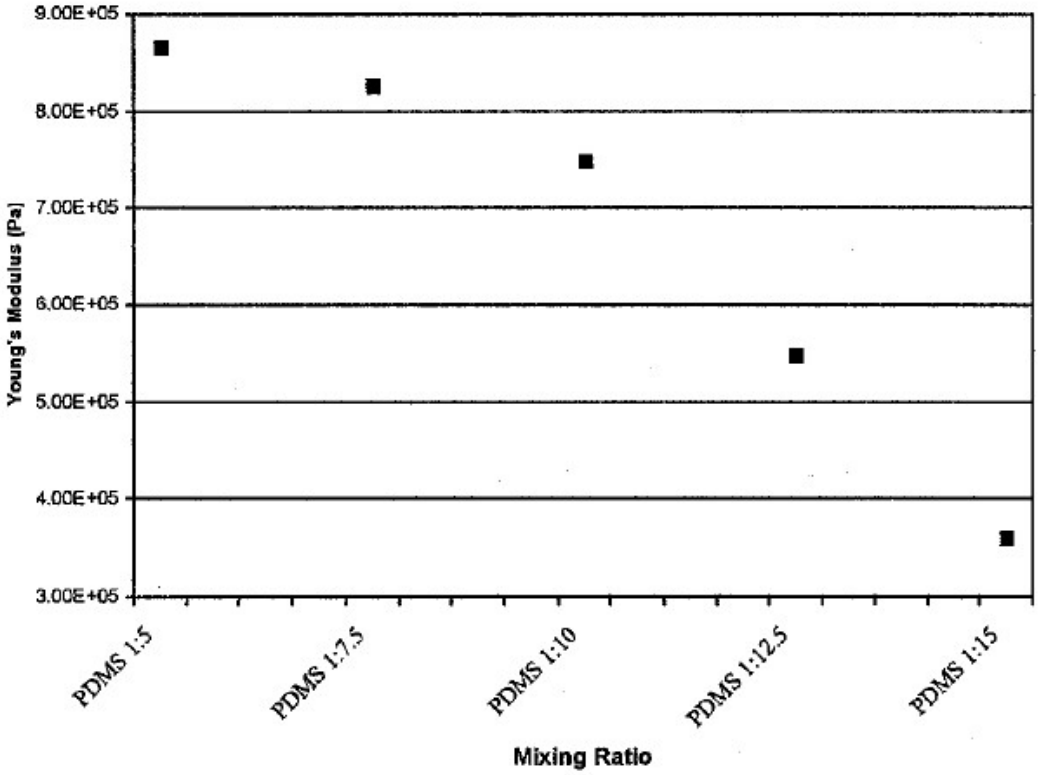

Figure 2.20 The Young's Modulus of PDMS in different mixing ratio [76]

However, the sensor will eventually measure the strain in tyres, which means that the sensor will have to be attached on the inner surface of the tyre. Therefore, the adhesive bonding method between the surfaces of the tyre rubber and PDMS is a challenge in this case. It is hard to find out any literature on this. The adhesive has to provide a firm connection between the sensor and tyre rubber without influencing the strain behaviour of either the tyre surface or the sensor. Hence, for instance, cyanoacrylate, which is known as superglue, is not an appropriate adhesive due to the high stiffness after polymerisation in spite of being employed in many bonding applications.

Oxygen plasma treatment is always employed for attaching the PDMS surface to other materials [78, 79, 84, 85]. Similar with this, corona discharge treatment is an alternative

method with less cost and simpler process [86]. Either oxygen plasma treatment or corona discharge treatment develops a silanol group (-OH) on both surfaces of the materials with a expense of methyl group ($-CH_3$) [87] and makes the PDMS surface highly hydrophilic [88], when contacting and pressing these two surfaces together, a Si-O-Si/Si-O-C bond will be yielded with loss of a water molecule. Hence, the bond forms an irreversible seal between these two surfaces. However, since the oxygen plasma treatment is often employed in fabrication of microfluidic structure, most of researching applications only focus on a reasonably low level of adhesion due to the small fluid pressure requirement [87]. Meanwhile, as one of the bonding surfaces is the inner surface of a tyre, the oxygen plasma treatment undoubtedly increases the cost of the installation of the sensor and also negates the mass production. Therefore, an efficiently convenient adhesive bonding method is desired in the sensing system.

2.6 Conclusions

This chapter firstly introduced the reasons for measuring the strain in tyres and the strain behaviour of the tyre. Due to the difficulties of measurement, there are many research papers alternatively aiming at the simulation on different mechanical properties of tyres. From the modules employed in the simulation, the size of sensing area and the sensing speed were determined. After that, the major five strain sensing technologies were studied, which are basic foiled strain sensor, fibre optic strain sensor, surface acoustic wave strain sensor, piezoelectric strain sensor and capacitive strain sensor. It can be concluded stiffness is one of most significant problems in these techniques, and a stiff sensor will have a remarkable effect

on the sensing area, which results of the unstable and unreliable measurement. Then, the previous research on the strain sensing technology specially in tyres was studied. Meanwhile, the advantages and the potential problems that might occur in each research paper were analyzed as well. Based on the study on the tyre behaviour and the previous research, requirements of strain sensor in tyres were listed in table 2.1. Moreover, a comparison between the studied strain sensing technologies was given and capacitive strain sensor was finally determined as the strain sensing technology that employed in tyres. To overcome the high stiffness that might be brought by the capacitive sensor, an investigation on a transparent and compliant embedding material, which is called Polydimethylsiloxane (PDMS), was presented. The mechanical and electrical properties of PDMS that related to sensor strain and capacitive sensing were studied. The adhesive bonding methods between PDMS and rubber tyre surfaces were investigated briefly and it can be concluded that, a more effective adhesive method instead of oxygen plasma treatment is desired for attaching the PDMS-packaged sensor to the rubber tyre surfaces.

Reference

1. Ishtiaq Roufa, R.M., et al. *Security and privacy vulnerabilities of in-car wireless networks: A tire pressure monitoring system case study*. in *19th USENIX Security Symposium, Washington DC*. 2010.

2. Pohl, A., et al. *Monitoring the tire pressure at cars using passive SAW sensors*. in *Ultrasonics Symposium, 1997. Proceedings., 1997 IEEE*. 1997. IEEE.

3. Velenis, E., et al., *Dynamic tyre friction models for combined longitudinal and lateral vehicle motion.* Vehicle System Dynamics, 2005. **43**(1): p. 3-29.

4. Canudas-De-Wit, C., et al., *Dynamic friction models for road/tire longitudinal interaction.* Vehicle System Dynamics, 2003. **39**(3): p. 189-226.

5. Holscher, H., et al., *Modeling of Pneumatic Tires by a Finite Element Model for the Development a Tire Friction Remote Sensor.* Center of Advanced European Studies and Research (CAESAR), Ludwig-Erhard-Allee, 2004. **2**: p. 53175.

6. Heinrich, G. and M. Klüppel, *Rubber friction, tread deformation and tire traction.* Wear, 2008. **265**(7–8): p. 1052-1060.

7. Pohl, A., R. Steindl, and L. Reindl, *The "intelligent tire" utilizing passive SAW sensors measurement of tire friction.* Instrumentation and Measurement, IEEE Transactions on, 1999. **48**(6): p. 1041-1046.

8. Matsuzaki, R. and A. Todoroki, *Wireless strain monitoring of tires using electrical capacitance changes with an oscillating circuit.* Sensors and Actuators A: Physical, 2005. **119**(2): p. 323-331.

9. Erdogan, G., L. Alexander, and R. Rajamani, *Estimation of tire-road friction coefficient using*

a novel wireless piezoelectric tire sensor. Sensors Journal, IEEE, 2011. **11**(2): p. 267-279.

10. Yang, X., *Finite element analysis and experimental investigation of tyre characteristics for developing strain-based intelligent tyre system*. 2011, University of Birmingham.

11. Morinaga, H., et al., *The possibility of intelligent tire (technology of contact area information sensing).* FISITA2006 Trans., F2006V104, 2006.

12. Holtschulze, J., H. Goertz, and T. Hüsemann, *A simplified tyre model for intelligent tyres.* Vehicle System Dynamics, 2005. **43**(sup1): p. 305-316.

13. Wong, J.Y., *Theory of ground vehicles*. 2001: John Wiley & Sons. p.19, p. 26.

14. Sokolov, S.L., *Calculation of the stress-strain state of pneumatic tires by the finite element method.* Journal of Machinery Manufacture and Reliability, 2007. **36**(1): p. 45-49.

15. Ghoreishy, M.H.R., *Finite element analysis of the steel-belted radial tyre with tread pattern under contact load.* Iranian Polymer Journal, 2006. **15**(8): p. 667-674.

16. Tönük, E. and Y.S. Ünlüsoy, *Prediction of automobile tire cornering force characteristics by finite element modeling and analysis.* Computers & Structures, 2001. **79**(13): p. 1219-1232.

17. Helnwein, P., et al., *A new 3-D finite element model for cord-reinforced rubber composites—application to analysis of automobile tires.* Finite elements in analysis and design, 1993. **14**(1): p. 1-16.

18. Charlton, D., J. Yang, and K. Teh, *A review of methods to characterize rubber elastic behavior for use in finite element analysis.* Rubber chemistry and technology, 1994. **67**(3): p. 481-503.

19. Matsuzaki, R., et al., *Analysis of Applied Load Estimation Using Strain for Intelligent Tires.* Journal of Solid Mechanics and Materials Engineering, 2010. **4**(10): p. 1496-1510.

20. Hoffmann, K., ed. *An Introduction to Measurements using Strain Gages*. 1989, Hottinger

Baldwin Messtechnik GmbH,Darmstadt.

21. Cowles, V.E., et al., *A quarter wheatstone bridge strain gage force transducer for recording gut motility.* The American journal of digestive diseases, 1978. **23**(10): p. 936-939.

22. Hylander, W.L., *In vivo bone strain in the mandible of Galago crassicaudatus.* American journal of physical anthropology, 1977. **46**(2): p. 309-326.

23. *Foil strain sensor http://en.wikipedia.org/wiki/Strain_gauge.*

24. *Wheatstone bridge http://en.wikipedia.org/wiki/Wheatstone_bridge.*

25. Hoskins, E.R., *An investigation of strain rosette relief methods of measuring rock stress.* International Journal of Rock Mechanics and Mining Sciences & Geomechanics Abstracts, 1967. **4**(2): p. 155-164.

26. Shah, J.S., W.G. Hampson, and M.I. Jayson, *The distribution of surface strain in the cadaveric lumbar spine.* J Bone Joint Surg Br, 1978. **60-B**(2): p. 246-51.

27. T.S. Gross, K.J. McLeod, and C.T. Rubin, *Characterizing bone strain distributions in vivo using three triple rosette strain gages.* Journal of Biomechanics, 1992. **25**(9): p. 1081-1087.

28. Cohen, D.J., et al., *A highly elastic, capacitive strain gauge based on percolating nanotube networks.* Nano letters, 2012. **12**(4): p. 1821-1825.

29. Hill, M. and J. Turner. *Automotive tyre pressure sensing*. in *Automotive Sensors, IEE Colloquium on*. 1992. IET.

30. Xu, M., et al., *Optical in-fibre grating high pressure sensor.* Electronics letters, 1993. **29**(4): p. 398-399.

31. Fu, H., et al., *Pressure sensor realized with polarization-maintaining photonic crystal fiber-based Sagnac interferometer.* Applied optics, 2008. **47**(15): p. 2835-2839.

32. Gatti, D., et al., *Fiber strain sensor based on a π-phase-shifted Bragg grating and the Pound-Drever-Hall technique.* Optics express, 2008. **16**(3): p. 1945-1950.

33. Choi, H.Y., et al., *Miniature fiber-optic high temperature sensor based on a hybrid structured Fabry–Perot interferometer.* Optics letters, 2008. **33**(21): p. 2455-2457.

34. Yeo, T., T. Sun, and K. Grattan, *Fibre-optic sensor technologies for humidity and moisture measurement.* Sensors and Actuators A: Physical, 2008. **144**(2): p. 280-295.

35. Lee, B., *Review of the present status of optical fiber sensors.* Optical Fiber Technology, 2003. **9**(2): p. 57-79.

36. Geernaert, T., et al., *Fiber Bragg gratings in germanium-doped highly birefringent microstructured optical fibers.* Photonics Technology Letters, IEEE, 2008. **20**(8): p. 554-556.

37. Jung, J., et al., *Simultaneous measurement of strain and temperature by use of a single-fiber Bragg grating and an erbium-doped fiber amplifier.* Applied optics, 1999. **38**(13): p. 2749-2751.

38. Chen, X., et al., *Bragg grating in a polymer optical fibre for strain, bend and temperature sensing.* Measurement Science and Technology, 2010. **21**(9): p. 094005.

39. Iadicicco, A., et al., *Thinned fiber Bragg gratings as high sensitivity refractive index sensor.* Photonics Technology Letters, IEEE, 2004. **16**(4): p. 1149-1151.

40. Xu, M., et al., *Temperature-independent strain sensor using a chirped Bragg grating in a tapered optical fibre.* Electronics Letters, 1995. **31**(10): p. 823-825.

41. Haase, K. *Strain sensors based on bragg gratings*. in *CD Proc. IMEKO Int'l Conf. Cultivating Metrological Knowledge, Merida, Mexico, November*. 2007.

42. Dong, X.Y., H.Y. Tam, and P. Shum, *Temperature-insensitive strain sensor with*

polarization-maintaining photonic crystal fiber based Sagnac interferometer. Applied Physics Letters, 2007. **90**(15).

43. Fibres, S., *FBG sensor datasheet*, S. Fibres, Editor.

44. Drafts, B., *Acoustic wave technology sensors.* Ieee Transactions on Microwave Theory and Techniques, 2001. **49**(4): p. 795-802.

45. Ye, X.S., et al., *Studies of a high-sensitive surface acoustic wave sensor for passive wireless blood pressure measurement.* Sensors and Actuators a-Physical, 2011. **169**(1): p. 74-82.

46. Pohl, A. and F. Seifert, *Wirelessly interrogable surface acoustic wave sensors for vehicular applications.* Ieee Transactions on Instrumentation and Measurement, 1997. **46**(4): p. 1031-1038.

47. Haekwan Oh1, K.L., Kyoungtae Eun2, Sung-Hoon Choa2 and Sang Sik Yang1, *Development of a high-sensitivity strain measurement system based on a SH SAW sensor.* JOURNAL OF MICROMECHANICS AND MICROENGINEERING, 2012. **22**(2).

48. Varadan, V.V., et al., *Wireless passive IDT strain microsensor.* Smart Materials & Structures, 1997. **6**(6): p. 745-751.

49. Shmaliy, Y.S., et al. *An analysis of errors in RFID SAW-tag systems with pulse position coding*. in *Proc. 6th WSEAS Int. Conf. Comput. Eng. Appl. Amer. Conf. Appl. Math*. 2012.

50. Chawla, V. and D.S. Ha, *An overview of passive RFID.* Communications Magazine, IEEE, 2007. **45**(9): p. 11-17.

51. Seifert, F., W.E. Bulst, and C. Ruppel, *Mechanical Sensors Based on Surface Acoustic-Waves.* Sensors and Actuators a-Physical, 1994. **44**(3): p. 231-239.

52. Schimetta, G., F. Dollinger, and R. Weigel, *A wireless pressure-measurement system using a*

SAW hybrid sensor. Ieee Transactions on Microwave Theory and Techniques, 2000. **48**(12): p. 2730-2735.

53. Li, T.L., et al., *Pressure and temperature microsensor based on surface acoustic wave.* Electronics Letters, 2009. **45**(6): p. 337-338.

54. Eaton, W.P. and J.H. Smith, *Micromachined pressure sensors: Review and recent developments.* Smart Electronics and Mems - Smart Structures and Materials 1997, 1997. **3046**: p. 30-41.

55. Wu, C.H., C.A. Zorman, and M. Mehregany, *Fabrication and testing of bulk micromachined silicon carbide piezoresistive pressure sensors for high temperature applications.* Ieee Sensors Journal, 2006. **6**(2): p. 316-324.

56. Zhou, J., et al., *Flexible piezotronic strain sensor.* Nano Letters, 2008. **8**(9): p. 3035-3040.

57. Gullapalli, H., et al., *Flexible Piezoelectric ZnO-Paper Nanocomposite Strain Sensor.* Small, 2010. **6**(15): p. 1641-1646.

58. Matsuzaki, R., et al., *Rubber-based strain sensor fabricated using photolithography for intelligent tires.* Sensors and Actuators a-Physical, 2008. **148**(1): p. 1-9.

59. Igreja, R. and C.J. Dias, *Analytical evaluation of the interdigital electrodes capacitance for a multi-layered structure.* Sensors and Actuators a-Physical, 2004. **112**(2-3): p. 291-301.

60. Vendik, O.G., S.P. Zubko, and M.A. Nikol'ski, *Modeling and calculation of the capacitance of a planar capacitor containing a ferroelectric thin film.* Technical Physics, 1999. **44**(4): p. 349-355.

61. Preradovic, S., N. Kamakar, and E.M. Amin. *Chipless RFID tag with integrated resistive and capacitive sensors*. in *Microwave Conference Proceedings (APMC), 2011 Asia-Pacific*. 2011.

IEEE.

62. Todoroki, A., S. Miyatani, and Y. Shimamura, *Wireless strain monitoring using electrical capacitance change of tire: part I - with oscillating circuit.* Smart Materials & Structures, 2003. **12**(3): p. 403-409.

63. Todoroki, A., S. Miyatani, and Y. Shimamura, *Wireless strain monitoring using electrical capacitance change of tire: part II - passive.* Smart Materials & Structures, 2003. **12**(3): p. 410-416.

64. Yi, J.G., *A piezo-sensor-based "smart tire" system for mobile robots and vehicles.* Ieee-Asme Transactions on Mechatronics, 2008. **13**(1): p. 95-103.

65. Erdogan, G., L. Alexander, and R. Rajamani, *A novel wireless piezoelectric tire sensor for the estimation of slip angle.* Measurement Science and Technology, 2010. **21**(1): p. 015201.

66. Sergio, M., et al., *On a road tire deformation measurement system using a capacitive-resistive sensor.* Smart Materials & Structures, 2006. **15**(6): p. 1700-1706.

67. Matsuzaki, R. and A. Todoroki, *Passive wireless strain monitoring of actual tire using capacitance-resistance change and multiple spectral features.* Sensors and Actuators a-Physical, 2006. **126**(2): p. 277-286.

68. Tuononen, A.J., *Optical position detection to measure tyre carcass deflections.* Vehicle System Dynamics, 2008. **46**(6): p. 471-481.

69. Matsuzaki, R. and A. Todoroki, *Wireless flexible capacitive sensor based on ultra-flexible epoxy resin for strain measurement of automobile tires.* Sensors and Actuators a-Physical, 2007. **140**(1): p. 32-42.

70. Clarson, S.J. and J.A. Semlyen, *Siloxane polymers*. 1993: Prentice Hall.

71. Lötters, J., et al., *The mechanical properties of the rubber elastic polymer polydimethylsiloxane for sensor applications.* Journal of Micromechanics and Microengineering, 1997. **7**(3): p. 145.

72. Van Krevelen, D.W. and K. Te Nijenhuis, *Properties of polymers: their correlation with chemical structure; their numerical estimation and prediction from additive group contributions*. 2009: Elsevier.

73. Arquint, P., et al. *Flexible polysiloxane interconnection between two substrates for microsystem assembly*. in *Solid-State Sensors and Actuators, 1995 and Eurosensors IX.. Transducers' 95. The 8th International Conference on*. 1995. IEEE.

74. Eteshola, E. and D. Leckband, *Development and characterization of an ELISA assay in PDMS microfluidic channels.* Sensors and Actuators B-Chemical, 2001. **72**(2): p. 129-133.

75. Park, T., et al., *Highly sensitive signal detection of duplex dye-labelled DNA oligonucleotides in a PDMS microfluidic chip: confocal surface-enhanced Raman spectroscopic study.* Lab on a Chip, 2005. **5**(4): p. 437-442.

76. Armani, D., C. Liu, and N. Aluru, *Re-configurable fluid circuits by PDMS elastomer micromachining.* Mems '99: Twelfth Ieee International Conference on Micro Electro Mechanical Systems, Technical Digest, 1999: p. 222-227.

77. Mosadegh, B., et al., *Simultaneous fabrication of PDMS through-holes for three-dimensional microfluidic applications.* Lab on a Chip, 2010. **10**(15): p. 1983-1986.

78. Eddings, M.A., M.A. Johnson, and B.K. Gale, *Determining the optimal PDMS–PDMS bonding technique for microfluidic devices.* Journal of Micromechanics and Microengineering, 2008. **18**(6): p. 067001.

79. Lee, K.S. and R.J. Ram, *Plastic–PDMS bonding for high pressure hydrolytically stable active microfluidics.* Lab on a Chip, 2009. **9**(11): p. 1618-1624.

80. Wu, H.K., B. Huang, and R.N. Zare, *Construction of microfluidic chips using polydimethylsiloxane for adhesive bonding.* Lab on a Chip, 2005. **5**(12): p. 1393-1398.

81. Liu, C.-X. and J.-W. Choi, *Patterning conductive PDMS nanocomposite in an elastomer using microcontact printing.* Journal of Micromechanics and Microengineering, 2009. **19**(8): p. 085019.

82. Park, H., K. Seo, and K.B. Crozier, *Adding colors to polydimethylsiloxane by embedding vertical silicon nanowires.* Applied Physics Letters, 2012. **101**(19): p. 193107.

83. Mark, J.E., *Polymer Data Handbook: Oxford University Press.* New York, 1999.

84. Tang, K.C., et al., *Evaluation of bonding between oxygen plasma treated polydimethyl siloxane and passivated silicon.* International Mems Conference 2006, 2006. **34**: p. 155-161.

85. Krump, H., et al., *Adhesion strength study between plasma treated polyester fibres and a rubber matrix.* Applied Surface Science, 2005. **240**(1-4): p. 268-274.

86. Haubert, K., T. Drier, and D. Beebe, *PDMS bonding by means of a portable, low-cost corona system.* Lab on a Chip, 2006. **6**(12): p. 1548-1549.

87. Bhattacharya, S., et al., *Studies on surface wettability of poly (dimethyl) siloxane (PDMS) and glass under oxygen-plasma treatment and correlation with bond strength.* Microelectromechanical Systems, Journal of, 2005. **14**(3): p. 590-597.

88. Hillborg, H. and U. Gedde, *Hydrophobicity changes in silicone rubbers.* IEEE Transactions on Dielectrics and Electrical insulation, 1999. **6**(5): p. 703-717.

Chapter Three.
The Development on the Design of Capacitive Strain Sensor for Tyres

3.1 Introduction

In the literature review, the capacitive sensor was determined as the study target for the strain sensor in tyres. Hence, in this chapter, the development on the capacitive strain sensor for tyres will be presented. The design ideas and concepts will be first introduced, which are interdigitated structure and PDMS embedding. As followed, there will be three designs introduced based on the concepts, which are interdigital capacitor design, coplanar capacitor design and bond wire capacitor design. In each design, calculations on the capacitance and the capacitance changes with respect to strain will be given. Since the interdigital design was following the existed research projects [1-3], it was decided to initially check the feasibility of the design and fabrication process before modelling. But due to the high stiffness of the design and the un-efficient adhesion method found for this device, no further modelling or measurements were undertaken. For the coplanar capacitor design and bond wire capacitor design, a finite element analyse software, which is named COMSOL Multiphysics, will be employed to simulate the capacitance and the capacitance changes respect to strains as well. Meanwhile, comparisons between the results from simulation and calculation will be presented. The stiffness of the sensor is the most significant problem for designing. A high stiffness sensor will cause inevitable disturbances on the strain behaviour of the sensing area and the strain of the tyre will not be coupled to the sensor. Among these three designs, the bond wire capacitor design can minimize the stiffness that brought by the capacitive structure

and in the same time achieve a reasonable capacitance and sensitivity, which is selected as final design for the tyre strain sensor.

3.2 Design ideas and concepts

In order to minimize the influence brought by sensor on the tyre strain, the stiffness of the sensor has to be smaller than or similar with that of the tyre (which is 5-10 MPa). In this work, the aim was produce the sensor with stiffness that is below 5MPa. Additionally, as introduced in literature review, the initial capacitance of the sensor in previous research was approximately from 10 to 30 pF [1, 2], so the capacitance of the sensor has to be a considerable value for measuring the variation of 1% of the strain or even less [3]. Therefore, the flexibility and the capacitance of the capacitor are the two main potential problems to be concerned during the sensor design and development. So, two ideas which aim at these problems will be introduced: interdigital structuring and PDMS embedding.

As the tyre strain is changing while rotating, the size of the sensor has to be small enough to measure the tyre strain at the sensing area in every straining position of the contact patch. Hence, based on the literature review and the work of previous researchers [1, 4], the size of the sensor was determined to be approximately 10 by 10 mm. In terms of the requirement of space and flexibility, an interdigital structure was employed. Interdigital structure is widely used in capacitive sensor in different research areas [1, 5, 6]. A typical interdigital structure, which has two comb-structures sticking into each other, is shown in *figure 3.1*. Employing this structure can fully utilize the square space to generate a reasonable capacitance,

meanwhile, the multiple fingers are splitting the whole electrode plates in the original parallel capacitive structure into many small ones, which can increase the flexibility of the capacitor dramatically and adapt the sensor to the stiffness of the tyre, thus minimizing the influence to the sensing area in the tyre

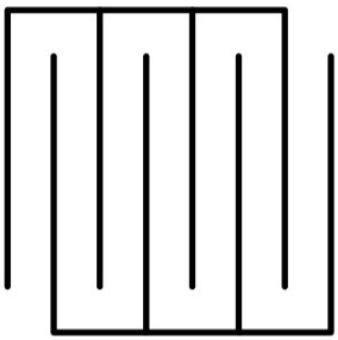

Figure 3.1 A schematic diagram of a typical interdigital structure

In the literature review, polydimethysiloxane (PDMS) is introduced and concerned to be employed as an embedding material for the whole sensor structure. The Young's modulus of PDMS in different mixing ratios are approximately from 3.6×10^5 to 8.7×10^5 Pa [7], which are very flexible compared with the tyre rubber. So, it is believed that the PDMS embedding can efficiently maintain the flexibility of the sensor and protect the structure from potential damage.

3.3 Sensor development

In this section, the development of the sensor design will be presented. There are three main designs, which are interdigital capacitor design, coplanar capacitor design and bond wire capacitor design. These three designs share the same concept but the details in each design differ from each other. Respect to each design, the process of simulation is also presented and

discussed as well. Nonetheless, from the test and simulation, it can be found that the first two designs (interdigital capacitor design and coplanar capacitor design) have some defects either in the flexibility or the total capacitance while the bond wire capacitor design is determined as the final design.

3.3.1 Interdigital capacitor design

3.3.1.1 The theory of interdigital capacitor design

Based on the previous study on the capacitive sensor and the idea of interdigitated structure that was introduced previously [8, 9], an interdigital capacitor was designed as shown in *figure 3.2*. According to the formula of capacitance:

$$C = \varepsilon_0 \varepsilon_r \frac{A}{d} \qquad Eq.\,3.1$$

Where C is the capacitance, A is the area of overlapping of the two plates, d is the distance between the plates, ε_r is the dielectric constant of the material between the plates, ε_0 is the electric constant, which approximately equals to $8.854 \times 10^{-12}\ F\ m^{-1}$.

Hence, the initial capacitance of the design is given by:

$$C_{i0} = \varepsilon_0 \varepsilon_{PDMS} \left[c d_f \left(\frac{2n-1}{a} \right) + w d_f \left(\frac{2n-2}{a} \right) \right] + C_p \qquad Eq.\,3.2$$

Where C_{i0} is the initial capacitance of the interdigtal capacitor, C_p is the parasitic capacitance, $\varepsilon_{PDMS} = 2.75$ is the dielectric constant of PDMS [10], $c = 10\,mm$ is the overlapping length of fingers, $d_f = 1.2\,mm$ is the thickness of fingers, $a = 0.3\,mm$ is the gap between two fingers and $w = 1\,mm$ is the width of the finger and $n = 5$ is the number of fingers in one comb structure.

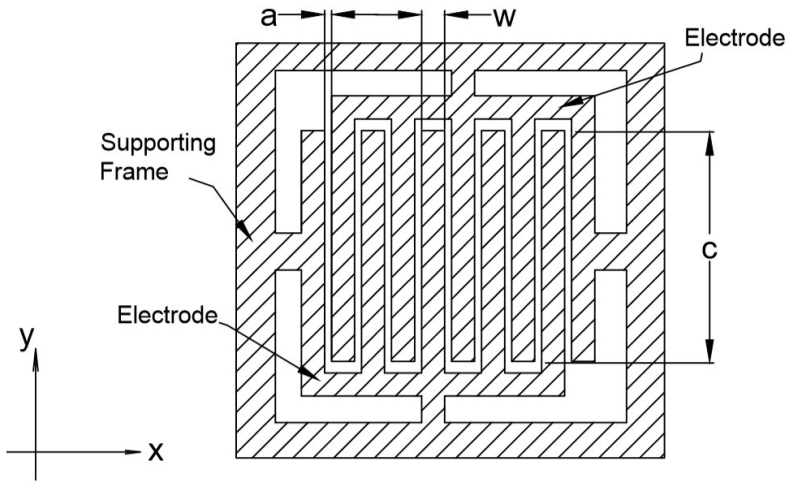

Figure 3.2 The 2-D image of interdigital capacitor design

Hence, when a small deflection $\begin{bmatrix}\Delta x\\ \Delta y\end{bmatrix}$ occurs, where Δx in x direction and Δy in y direction, the capacitance can be given by:

$$C_{i,deflected} = \varepsilon_0 \varepsilon_{PDMS}[(c-\Delta y)d_f\left(\frac{n}{a+\Delta x}+\frac{n-1}{a-\Delta x}\right)+wd_f\left(\frac{n-1}{a+\Delta y}+\frac{n-1}{a-\Delta y}\right) + C_p \qquad Eq.3.3$$

From $Eq.3.3$, it can be figured out that the capacitance is both in a non-linear relationship with the deflection in x and y direction, which means that the capacitance at the ends of the finger cannot be neglected and this is different from the literature review in Section 2.3.5.

3.3.1.2 Simulation, fabrication and experiments on the interdigital capacitor design

MATLAB is used to investigate the relationship between the capacitance change and strain in x and y direction[3], which is shown in *figure 3.3 (a)* and *(b)*, respectively.

As it can be seen in *figure 3.3 (a)*, in x-direction, the capacitance has small variations at small strains and is not in one-to-one correspondence relationship with the strain. Either when the

[3] The MATLAB code is given in Appendix II

sensor is under compression condition (the strain is in negative value) or under extension condition (the strain is in positive value), the capacitance will both be increased. So, there are two straining points that giving the same value of the capacitance, which is a potential problem when using the design for measuring strain in both compression and extension conditions. Meanwhile, the minimum capacitance, which is 9.545 pF, does not locate at the original point but at the point when the strain is approximately 1340 micro-strain.

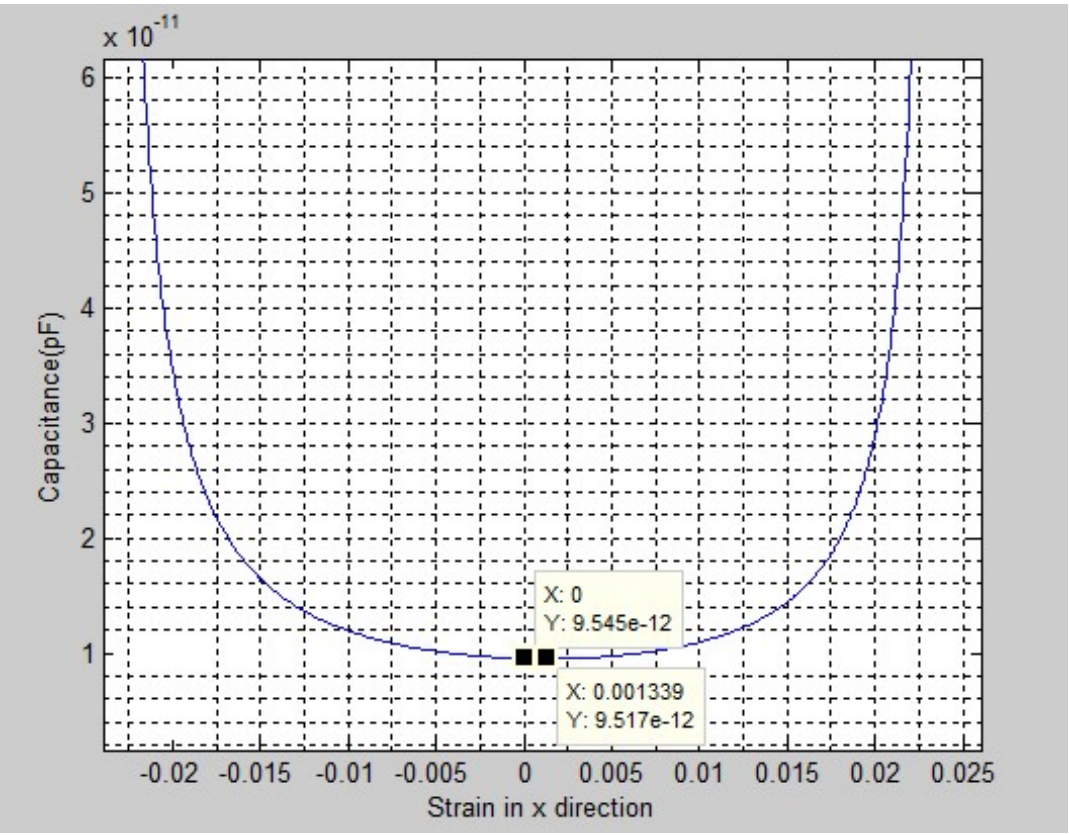

(a)

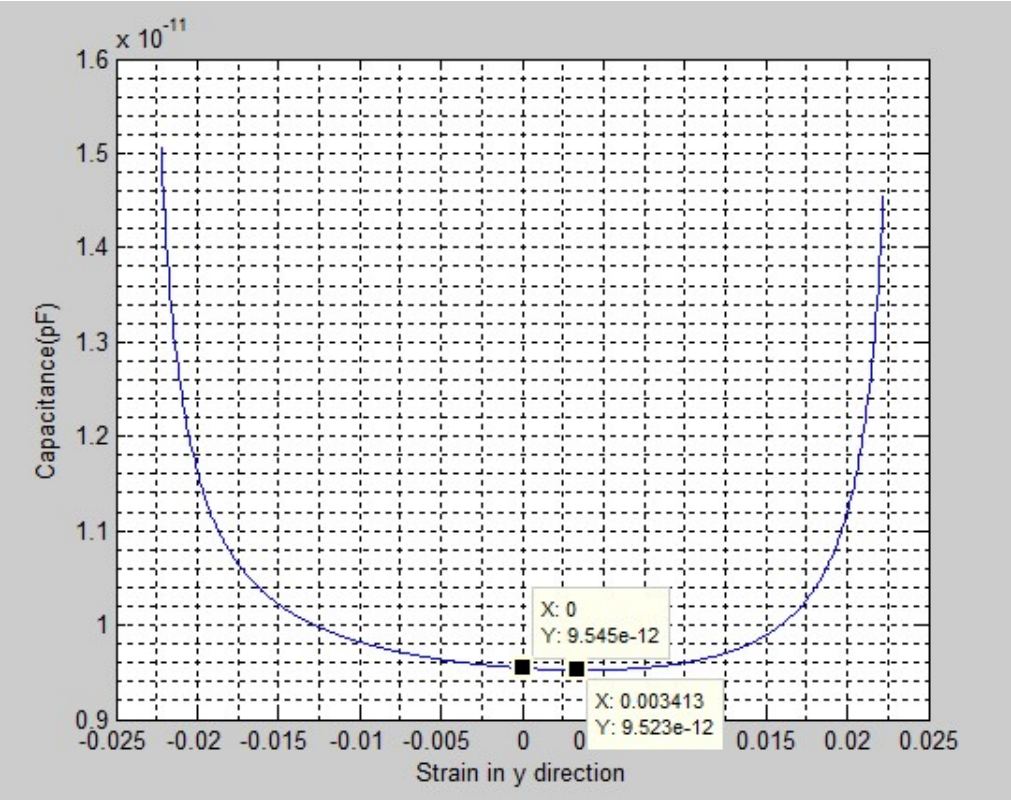

(b)

Figure 3.3 The calculated capacitance of the interdigital capacitor design with respect to strain in x (a) and y (b) direction, drawn in MATLAB

As shown in *figure 3.3 (b)*, similar with the strain in x direction, the strain is not in a one to one correspondence relationship with the capacitance in y direction. The trend of capacitance in compression condition (when the strain is in negative value) and extension condition (when the strain is in positive value) is also similar with that in x direction. The minimum capacitance, which is 9.523 pF, occurs when the strain is approximately 3400 micro-strain. However, it can be seen that the changing rate in y direction, which is the sensitivity, is less than that in x direction.

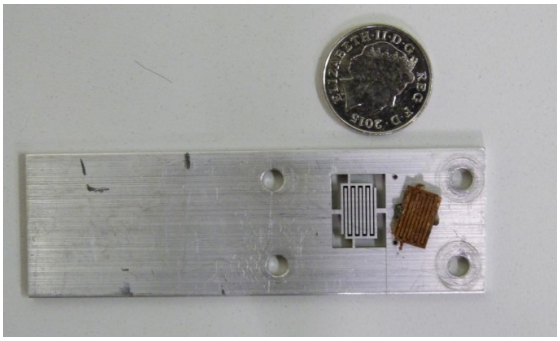

Figure 3.4 The interdigital capacitor sensor and the one of the aluminium strips that were used for sandwiching

A 1.2 mm thick copper sheet was used to fabricate the design and it was cut by electric discharge machine (EDM) called Agiecut® Vertex. As it shown in *figure 3.4*, two aluminium strips were used to sandwich the copper sheet for preventing the self-crimping during the machining and 50 micron tungsten wire was used in the cutting process. After that, the copper sample was embedded in PDMS to keep the fingers settled and then it was cut down from the supporting frame and connected out from two ends of the comb-structures by wire glue. After embedding into the PMDS, the actual capacitance of the sample is 12.67 pF, while the calculated capacitance is 9.545 pF. The reason for the difference between the actual and calculated capacitance is that the capacitance generated by fringing field and wires that connecting the sensor to the external device is neglected in the calculation. Finally the sample was bonded to a piece of tyre rubber sample by vulcanising fluid from Rema-tiptop and tested on MTS Landmark tensile machine.

In the first design, the stiffness of the sensor was the main problem. The capacitance of the sensor did not change much in the tensile test. It is believed that the reason for this situation was the thickness of fingers in the design was too large and the fingers had a significant effect

on the strain behaviour of the tyre sample. As a result, the fingers in the design barely moved when the tyre strained, therefore the changes in the capacitance could hardly be detected. What is worth mentioning, the cutting process took 5 hours to fabricate the interdigital structure, which means that EDM cutting process is not suitable for mass production due to the slow speed. Additionally, although the vulcanising fluid can build up an adhesion between the PDMS and rubber surfaces, the sensor still could be peeled off from the tyre rubber sample manually. Hence, a more reliable adhesion bonding method is also necessary.

3.3.2 Coplanar capacitor design

3.3.2.1 The theory of coplanar capacitor design

Inspired by the flexible printed circuit board (PCB), a developed design was carried out aiming at reducing the influence of the fingers on the tyre. The thickness of the fingers d_f was reduced to a sufficiently small value, which is 70 micron. Meanwhile, the gap between fingers a was decreased to 150 microns. This then changed the design into a coplanar structure, which means most of capacitance was contributed by the fringing field. *Figure 3.5* shows a schematic of the distribution of electric field in a coplanar capacitor with two strips.

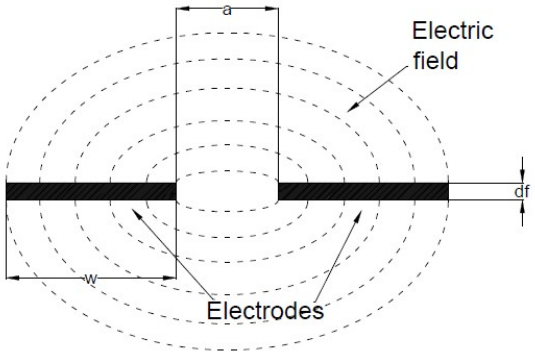

Figure 3.5 A schematic of the distribution of electric field in a pair of coplanar capacitor

Additionally, as it shown in *figure 3.6*, the connections between the fingers were also changed

into a spring shape to further reduce the stiffness of the whole sensor. The fingers, therefore, can move individually without the restriction of the side connections when strain occurs. Hence, the capacitance can only be changed by the distance between the metal strips, the strain in x direction will be have major effects on the capacitance and the strain in y direction which is generated by the Poisson effect cannot influence the overlapping of the fingers. So, two coplanar capacitor designs which are perpendicular with each other will be attached on the tyre surface for measuring the strains in x and y direction respectively. Therefore, only the relationship between the capacitance and strain in x direction will be calculated and analyzed as follows.

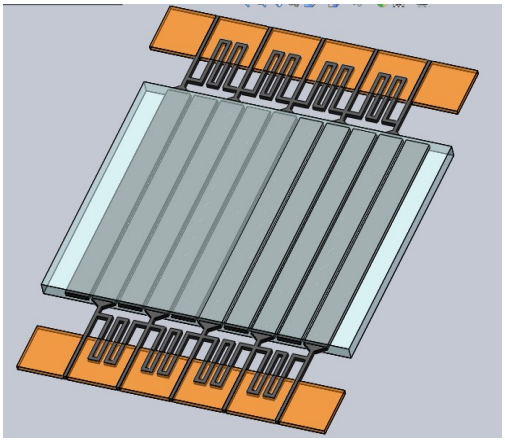

Figure 3.6 The coplanar capacitor design drawn in Solidworks

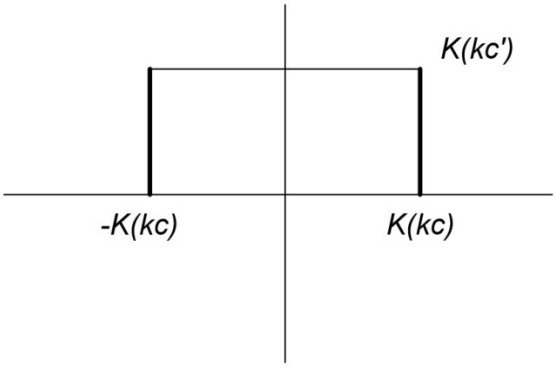

Figure 3.7 The rectangle structure that transferred from the non-uniform electric field based on Christoffel-Schowarz transformation [11]

For either upper half or bottom half of one pair of electrodes in the structure, employing the conformal mapping based on the Christoffel-Schwarz transformation can transfer the non-uniform electric field into a rectangle structure [11], which is shown in *figure 3.7*. Hence, the total capacitance C_{ci} is doubled for both sides of one pair of coplanar structure and it can be given by:

$$C_{ci} = 2 \cdot \varepsilon_0 \varepsilon_{PDMS} c \frac{K(k_c{}')}{2K(k_c)} = \varepsilon_0 \varepsilon_{PDMS} c \frac{K(k_c{}')}{K(k_c)} \qquad Eq.\,3.4$$

The capacitance of a coplanar capacitor design C_c is given below [11, 12]:

$$C_{c0} = (2n-1)C_{ci} = (2n-1)\varepsilon_0 \varepsilon_{PDMS} c \frac{K(k_c{}')}{K(k_c)} \qquad Eq.\,3.5$$

And:

$$k_c{}' = \sqrt{1 - k_c{}^2} \qquad Eq.\,3.6$$

where $K(k_c)$ is the total elliptic integral of the first kind and the elliptic integral k_c is given by:

$$k_c = \frac{a}{a + 2w} \qquad Eq.\,3.7$$

And:

$$F(k_c) = \frac{K(k_c{}')}{K(k_c)} = \begin{cases} \pi^{-1} \ln\left[2 \cdot \dfrac{1 + \left(1 - k_c{}^2\right)^{0.25}}{1 - \left(1 - k_c{}^2\right)^{0.25}}\right] & when\ 0 < k_c \leq 0.7 \\ \pi[\ln\,(2 \cdot \dfrac{1 + k_c{}^{0.5}}{1 - k_c{}^{0.5}})]^{-1} & when\ k_c \geq 0.7 \end{cases} \qquad Eq.\,3.8$$

where $w = 1\ mm$ is the width of the finger.

When a deflection Δx occurs, the capacitance can be given by:

$$C_{c,deflected} = (2n-1)\varepsilon_0 \varepsilon_{PDMS} c \frac{K(k_{c,deflected}{}')}{K(k_{c,deflected})} \qquad Eq.\,3.9$$

If the sensor is strained uniformly,

$$k_{c,deflected} = \frac{a + \Delta x \cdot \frac{a}{2nw + (2n-1)a}}{a + 2w + \Delta x \cdot \frac{a}{2nw + (2n-1)a}} \qquad Eq.3.10$$

3.3.2.2 Simulation on the coplanar capacitor design

Similarly with the interdigital capacitor design, the relationship between the strains in the x and y direction and the capacitance of the coplanar capacitor design is illustrated through MATLAB[4], which is shown in *figure 3.8*.

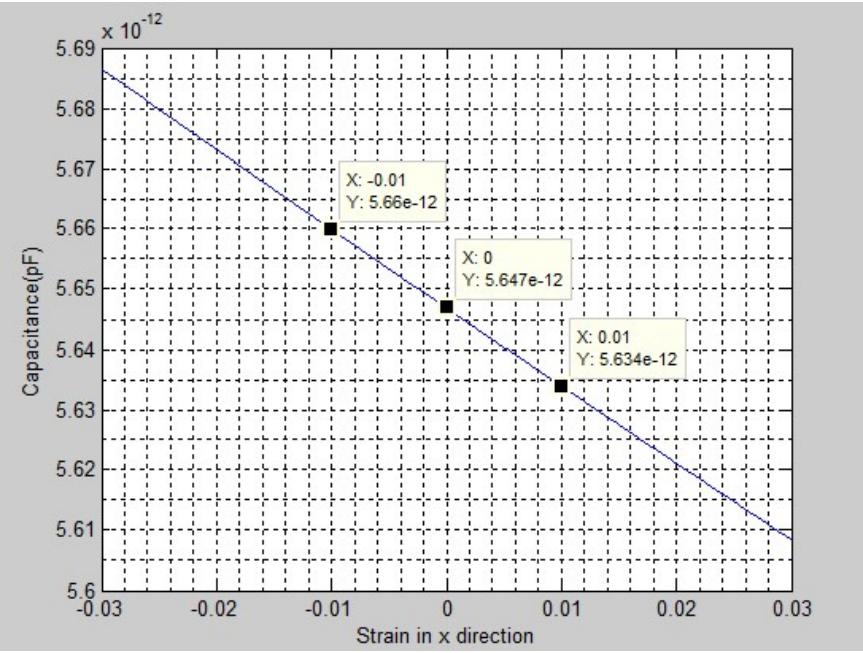

Figure 3.8 The calculated capacitance respect to the strain in x direction for coplanar capacitor design, in MATLAB

From *figure 3.8*, it can be seen that the capacitance is almost in a linear relationship with the strain. Different from the relationship in the interdigital capacitor design, the capacitance is in one to one correspondence with the strain, the capacitance keeps decreasing gradually from the compression condition (strain is in a negative value) to the extension condition (strain is in a positive value) in a similar trend.

[4] The MATLAB code is given in Appendix III

The calculated capacitance from the equations above is 5.647 pF, which is matched with the result from the figure. However, the capacitance does not change much when the sensor applied with a strain, which is 5.660 pF and 5.634 pF at -10000 and +10000 micron-strain, respectively. If the curve is treated as a straight line, the changing ratio could be calculated, which is 0.013 pF per 10000 micron-strain. Nonetheless, the figure is based on an assumption that the sensor is strained uniformly. In fact, the metal fingers are copper while the embedding material is PDMS and they will be compressed or extended in different ratios due to the different Young's modulus. So, this design is simulated in a finite element analyse software for a more accurate result as well.

COMSOL Multiphysics [13] was employed to simulate the designs in this chapter. As a finite element analyse software, COMSOL can simulate the coupled or multiple physics phenomena. Hence, it will be capable of simulating changes of capacitance of the sensor when applied a various deformation from the tyre.

Based on this design, a model was built and electromechanics module was selected to compare the results from simulation and calculation when a strain happening to the sensor. Since the connecting structure has minor effects on the straining behaviour of the sensor, the connecting spring structure is neglected in the COMSOL model, which also simplifies the structure and reduces the duration of computing.

What is worth mentioning is, in the mesh section, one surface of the design is meshed first,

which is the xy plane shown in the *figure 3.9*, and the whole structure is swept along the z axis to generate the whole mesh. This meshing method can reduce the computing duration and minimize the consumption of the memory while keep in the accuracy of the simulation.

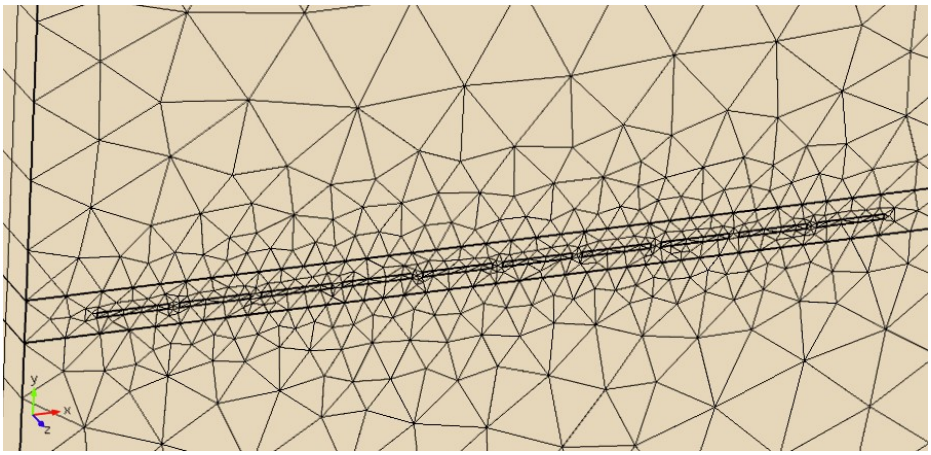

Figure 3.9 The mesh method for coplanar capacitor design in COMSOL Multiphysics

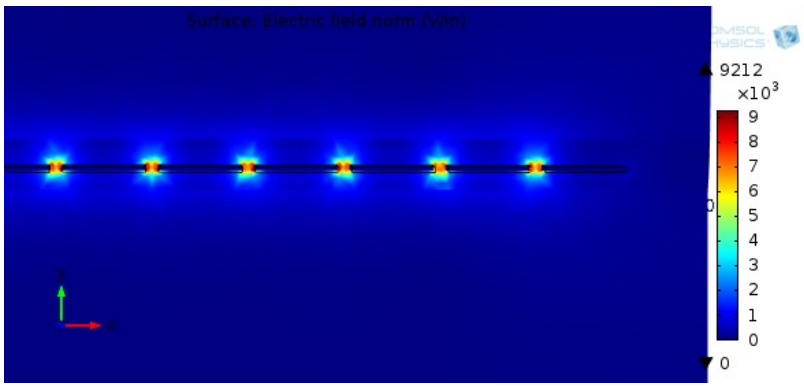

(a)

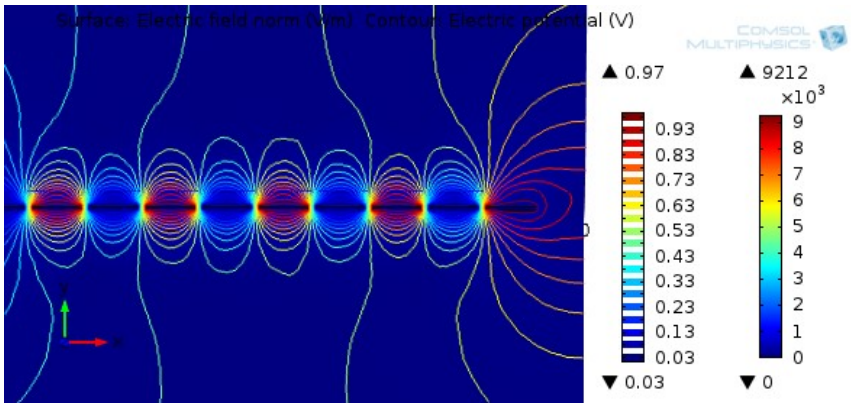

(b)

Figure 3.10 The electric field distribution (a) and equipotential contours (b) when zero strain for coplanar capacitor design in COMSOL Multiphysics

From the result of the simulation, the electric field distribution and equipotential contours when zero strain are presented in *figure 3.10 (a)* and *(b)*. *Table 3.1* and *figure 3.11* also are illustrated to compare the results between the simulations and calculations. From *figure 3.10 (a)*, the electric fields around the fingers concentrate in the gaps, which means most of the capacitance is still contributed by the facing areas between the fingers rather than the coplanar surfaces. As shown *table 3.1* and *figure 3.11*, it is found that although capacitance in the simulation is slightly smaller than that in the calculation, the simulated capacitance changed almost linearly with respect to the strain, which matches with the results from the calculation

in MATLAB. And the changing rate of capacitance becomes acceptable: the difference of the capacitance between the zero strain and 10,000 micro strains was approximately 0.018 pF.

Table 3.1 The comparison of capacitance in simulation and calculation respect to strain for coplanar capacitor design

Strain (micro-strain)	Capacitance in simulation (pF)	Capacitance in calculation (pF)
-10000	5.1812	5.660
-8000	5.1776	5.657
-6000	5.1741	5.655
-4000	5.1706	5.652
-2000	5.1671	5.649
0	5.1636	5.647
2000	5.1601	5.644
4000	5.1566	5.642
6000	5.1531	5.639
8000	5.1497	5.637
10000	5.1496	5.634

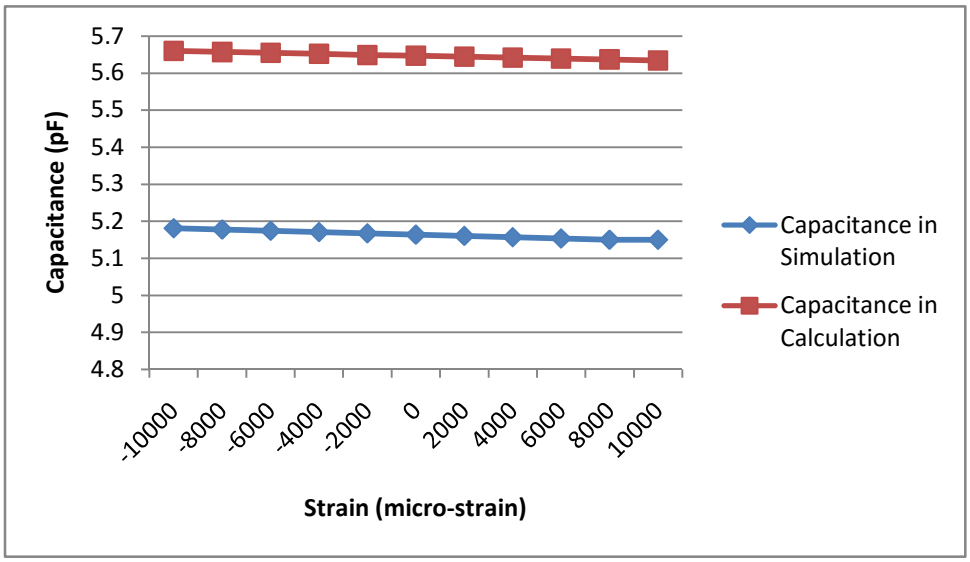

Figure 3.11 The comparison of the capacitance respect to strain in simulation and calculation for coplanar capacitor design

Compared with the interdigital capacitor design, the coplanar capacitor design has less capacitance and lower changing rate, which results in less sensitivity. Meanwhile, from the results in simulation, the thickness of fingers in the design is still too large to generate a capacitance in coplanar surfaces, and the metal material takes most of the percentage in the sensing area, which both results of a potential problem on the stiffness. Hence, it can be inferred that the coplanar capacitor design might be still not suitable for measuring the strain in tyres. Nonetheless, from the calculation and simulation based on this design, it can be noticed that without the stiff connections between the strips, the capacitance of coplanar design has one to one correspondence relationship with strain. This concept has a contribution to the bond wire capacitor, which will be introduced in next section.

3.3.3 Bond wire capacitor design

3.3.3.1 Concept and geometry of the bond wire capacitor design

Compared with the interdigital design, the coplanar design reduced the thickness of fingers and the gaps between them. However, the capacitance of the sensor was simultaneously decreased and the sensitivity to the strain was also affected while the stiffness of the sensor is still a potential problem. Increasing the capacitance by simply increasing the number of fingers might increase the capacitance and sensitivity but the size of the sensor will be expanded and it will become difficult to detect the tyre strain in a small area.

So, the bond wire capacitor design was carried out, in which not only the number of fingers was increased, but the width of fingers was also reduced to a very small value to control the size of the sensor in a reasonable value and minimize the stiffness of the structure. It can also be considered that the fingers in the two comb structures were re-designed to be two arrays of wires, which is shown in *figure 3.12*. This structure can be produced by wire bonding process. Wire bonding process is normally used to make electrical connection from metal bond pads in an integrated circuit (IC) chips to lead frames in microelectronics [14]. Gold, copper and aluminium are commonly employed as the material for the bond wires. There are two main classes for the wire bonding process, which are ball bonding and wedge bonding. However, in both of them the weld at each wire is formed by pressure and ultrasonic energy of the bonding head [15, 16] while for gold wires, some heat energy might be employed. It is typically using wires with diameter in the range of 15 to 75 micrometres. As will be introduced in Chapter 4, a bondjet BJ 820 automatic wedge bonder from HESSE Mechatronics is employed for the

bond wire capacitor design and the wires used for the process are aluminium wires with 25 micron diameter.

There are four metal strips designed for the 'bond landings'. Blue wires (in one array) are connected together by strip 1 and 3 while the rest of the wires, which are black wires (in the other array), are connected by strip 2 and 4. Besides, the strip 1 and 4 can be connected out as two electrodes of this design. The distance between strip 1 and 3 or strip 2 and 4 is 6 mm and the length of the strips is 8 mm. While the gap between strip 1 and 2 or strip 3 and 4 should be minimized to acquire a maximum overlaps for the two wire arrays, it is originally designed to be 150 micron and the spacing between the wires is 100 microns.

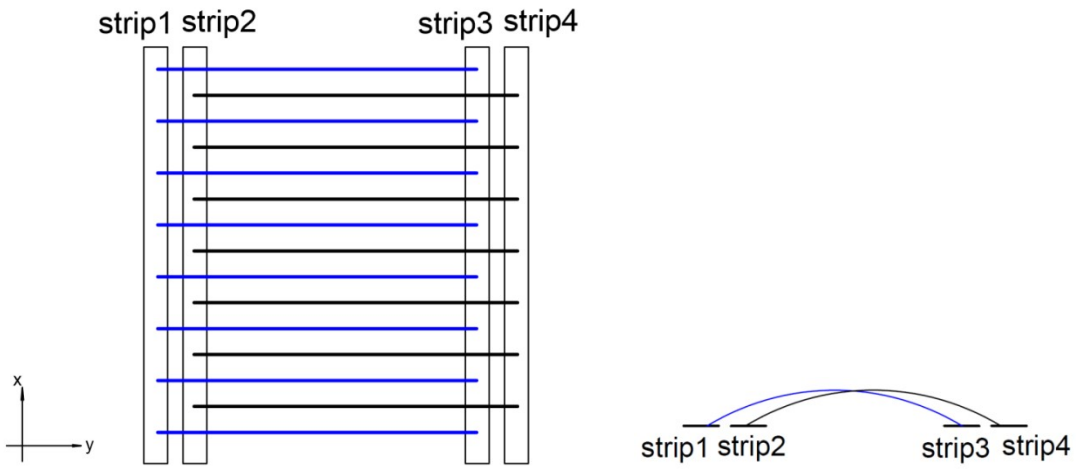

Figure 3.12 A schematic of bond wire capacitor design in top view (a) and front view (b)

Similar with the coplanar capacitor design, bond wire capacitor design is only sensitive to the strain in the x direction. Since both ends of the wires are bonded on the strips, the strain in the y direction cannot change the overlapping area of the wires. So the following calculation and

simulation will only consider the strain in x direction. Meanwhile, the distance between the adjacent strips is incomparable with the length of the wire, the two wire arrays are considered as fully overlapped with each other.

3.3.3.2 Calculation on the bond wire capacitor design

It is a challenge to find out capacitance of the bond wire capacitor design and in order to estimate the capacitance between two wire-arrays C_a, the capacitance between two single wires will be investigated first.

Imagine two infinite long wires are applied a voltage V and these wires will carry a charge of q and $-q$ coulomb per metre (C/m). Hence, the capacitance between the two wires C_E is given by:

$$C_E = \frac{q}{V} \qquad Eq.3.11$$

Then a Cartesian coordinate system is built based on the location of the wires as shown in *figure 3.13*.

If these two wires are replaced by two equivalent line charges, then the distance between these two charges is defined as $2m$. And the potential along the y axis is zero.

Hence, the potential ϕ of a point $P(x, y)$ can be given by [17]:

$$\phi = \int_{r_1}^{m} \frac{q}{2\pi\varepsilon r} dr + \int_{r_2}^{m} \frac{-q}{2\pi\varepsilon r} dr = -\frac{q}{2\pi\varepsilon} ln\frac{r_1}{r_2} \qquad Eq.3.12$$

Where $\varepsilon = \varepsilon_0\varepsilon_{PDMS}$ in this case and r_1, r_2 are the distances from P to two line charges, respectively.

So,

$$(x+m)^2+y^2=r_1^2 \qquad Eq.3.13$$

$$(x-m)^2+y^2=r_2^2 \qquad Eq.3.14$$

If a coefficient k is defined as:

$$k=\frac{r_1}{r_2} \qquad Eq.3.15$$

Then

$$k^2=\frac{r_1^2}{r_1^2}=\frac{(x+m)^2+y^2}{(x-m)^2+y^2} \qquad Eq.3.16$$

This expression can be written in a function of x and y:

$$x^2-2m\frac{k^2+1}{k^2-1}x+y^2+m^2=0 \qquad Eq.3.17$$

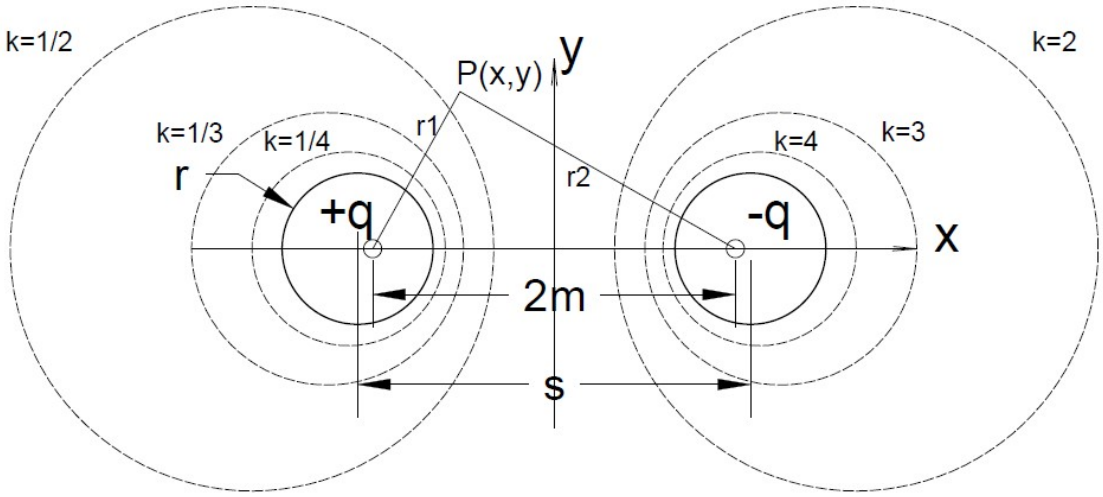

Figure 3.13 A schematic of equipotential contours around two infinite long wires

From equation $Eq.3.13$, equipotential contours can be determined when k equals to different values, which is shown in *figure 3.13*. Meanwhile, for the left wire, the function of the outline of the wire is given by:

$$(x+\frac{s}{2})^2+y^2-r^2=0 \qquad Eq.3.18$$

After expansion

$$x^2 + sx + y^2 + \frac{s^2}{4} - r^2 = 0 \qquad Eq.3.19$$

where r is the radius of the wire and s is the spacing between the wires.

As it known, the potential of every point on the surface of the wire is equivalent. Hence, the surface of the wire is one of the equipotential contours, which means the coefficient k has to satisfy:

$$-2m\frac{k^2+1}{k^2-1} = s \qquad Eq.3.20$$

and

$$m^2 = \frac{s^2}{4} - r^2 \qquad Eq.3.21$$

So k can be expressed by:

$$k = \frac{s-2m}{2r} = \frac{s-\sqrt{s^2-4r^2}}{2r} \qquad Eq.3.22$$

Hence the potential at the left wire ϕ_{left} is given by:

$$\phi_{left} = -\frac{q}{2\pi\varepsilon} ln\left(\frac{s-\sqrt{s^2-4r^2}}{2r}\right) \qquad Eq.3.23$$

As the electric field is symmetric, the potential at the right wire ϕ_{right} is given by:

$$\phi_{right} = -\phi_{left} \qquad Eq.3.24$$

So the voltage V between the wires is given by:

$$V = \phi_{left} - \phi_{right} = 2\phi_{left} \qquad Eq.3.25$$

Hence from equation $Eq.3.11$, $Eq.3.23$ and $Eq.3.25$ the capacitance between the wires is given by:

$$C_E = \frac{q}{-\frac{q}{\pi\varepsilon} ln\left(\frac{s-\sqrt{s^2-4r^2}}{2r}\right)} = -\frac{\pi\varepsilon L}{ln\left(\frac{s-\sqrt{s^2-4r^2}}{2r}\right)} \qquad Eq.3.26$$

where L is length of the wire.

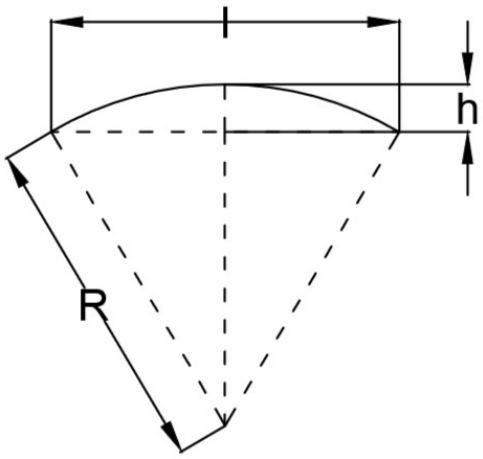

Figure 3.14 The schematic diagram of the aluminium wire in the bond wire capacitor design

As shown in *figure 3.14*, if the wire curve can be treated as an arc and the height of the curve is h, the radius of the arc R can be solved by:

$$R^2 = \left(\frac{l}{2}\right)^2 + (R-h)^2 \qquad Eq.3.27$$

Hence, R is given by:

$$R = \frac{l^2 + 4h^2}{8h} \qquad Eq.3.28$$

Where l is the distance between the strip 1 and 3 (strip 2 and 4) and h is the height of the wire bonding.

So, L is given by:

$$L = 4R\,\pi \sin^{-1}\frac{\frac{l}{2}}{R} = \frac{l^2 + 4h^2}{2h}\pi \sin^{-1}\frac{4hl}{l^2 + 4h^2} \qquad Eq.3.29$$

In the bond wire capacitor design, the electrical field in the wires will not be generated as that in a pair of wires but only at both ends of the array. Hence, the wire array cannot be considered as a summation of multiple pairs of capacitors in a parallel connection. In the middle area, the electrical field can be equivalent with a coplanar design as introduced in Section 3.3.2. And according to the theory that introduced in the section, only half of the

capacitance of the design is taken into consideration. So the total capacitance that the whole structure generates is doubled.

The capacitance that generated by the ends of the array is equivalent as $\frac{C_E}{2}$. Hence, the capacitance of the wire array C_a is given by [12]:

$$C_a = 2 \cdot \left[(N-3)\frac{C_{aI}}{2} + 2\frac{C_E C_{aI}}{C_E + 2C_{aI}} \right] \qquad Eq.3.30$$

where N is the total number of the wires and C_{aI} the capacitance of one electrode to the ground potential for half of the structure is given by:

$$C_{aI} = \varepsilon_0 \varepsilon_{PDMS} c \frac{K(k_a{}')}{K(k_a)} \qquad Eq.3.31$$

And k_a can be given by:

$$k_a = \frac{s-2r}{s+2r} \qquad Eq.3.32$$

When a deflection Δx or a strain $\varepsilon_{\text{strain}}$ occurs, and if the sensor is deformed uniformly, the deflection between each wire Δx_i can be given by:

$$\Delta x_i = \varepsilon_{\text{strain}}(s-2r) = \Delta x \cdot \frac{s-2r}{2Nr + (2N-1)(s-2r)} \qquad Eq.3.33$$

the capacitance of the wire array $C_{a,deflected}$ is given by:

$$C_{a,deflected} = 2 \cdot \left[(N-3)\frac{C_{aI,deflected}}{2} + 2\frac{C_{E,deflected} C_{aI,deflected}}{C_{E,deflected} + 2C_{aI,deflected}} \right] \qquad Eq.3.34$$

where

$$C_{aI,deflected} = \varepsilon_0 \varepsilon_{PDMS} c \frac{K(k_{a,deflected}{}')}{K(k_{a,delfected})} \qquad Eq.3.35$$

$$k_{a,deflected} = \frac{s-2r+\Delta x_i}{s+2r+\Delta x_i} \qquad Eq.3.36$$

and

$$C_{E,deflected} == -\frac{\pi \varepsilon L}{ln\left[\frac{(s+\Delta x_i) - \sqrt{(s+\Delta x_i)^2 - 4r^2}}{2r}\right]} \qquad Eq.3.37$$

What has to be mentioned is, there are some reasonable assumptions made to estimate the capacitance, the two arrays of wires are treated as fully overlapped and the wire curve is considered as an arc. Meanwhile, any effects due to the curving wires are neglected.

3.3.3.3 Simulation on the bond wire capacitor design

Due to the requirements of stability and reliability in the fabrication process, the bond wire capacitor design was developed based on the original concept, which will be presented in details in Section 4.4. In the original design, the bond wire capacitor design consists of two wire arrays, and each array is connected to its individual electrode. While in the developed design, there are two completely separate wire arrays and each of array can generate a capacitance. Moreover, in each of them, the wires are fully overlapped. Hence, the simulation and calculation will base on the developed bond wire capacitor design and results obtained from both simulation and calculation will be compared in this section.

Similar with coplanar structure design, electromechanics module was selected to simulate and evaluate the capacitance for bond wire capacitor design.

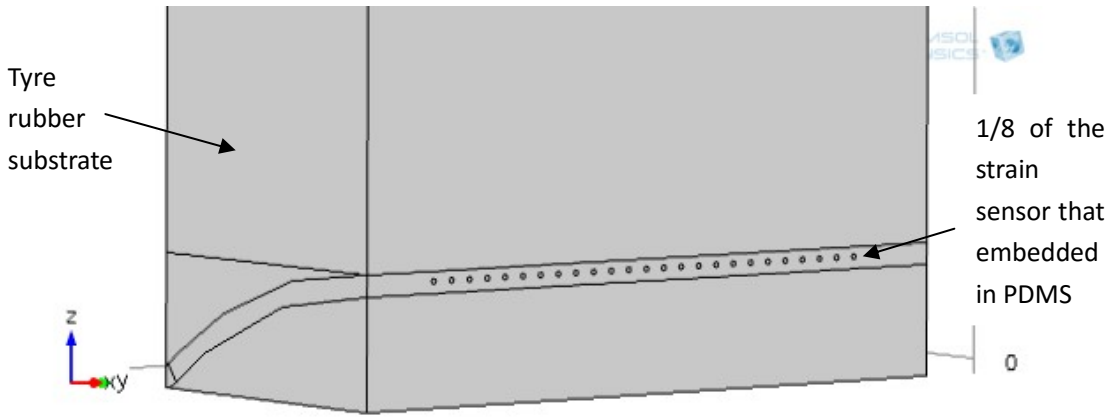

Figure 3.15 One quarter of a wire array for bond wire capacitor design in COMSOL Multiphysics

Due to multiple wires and relatively small dimensions of the wires, the simulation will be extremely complicated and time-consuming and also limited by the memory of the computer. It is impossible to simulate the behaviour of the whole design. Hence, the simplification for the simulation appears to be very significant. As will be introduced in Section 4.4, there are two separated same wires arrays in the design, so only one array is taken into consideration in the simulation. Additionally, due to the symmetry of the wire array, only a quarter of the wire array is simulated, which is shown in *figure 3.15*. By splitting the whole structure, only 1/8 of the actual sensor is simulated and the simulation process was simplified as much as possible.

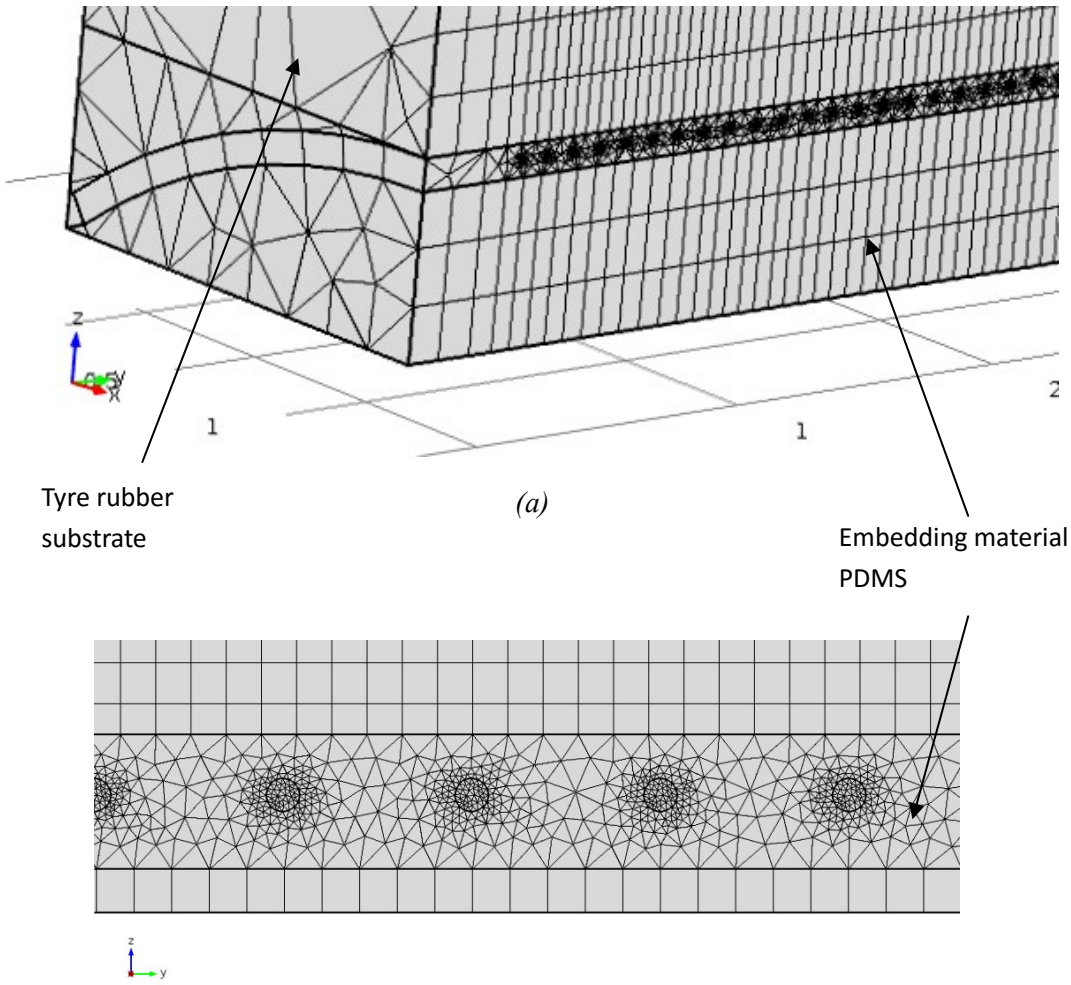

Figure 3.16 The mesh method for bond wire capacitor design in COMSOL Multiphysics, (a) two meshing directions, (b) the meshing around the wires

The meshing process will be vital as well in the simulation, the elements has to be generated as fine as possible to express the real situation. However, the finer the mesh is, the more complicated calculations and simulating duration will be brought. Hence, as shown in *figure 3.16 (a)*, there are two sweeping directions employed in the mesh process, in which one is along the direction of the wires and the PDMS around these wires, the other is perpendicular to the first direction and meshing the rest of PDMS and attached tyre rubber piece. As a result, areas of wires and the PDMS around the wires are in finer meshing, which is shown in *figure*

3.16 (b), while the areas of the rest of PDMS, which are the less important, are in a relatively coarser meshing. What is worth mentioning is, limited by the memory of the computer, the displacement is applied to one side of the substrate while the other side is fixed.

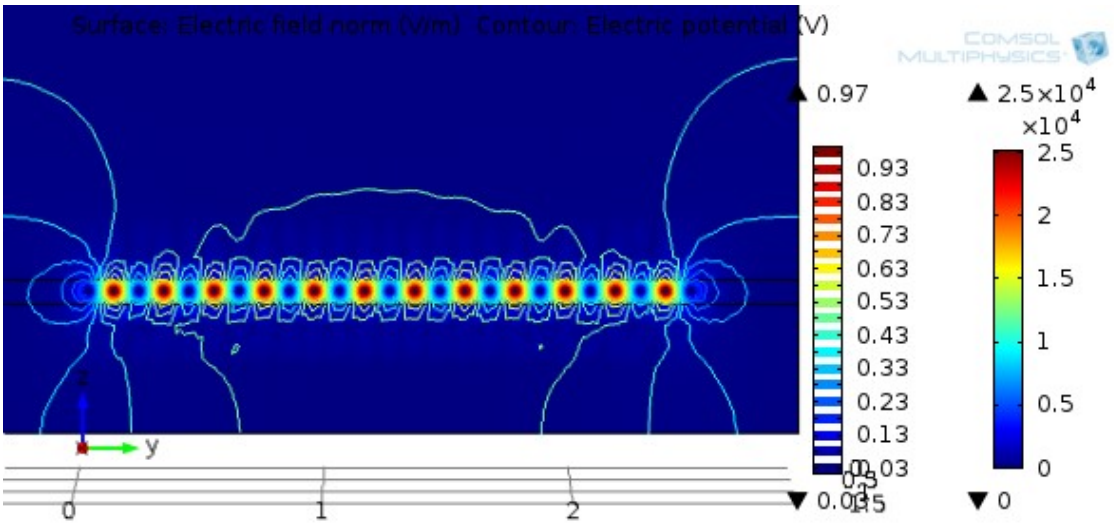

Figure 3.17 The electric field distribution and equipotential contours at zero strain in bond wire capacitor design in COMSOL Multiphysics

The electric field distribution and equipotential contours from the result of the simulaiton when strain equals zero are shown in *figure 3.17*. As it shown, the equipotential contours in the bond wire capacitor design are similar with that in the coplanar capacitor design, which supports the assumption in Section 3.3.3.2. And the capacitance from the simulation and calculation are illustrated in *table 3.2* and *figure 3.18*.

Table 3.2 The comparison of capacitance in simulation and calculation respect to strain for bond wire capacitor design

Strain (micro-strain)	Capacitance in simulation (pF)	Capacitance in calculation (pF)
-10000	7.6557	8.8351

-8000	7.6521	8.8284
-6000	7.6485	8.8216
-4000	7.6450	8.8149
-2000	7.6415	8.8082
0	7.6380	8.8016
2000	7.6345	8.7950
4000	7.6310	8.7884
6000	7.6276	8.7818
8000	7.6241	8.7752
10000	7.6207	8.7687

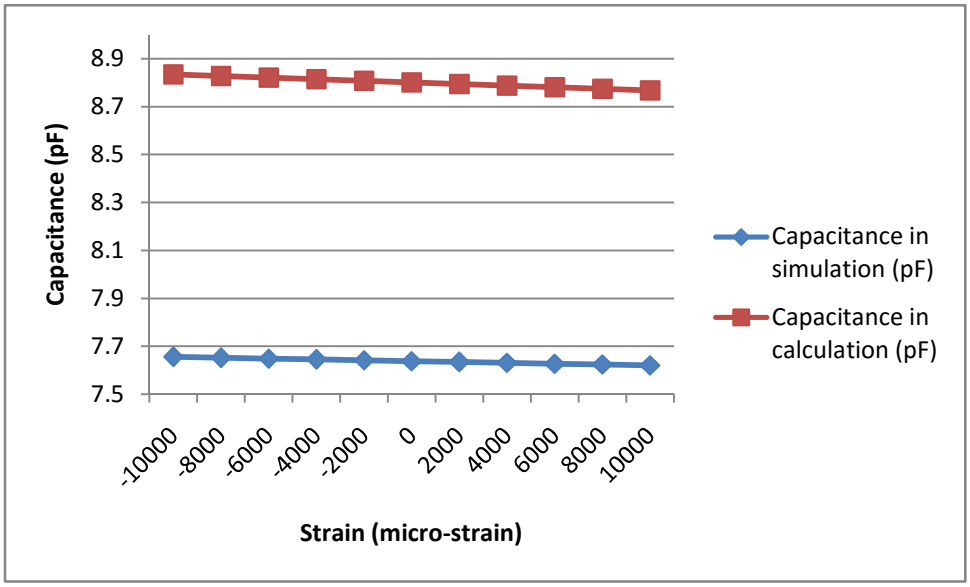

Figure 3.18 The comparison of the capacitance respect to strain in simulation and calculation for bond wire capacitor design

The simulated capacitance of the bond wire capacitor design is slightly smaller than calculated, which is similar with the coplanar design. However, the total capacitance and the

difference between zero strain and 10000 micro-strain are increased, which are 8.802 pF and 0.036 pF in calculation and 7.638 pF and 0.018 pF in simulation. The discussion on the difference of the results between the calculation and the simulation will be presented in Section 5.3.4.

Compared with the coplanar structure, the capacitance of the bond wire capacitor is also in a linear-like relationship with the strain. However, the bond wire capacitor design minimizes the stiffness of the sensor by employing arrays of tiny wires with only 25 micron diameter, while increasing the capacitance and retains the sensitivity. Hence, the bond wire capacitor is selected as the final design for the tyre strain sensor.

3.4 Conclusions

In this chapter, the sensor design process was presented. In the beginning, two main design concepts were introduced, which are interdigitated structure and PDMS embedding. Both of the concepts were employed in all of the potential designs and there were three tyre strain sensor designs were presented, which are interdigital capacitor design, coplanar capacitor design and bond wire capacitor design. For these three design, calculation and simulation were given in all of these three design. MATLAB was employed in the calculation while COMSOL Multiphysics was employed in the simulation. The total capacitance and the sensitivity for each design were presented and compared as well.

Stiffness of the sensor is still the most significant problem in the interdigital capacitor and

coplanar capacitor designs. As the first design, interdigital capacitor design had a reasonable initial capacitance, which was 9.545 pF. The fabrication process of interdigital structure design was briefly presented as well. However, due to the adhesion bonding method and the stiff structure of itself, no meaningful measurement was recorded. Coplanar capacitor design decreased the thickness of the fingers compared to the previous design to a very small value. The initial capacitance was influenced and dropped to approximately 5 pF. Improved from the interdigital capacitor design, the capacitance in the coplanar capacitor design was in a linear-like relationship with respect to the strain from compression to extension. Meanwhile, the fingers in the design can move individually due to the flexible connection between them, which make the sensor only sensitive to one direction. From the result of simulation, it was found that the electric field distributed in the gaps between the fingers. And the metal material in the design took most of the percentages in the sensing area. Both of the factors might result of high stiffness of the sensor.

Bond wire capacitor design was carried out as the final design. By employing the small wires and embedding the sensor into PDMS, the design minimizes the stiffness and maintains an acceptable capacitance (approximately 8 pF) and sensitivity. The next chapter will mainly introduce the fabrication process of the bond wire capacitor. And according to the limitation and optimization in each fabricating step, a developed bond wire capacitor will be presented.

Reference

1. Matsuzaki, R., et al., *Rubber-based strain sensor fabricated using photolithography for intelligent tires.* Sensors and Actuators a-Physical, 2008. **148**(1): p. 1-9.
2. Matsuzaki, R. and A. Todoroki, *Wireless flexible capacitive sensor based on ultra-flexible epoxy resin for strain measurement of automobile tires.* Sensors and Actuators A: Physical, 2007. **140**(1): p. 32-42.
3. Matsuzaki, R., et al., *Analysis of Applied Load Estimation Using Strain for Intelligent Tires.* Journal of Solid Mechanics and Materials Engineering, 2010. **4**(10): p. 1496-1510.
4. Cole, D.J. and D. Cebon. *A capacitative strip sensor for measuring dynamic type forces*. in *Road Traffic Monitoring, 1989., Second International Conference on*. 1989.
5. Bingger, P., M. Zens, and P. Woias, *Highly flexible capacitive strain gauge for continuous long-term blood pressure monitoring.* Biomedical Microdevices, 2012. **14**(3): p. 573-581.
6. Ong, J.B., et al., *A Wireless, Passive Embedded Sensor for Real-Time Monitoring of Water Content in Civil Engineering Materials.* Ieee Sensors Journal, 2008. **8**(11-12): p. 2053-2058.
7. Armani, D., C. Liu, and N. Aluru, *Re-configurable fluid circuits by PDMS elastomer micromachining.* Mems '99: Twelfth Ieee International Conference on Micro Electro Mechanical Systems, Technical Digest, 1999: p. 222-227.
8. Zhu, L. and K. Wu, *Accurate circuit model of interdigital capacitor and its application to design of new quasi-lumped miniaturized filters with suppression of*

harmonic resonance. Microwave Theory and Techniques, IEEE Transactions on, 2000. **48**(3): p. 347-356.

9. Gevorgian, S.S., et al., *CAD models for multilayered substrate interdigital capacitors.* Microwave Theory and Techniques, IEEE Transactions on, 1996. **44**(6): p. 896-904.

10. Farcich, N.J., J. Salonen, and P.M. Asbeck, *Single-Length Method Used to Determine the Dielectric Constant of Polydimethylsiloxane.* Microwave Theory and Techniques, IEEE Transactions on, 2008. **56**(12): p. 2963-2971.

11. Vendik, O.G., S.P. Zubko, and M.A. Nikol'ski, *Modeling and calculation of the capacitance of a planar capacitor containing a ferroelectric thin film.* Technical Physics, 1999. **44**(4): p. 349-355.

12. Igreja, R. and C.J. Dias, *Analytical evaluation of the interdigital electrodes capacitance for a multi-layered structure.* Sensors and Actuators a-Physical, 2004. **112**(2-3): p. 291-301.

13. *COMSOL Multiphysics https://uk.comsol.com/comsol-multiphysics.*

14. Xu, H., et al., *Growth of intermetallic compounds in thermosonic copper wire bonding on aluminum metallization.* Journal of Electronic materials, 2010. **39**(1): p. 124-131.

15. Shah, A., et al., *In situ ultrasonic force signals during low-temperature thermosonic copper wire bonding.* Microelectronic Engineering, 2008. **85**(9): p. 1851-1857.

16. Liu, Y., S. Irving, and T. Luk, *Thermosonic wire bonding process simulation and bond pad over active stress analysis.* Electronics Packaging Manufacturing, IEEE Transactions on, 2008. **31**(1): p. 61-71.

17. *Electroquasistatic Fields in the Presence of PerfectConductors*. Available from: http://web.mit.edu/6.013_book/www/chapter4/4.6.html.

Chapter Four.
Fabrication Process on Bond Wire Capacitor Design

4.1 Introduction

In the last chapter, the bond wire capacitor design is determined as the final design. Hence, the fabrication process of the design will be presented in this chapter. A flexible PCB is employed as the substrate material of the sensor, and the fabrication process consists of PCB pattern fabrication, wire bonding and PDMS embedding. In the pattern fabrication, wet etching method and laser machining method were both employed.

From the design in Chapter 3, the PCB pattern was originally fabricated by a wet-etching process, and there were two bonding steps adopted to complete the capacitive structure. And then, the whole structure was embedded in PDMS for protecting the sensor from potential external damage and to minimize the stiffness of the overall structure. However, during the fabrication, the requirements on the stability and the limitation of each process have many effects on and interact with the details of the design. Therefore, the design was developed based on the original one, and the PCB fabrication and wire bonding process was adjusted correspondingly. So in this chapter, the first attempt of the sensor fabrication, which is a general method, will be introduced firstly based on the design in Chapter 3. After that, the potential problems and limitation in each step will be analysed, and then improvement and optimization on these steps will be discussed, a re-designed sensor will follow. Finally, a final design will be carried out to maximize the stability in the fabrication while keeping a

reasonable capacitance. And also the final fabrication process based on this design will be presented.

4.2 Sensor fabrication process based on the original design

4.2.1 Fabricating PCB pattern for wire bonding—wet etching method

To achieve the wire bonding process, the surface of the bonded pattern/chip has to be metallic. Also due to the requirement of the flexibility of the sensor, the bonding surface has to be flexible, so a flexible PCB is employed as the substrate material of the sensor. However, in majority of normal PCBs the metal layer is made of copper, and during the wire bonding process a tenacious oxide layer will be generated on the copper surface by the ultrasonic energy, which reduces the bonding strength and bonding quality [1, 2]. In order to avoid this, a special flexible PCB called Pyralux AP flexible circuit material from DuPont is selected, which is specifically designed to allow wire bonding directly to the copper to achieve the best bonding strength and bonding quality. The material is a double-sided, copper-clad laminate while the all-polyimide composite of polyimide film is bonded to copper surface [3]. The thickness of the copper layer is 35 micron while the thickness of the polyimide layer between the copper laminates is 2 mils, which is 50.8 microns. The polyimide film makes the material capable of being wire bonded and will not affect any process on the material during the whole fabrication.

The pattern on the flexible PCB can be produced by different methods. Wet etching in ferric chloride, as one of the most common methods in PCB fabrication in research and industry

[4-6], is employed.

To etch down the specific pattern on the copper laminate, a photolithography technique is employed. From the bond wire capacitor design in Section 3.3, a mask for the copper pattern was designed as shown in *figure 4.1*. The mask was printed on the transparent paper by a HP Color LaserJet CP2025 Printer [7] and two identical masks were fully overlapped and bonded together by superglue to strengthen the features on the pattern. The mask consists of four disconnected strips; strip 1 and 3 would be connected by bond wires as an electrode while strip 2 and 4 would be connected by bond wires as the other electrode. The length of each strip was 8 mm while the width between strip 1 and 3 as well as strip 2 and 4 was 6 mm. The gaps between strip 1 and 2 as well as strip 3 and 4 were 150 micron. The two pads on strip 1 and 4 were used for connecting the sensor to external circuits. What is worth mentioning is that the area around the pattern was not designed to be removed, which not only reduced the etching area for quicker process but increased the stiffness of the whole sample to support itself during the subsequent wire bonding process.

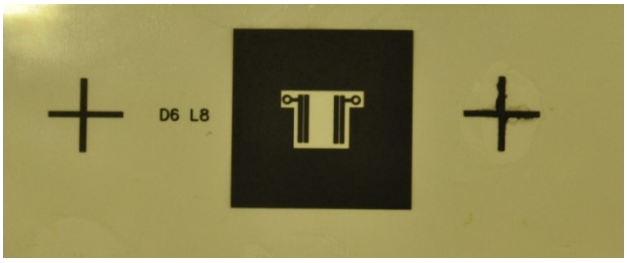

Figure 4.1 Mask for photolithography process in wet etching method

One side of the copper layer of the flexible PCB material was removed in 10% ferric chloride solution, as shown in *figure 4.2 (b)*, and the etched surface was bonded to the silicon wafer by thermal release tape as shown in *figure 4.2 (c)*. Then the photoresist S1813 was poured on the wafer and it was span at 500 rpm for 10 sec, 2000 rpm for 30 sec, 500 rpm for 10 sec

continuously and baked on the hot plate at 80℃ for 30 minutes, as shown *in figure 4.2 (d)*. After that, the sample was exposed under the mask in *figure 1* for 8 seconds and developed in MF-319 for 15 minutes at room temperature, as shown in *figure 4.2 (e)*. The normal developing duration for MF-319 is approximately 2 minutes, however, the exposed photoresist S1813 cannot be fully developed in 2 minutes, which probably results of extending the wet etching duration and damaging the features in the design. The sample with the pattern on then was rinsed in de-ionised water for 2 min for cleaning and finally etched in 10% ferric chloride solution for 45 min to 1 hour, as shown in *figure 4.2 (f)*. The un-developed photoresist was removed by soaking the sample in 1165 remover at 80 ℃ for 10 minutes, as shown in *figure 4.2 (g)*.

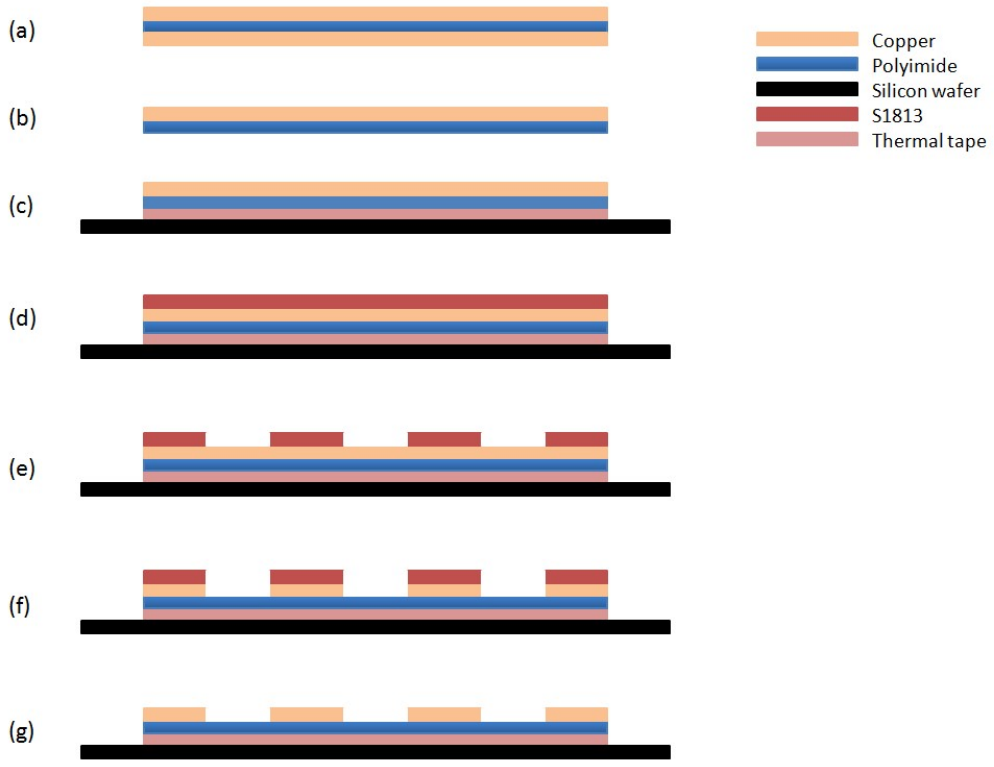

Figure 4.2 A schematic diagram of wet etching method, in which (a) the flexible PCB substrate, (b) removing one side of the copper, (c) bond to silicon wafer, (d) coating a S1813 photoresist layer, (e) expose and develop, (f)removing down the pattern, (g) removing the

photoresist layer

4.2.2 Wire bonding process

Wire bonding is widely employed in the microelectronic's industry to connect various types of substrate, chip and other materials in micro scaled range. In this process, a bondjet BJ 820 automatic wedge bonder from HESSE Mechatronics was used. Each pair of strips was connected by 25 micron aluminium wires as an electrode of the capacitor, so two bonding steps were needed and each of steps produced a wire array. The spacing in each wire array was set to be 200 micron. Each array consisted of 40 wires, which means 80 wires in total were evenly interdigitated into each other. Therefore the spacing between the wires was 100 micron.

In order to avoid wire touching with each other and the short cut of the capacitor, the parallelism of the wire array is the crucial point in this process. The wire length and the bond height have significant effects on the parallelism. Reducing the wire length can dramatically increase the parallelism of the bonding array, but it will also correspondingly reduce the capacitance of the sensor. From the bonding tests (more detailed wire bonding trials will be discussed in Section 4.3.2) that regarding a fixed 6 mm bond length, it is found that shallow bonds, which are normally set approximately 300 microns high, can cause some twisted and bended wires or even failure ones, while high bonds (over 1000 microns) will also be misaligned by the wedge shaped bonder. So, the bond height was finally set to be 900 micron. Additionally, it was also found that reducing the bonding speed was also helpful to straighten the wires.

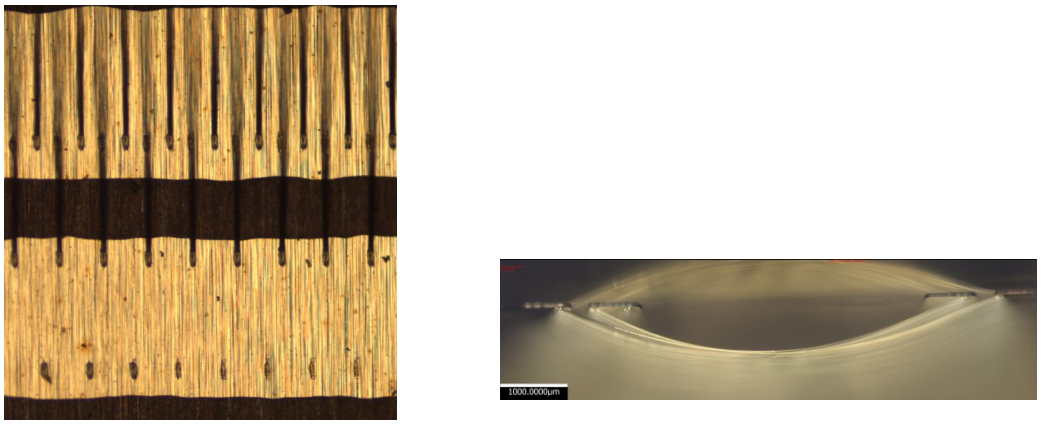

(a) *(b)*

Figure 4.3 Bonding feet in four strips pattern (a) and side view of the bonding wires (b)

In order to increase the overlapping of the wires for maximizing the capacitance of the sensor, the bonding feet in these two arrays of wires have to be closed to each other as much as possible. So as shown in *figure 4.3 (a)*, the bonding feet were set at edge of the strip and *figure 4.3 (b)* shows the side view of the bonding wires.

4.2.3 Embedding process

As introduced in literature review, PDMS has already used in a wide range of applications by different researchers. Due to its particularly the low stiffness compared to tyre rubber, its dielectric properties and the ability to be easily moulded, polydimethysiloxane (PDMS) is selected as the embedding material. Embedding the sensor into PDMS provides the sensor with enough protection from the potential damage while keeping the flexibility of the sensor. Before curing, PDMS is a liquid material which has a high viscosity. However, it will become a complaint solid after mixing with the curing agent for 24 hours at room temperature or for

approximately 20 min at 80 ℃. These characteristics makes PDMS be an ideal material for moulding and embedding process for the design.

The embedding process is the final step of the fabricating process. As shown in *figure 4.4*, a square frame with 24 mm inner edge was built by LEGO bricks and bonded to the silicon wafer by PDMS, which formed a mould that can surround the bond wire structure inside, as shown in *figure 4.5 (b)*. Since the area is in a square shape and wire height is known, the volume of PDMS can be calculated, which is approximately 0.58mL for making a 1 mm thick PDMS layer that will cover the bond wires. As shown in *figure 4.5 (c)*, PDMS was injected by a syringe with 1mL capacity and 0.01mL precision into the mould. There were some small bubbles produced because of mixing PDMS with the curing agent, so before the injecting, the syringe was put up side down for an hour to release these bubbles. After that, the sample piece was put in room temperature for 24 hours for curing. Then, the LEGO bricks were removed from the wafer and the PDMS around the bond wire structure was cut down by razor blade, as shown in *figure 4.5 (d)*, and the sample was baked on hot plate at 160℃ for 2 min to let the thermal tape release the sensor part from the wafer, as shown in *figure 4.5 (e)*.

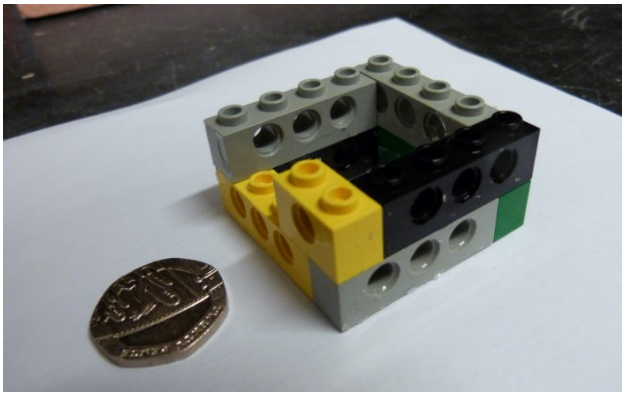

Figure 4.4 The LEGO bricks mould used for embedding process

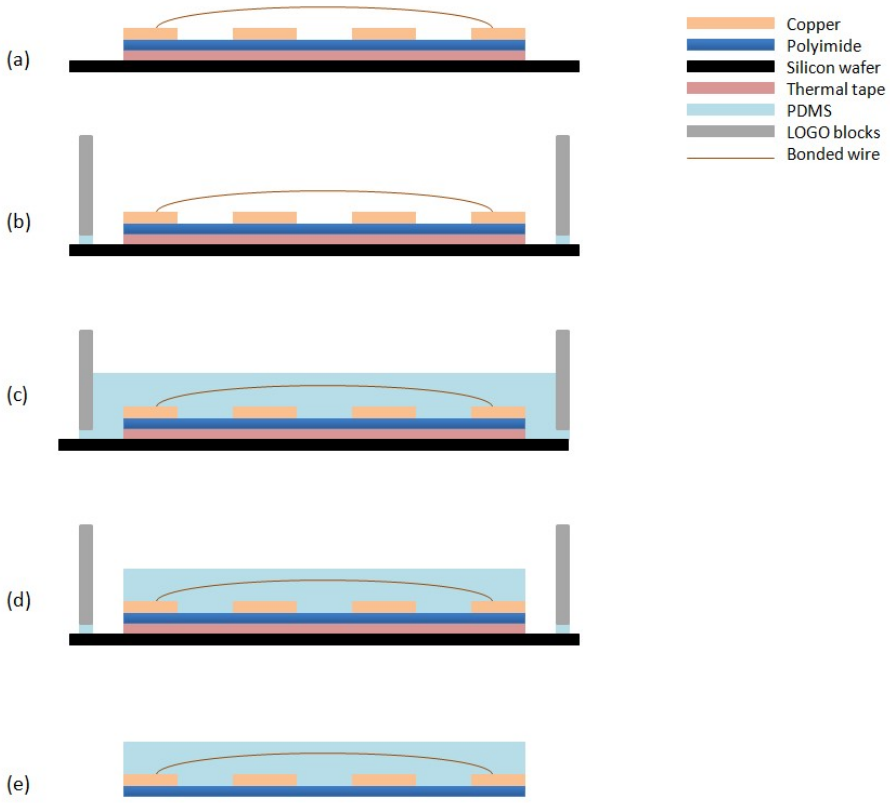

Figure 4.5 A schematic diagram of embedding process, in which (a) the copper pattern with wire bonded, (b) bonding the logo blocks on the silicon wafer by PDMS, (c) Injecting PDMS into the mould and curing for 24 hours, (d) cutting down the PDMS around sensor, (e) baking at 160 ℃ to release the sensor from the silicon wafer

4.3 Improvement and optimization on the original design and fabrication process

Even if a sensor was fabricated successfully by the process that introduced in the preceding section, there are still some potential problems in the wet etching and wire bonding process. Hence, some tests and analysis were made to improve and optimize the fabrication process, which will be presented as follows.

4.3.1 Analysis in wet etching process

Wet etching is a traditional manufacturing method in the PCB industry, the main advantages are that it is economical and easy to operate. However, in the fabrication process, the accuracy and stability were not as good as expected. The gaps between strips were designed to be 150 microns, and the width of the strips was designed to be 700 microns. While the actual gaps that were achieved by wet etching were around 200 to 250 microns and the strips were 700 to 750 microns. From *figure 4.3 (a)*, it also shows that the edges of those strips are rough.

The rough edges were probably caused by the coarse edges of the mask produced by the printer. If a finer mask employed, the edges will be very smooth and neat, as shown in *figure 4.6*.

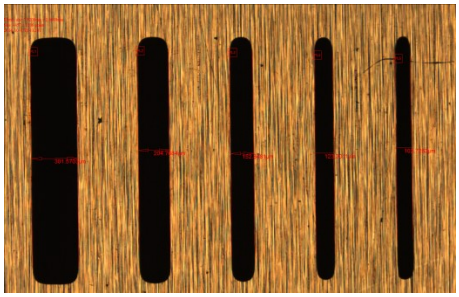

Figure 4.6 A tested copper pattern made by a fine mask

However, the accuracy of the wet etching, also known as etch factor, is influenced by multiple factors, such as the recipe of the etchant, temperature and duration of the etching process. The etch factor, which is describing the precision of the wet etching regarding to the etching depth, is defined as [8]:

$$Undercut, U = \frac{(W_f - W_i)}{2}$$

$$Etch\ factor = \frac{D}{U}$$

Where W_i is the designed width and W_f is the actual width after wet etching, D is the

etching depth, which is shown in *figure 4.7*.

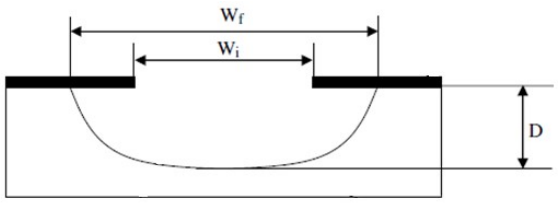

Figure 4.7 A schematic of the wet etching

However, in this case, all copper layers will be etched through, which means that etch factor will not be available for most of the situations in the etching process, so undercut will be the only factor in the tests below.

Etching tests on gaps in different widths were carried out in different conditions and the results were obtained in *table 4.1*. It has been proved that an etchant with 10 wt% hydrochloric acid, 10 wt% ferric chloride and 5 wt% nitric acid could obtain a very good etch factor and small under cut for stainless steel, which is 9.6 [8]. However, based on test 1, this etchant did not have a good result in etching copper. From the image and measurement taken by an infinite focus system called Alicona [9], which is shown in *figure 4.8*, most of the photoresist was 'washed off' and the most of area on the surface which was covered by the photoresist was attacked from sidewall by the etchant.

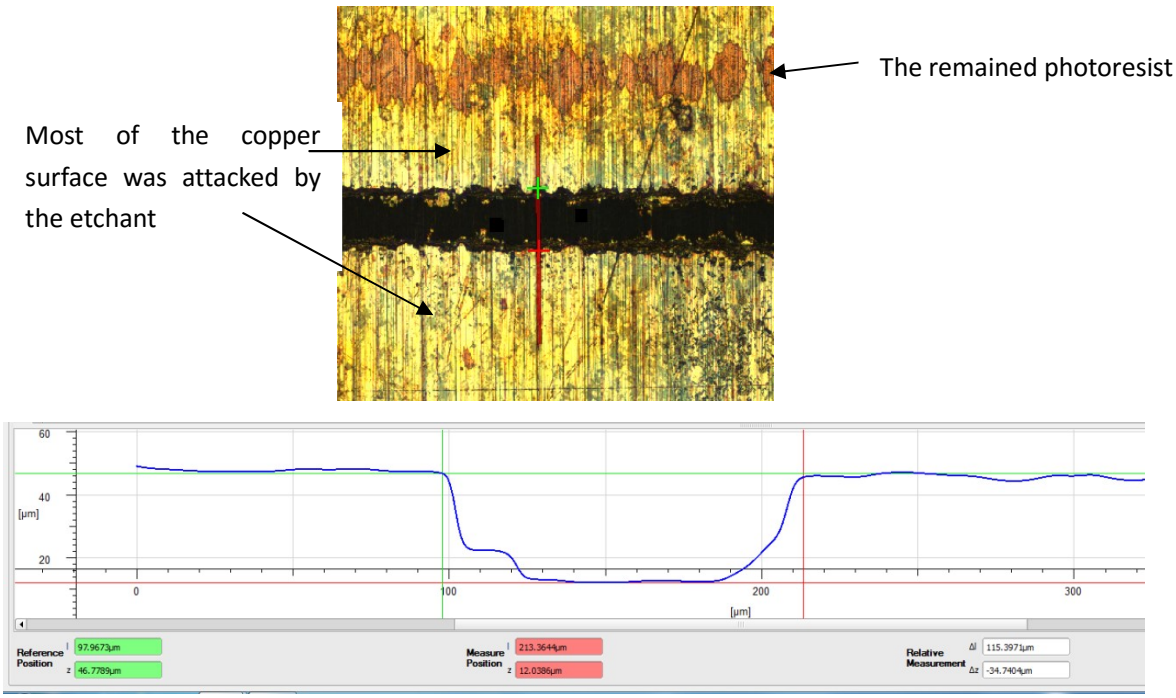

Figure 4.8 Image and measurement from Alicona for 25 micron gap etched by mix etchant (10 wt% hydrochloric acid, 10 wt% ferric chloride and 5 wt% nitric acid) at 40 ℃

From test 2, 3 and 4 in *table 4.1* increasing the temperature in the etching process for copper can increase the etch rate, but also decrease the slope of the sidewall and coarsen the surface of the copper, as shown *figure 4.9 (a), (b) and (c)*. It might be another reason for causing the unexpected result in test 1. From test 3 and 4, it is also found that controlling the etching duration can efficiently reduce the undercut, as the etching is ceased when the copper layer is etched through.

Table 4.1 Wet etching tests in different conditions

Test No.	Etchant	Temperature	Etching duration	Etch depth	Undercut
1	10 wt% hydrochloric acid, 10 wt% ferric chloride and 5 wt% nitric acid solution	40 ℃	25 min	35	45 μm
2	10 wt% ferric chloride solution	40 ℃	35 min	35	37.5 μm
3	10 wt% ferric chloride solution	20 ℃	90 min	35	42.5 μm
4	10 wt% ferric chloride solution	20 ℃	70 min	35	22.5 μm

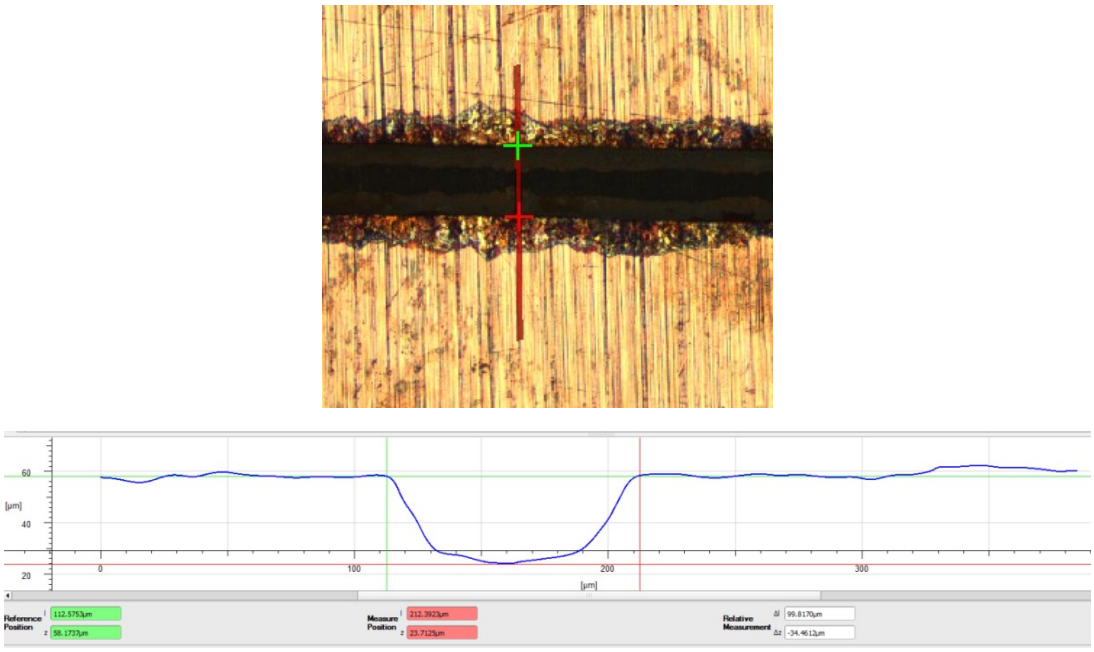

(*a*)

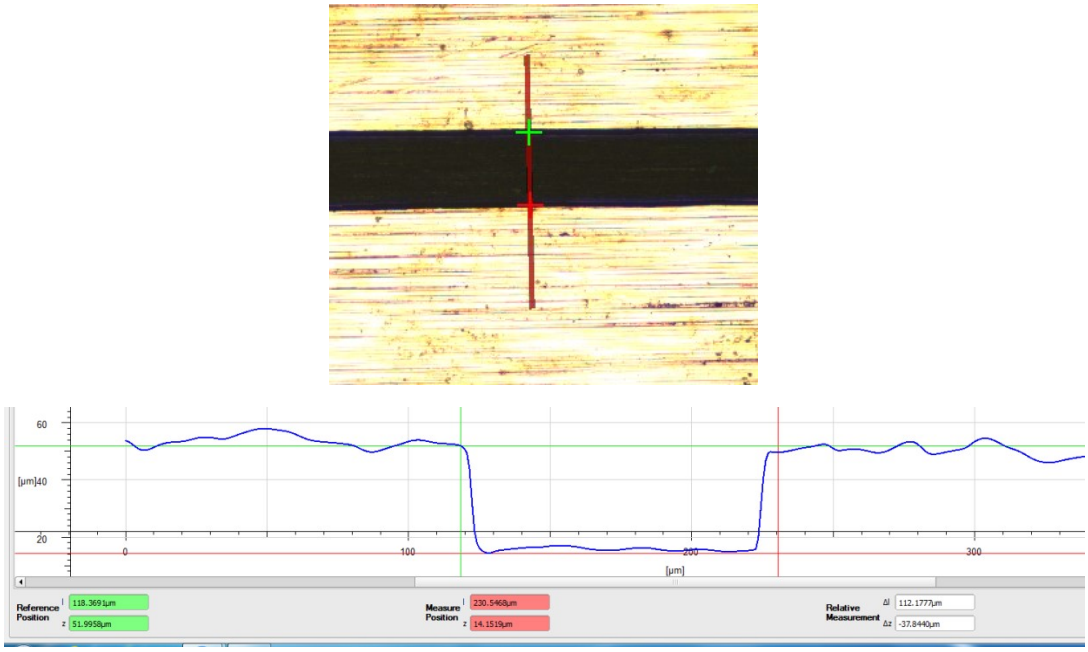

(*b*)

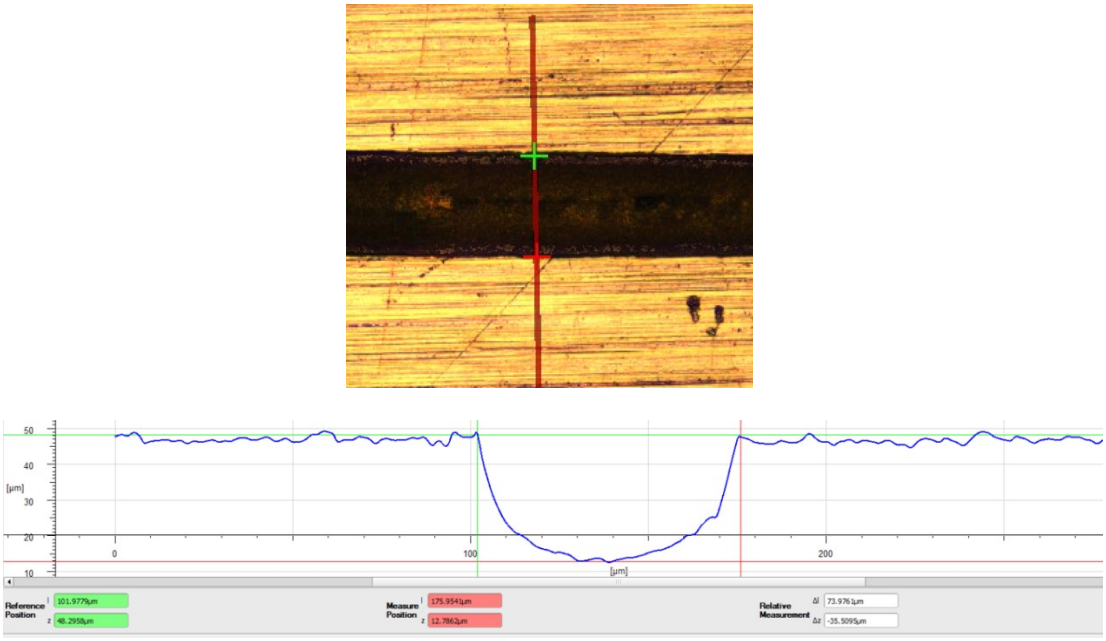

(*c*)

Figure 4.9 Image and measurement from Alicona for 25 micron gap etched at 40 ℃ for 35 min (a) and at room temperature 20 ℃ for 90 min (b) and 70 min (c) respectively

Additionally, from *figure 4.9 (c)*, it can be noticed that, for a 25 micron designed gap on 35

micron thick copper layer, the width of etched gaps was approximately 70 microns when the etched depth reached to 35 micron. So, it is believed that wet etching can hardly obtain a good result when features are 70 microns or less. Additionally, as isotropic process, if the etched feature is in different dimensions, the etch rates at different areas will be different and can be hardly controlled, which means for multiple etching gaps in different dimensions, in the same etching duration, some gaps are etched down while others are not. The etching duration, therefore, has to be increased to ensure every feature to be fully etched and this will inevitably result in narrowing the features in the patterns.

4.3.2 Potential problems and analysis in wire bonding

As introduced in section 2.2, the pattern was designed as four strips, and each of two strips would be connected as an electrode of the capacitor, which means two bonding steps were needed. However, during the second bonding step the wedge bonder will possiblly bend or misalign the wire array produced in the first bonding step. And this, inevitably, will influence the parallelism of the wire arrays. As shown in *figure 4.10,* some wires in the first bonding step are misaligned by the wires that bonded in the second step, some wires are even bended and touching each other.

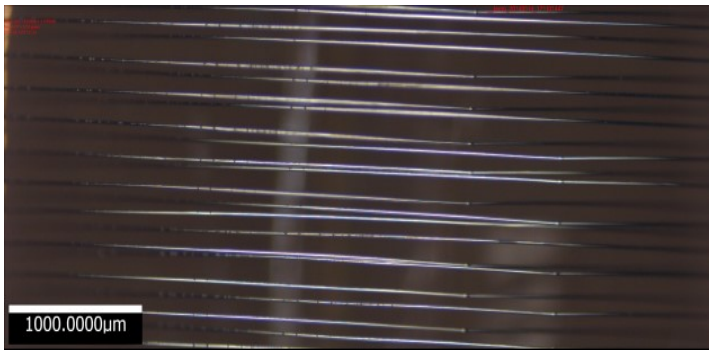

Figure 4.10 Wires are misaligned because of two bonding steps

A system of study was under taken of the bond length and height vs. wire parallelism. Based on results of the tests, which are shown in *table 4.2*, long bond length will not make any contribution to bonding quality but occasionally will result in problems on the parallelism of the wire array. These problems will undoubtedly have a negative effect and increase the instability, unreliability and ultimately yield in mass production. On the contrary, short bond length can achieve a highly parallel array with an appropriate bond height, but this also will decrease the capacitance of the sensor.

Table 4.2 The tests on the different combinations of bond length and height

Test No.	Spacing (μm)	Bond length (μm)	Bond height (μm)	Parallelism	Pictures
1	100	5000	330	Fair	-
2	100	5000	500	Fair	*Figure 4.11 (b)*
3	100	5000	700	Good	-
4	100	5000	900	Fair	-
5	100	5000	1200	Bad	*Figure 4.11 (c)*
6	100	3000	330	Good	
7	100	3000	500	Very good	
8	100	3000	700	Good	
9	100	3000	900	Fair	
10	100	3000	1200	Bad	
11	100	2500	330	Very good	-
12	100	2500	500	Very good	*Figure 4.11 (a)*
13	100	2500	700	Good	-

14	100	2500	900	Fair	-
15	100	2500	1200	Bad	-

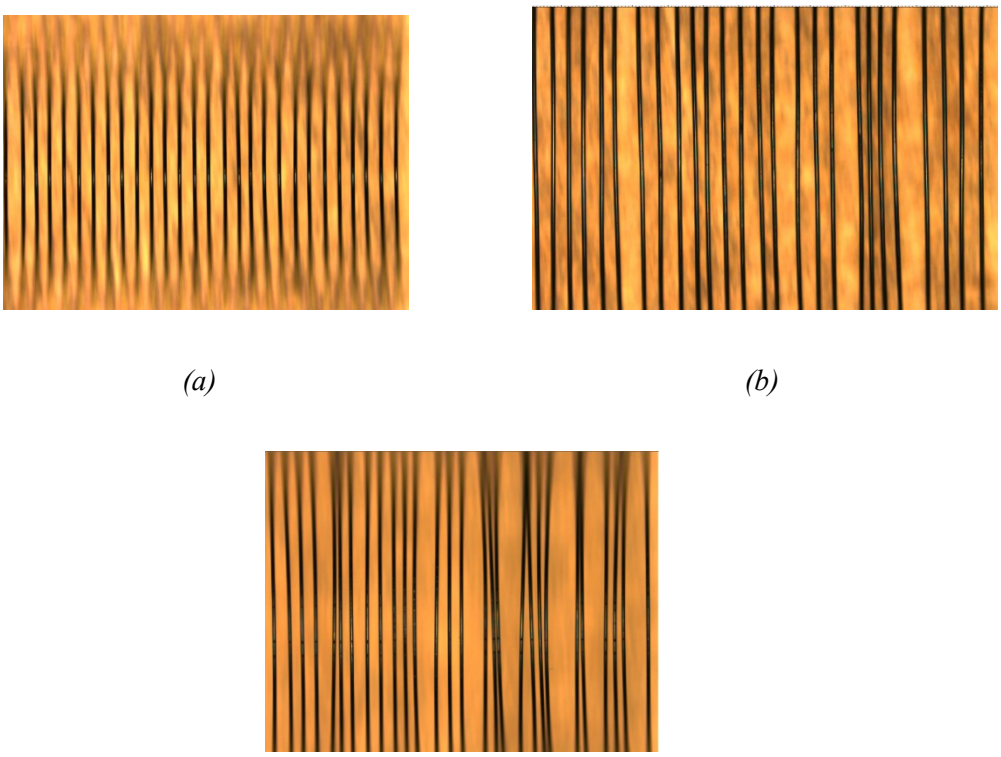

(a) *(b)*

(c)

Figure 4.11 Wire arrays at 2500 microns bond length and 500 micron bond height (a), at 5000 microns bond length and 500 micron bond height (b), at 5000 microns bond length and 1200 micron bond height (c)

From test 3, 6 and 7, it shows that the longer the bond length is, the higher the bond height must remain a good parallelism. As shown in test 1 to 5, it can be inferred that for a relatively long bonding, appropriately increasing the bond height can obtain a better parallelism. However, the parallelism also will be influenced if the bond height is too high, which is also shown from test 6 to 9. And from test 5 and 10 and shown in *figure 4.11 (c)*, it is found that when the bond height exceeding 1000 microns, the wire array will touch and interact with the

wedge bonder head, which results in bad parallelism of the array.

4.3.3 A re-designed copper pattern and an alternative method for producing copper pattern—laser machining process

In order to avoid the interaction between the two bonding steps, a re-designed copper pattern was carried out and shown in *figure 4.12*, strip 2 and 3 were replaced by small islands which were inserted between the fingers that connected to the strip 1 and 4. So these changes will generate a capacitor only through one wire array, and can avoid any misaligned effect of the wires in the array during bonding process. However, this design will also bring a challenge on the fabrication of the copper pattern: all the fingers and the islands have to be isolated with each other in terms of generating a capacitance.

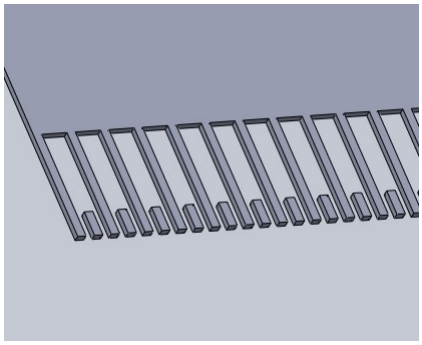

Figure 4.12 The re-designed pattern on the flexible PCB

Hence, considering the limitation of wet etching process, laser machining method was employed alternatively.

Laser machining has been employed as a micro-fabrication method in many applications such as MEMS, biomedical and surgery [10-13]. The technology generates either pulsed or continuous laser beam. During the interaction between beam and material, the power of the

laser beam is absorbed by the material, and a high temperature is developed in the beam spot, which results in the material softening, local yielding, melting, burning, or evaporation [13].

A LS4 from LASEA [14] was employed in the laser machining process. It was critical to find out the correct machining depth. On one hand, the gaps have to be deep enough to insulate the fingers. The machining depth, on the other hand, also has to be controlled to prevent the small islands from falling apart from the whole pattern in the process afterwards. Because of the material consumption in the laser machining process, 10 micron offset has to be added to the outline of the pattern design, so that the machining depth will be limited when the gaps are less than 20 microns. Additionally, a draft angle as shown in *figure 4.13*, which is mentioned in previous research papers [15, 16], is unavoidable in all laser millings. The actual machined gap will be wider than the designed gap if a specific depth is required. So, width of the gaps in the design has to be expanded to a reasonable value for isolating all the fingers with the islands.

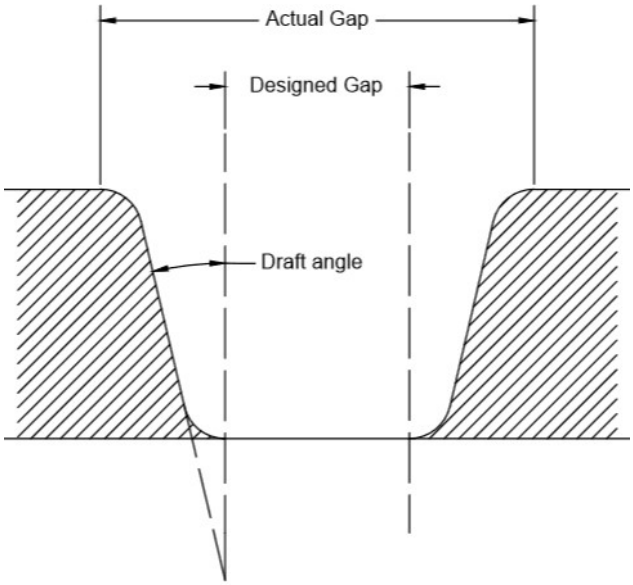

Figure 4.13 The draft angle that generated by the laser machining process

For all laser machining techniques, the craters in the final part are generated by layer-by-layer

machining [17]. As the machining depth can be controlled by the machining layers, some tests based on different machining layers were carried out, and the machining depths were measured by Alicona and the results are given by the *table 4.3*.

Table 4.3 The test results on different machining layers

Test No.	Number of machining layers	Machining depth (μm)	Electrical Isolation (Yes/No)
1	3	~20	No
2	5	~ 30	No
3	7	~ 35	No
4	8	60-70 (Somewhere are even 100 micron deep)	No

From the test 1 to 3, it can be inferred that approximately 6 micron deep copper is consumed by each machining layer. When seven layers were applied, the machining depth was approximately 35 micron, which was reaching the bottom of copper layer. From the machining depth in test 4, it can be known that the copper layer was fully machined and approximately 40 micron deep of polyimide layer was machined as well when eight layers were applied. However, the fingers and islands were still conductive. And this conduction probably was caused by the burned polyimide. Hence, it can be concluded that machining layers have to be controlled less than seven to avoid the laser reaching the polyimide layer and rest of the copper layer has to be finished and cleaned by a wet etching process.

4.4 Final design and fabrication process on the final design

Based on the improvements and optimization in the last section, the final design and the fabrication on this design are carried out, which aims at strengthen the stability and reliability of the process and avoid any potential problems when the process is employed in industry.

Firstly, laser machining and wet etching were combined in the fabrication of the copper pattern. So the fabrication of the pattern on the flexible PCB was slightly changed based on section 2.1. As it shown in *figure 4.14*, after coating with photoresist S1813, the flexible PCB was firstly laser machined with seven machining layers and then etched in 10% wt ferric chloride solution. During the etching process, ultrasonic vibration can accelerate the process; however, this will also cause the side wall area in the pattern to be attacked. The etching duration was 10 min to ensure gaps between the fingers and islands as well as the gaps in the middle landing islands being isolated.

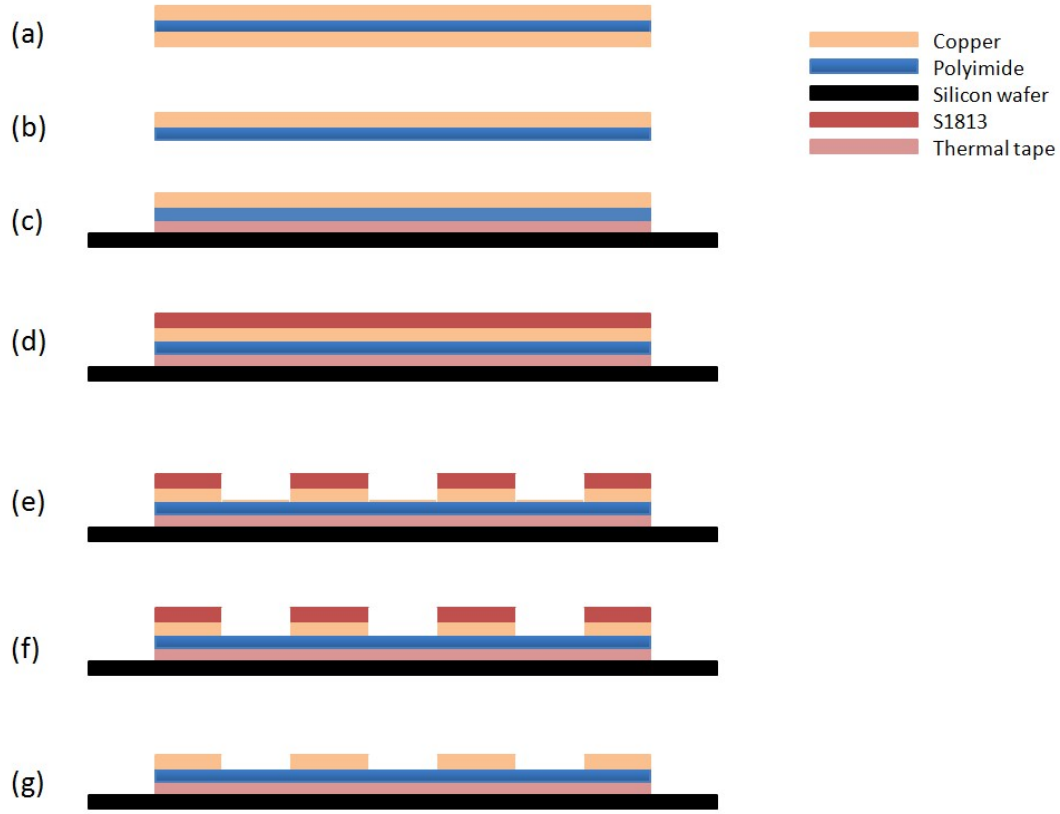

Figure 4.14 A schematic diagram of wet etching method, in which (a) the flexible PCB substrate, (b) etching down one side of the copper, (c) bond to silicon wafer, (d) coating a S1813 photoresist layer, (e) laser machining down most of copper layer, (f) cleaning off the rest of copper in the gaps, (g) cleaning the photoresist layer

Secondly, from the result in the wire bonding tests, the bond length in wire array was decided as 3mm while the height was set as 500 micron for the best parallelism. In order to complement the loss of capacitance due to the configuration, there are two same arrays employed and connected together. Therefore, an array of landing strips was added in the middle of the wire bonding area. For this design, although there are still two bonding steps, the arrays generated in these two steps are completely separated with each other and there will not be any interaction with each other. Compared with the original design, the height of wire array is halved. So, the injecting PDMS was also reduced to half of the original amount,

which was 0.29 mL.

Meanwhile, due to the material consumption in laser machining process and the side wall attacks in the wet etching process, all the gaps will be expanded and the finger will be narrowed down after laser machining and wet etching. So, all the gaps in the final design were 40 micron and the width of the finger was 100 micron, which guarantees that the fingers and islands are isolated with each other while fingers are wide enough for a wire bonding process. Therefore, the spacing in the wire array was increased to 140 micron. Additionally, as shown in *figure 4.15*, those two pads for connecting the external circuits were also replaced by two 5 mm wide pads which are connected to strip 1 and 4 by smooth curves, while width of the strips in the bonding area was 300 micron, which is aiming at minimizing the stiffness of the sensor. All the islands are connected out by two long pads for testing the isolation between the fingers and islands in the structure.

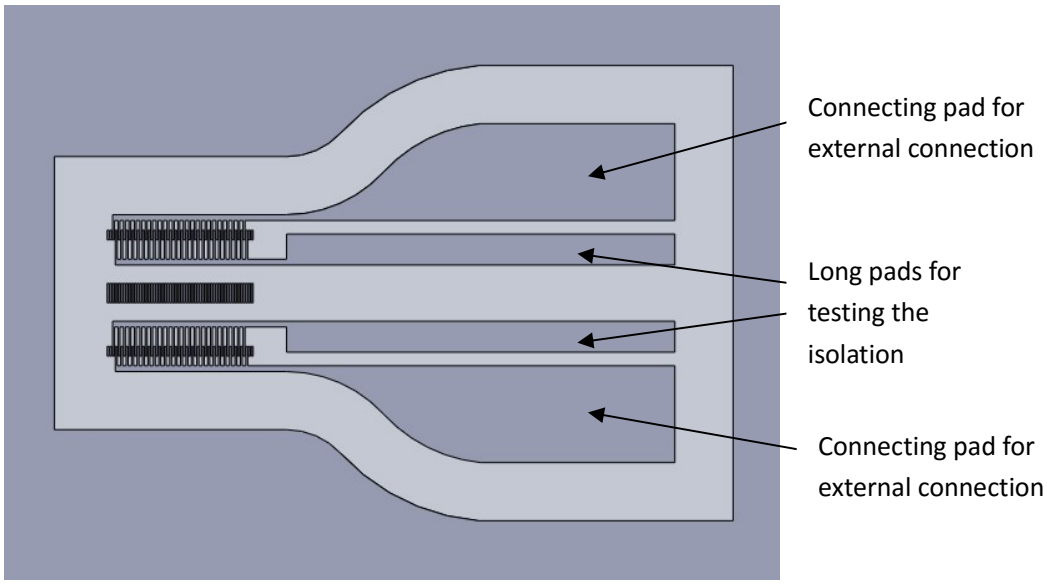

Figure 4.15 The drawing of the final bond wire capacitor design that drawn by Solidworks

Additionally, there are two more sacrificed landing islands designed at each end of the wire

bonding area, as shown in *figure 4.16*. The sacrificed islands will not contribute any capacitance to the design, but can keep the dimensions of the gaps and fingers in the structure consistent during a wet etching process, especially for the fingers and islands at two ends of the design. Moreover, the sacrificed islands can provide some testing areas for the wire bonding process as well.

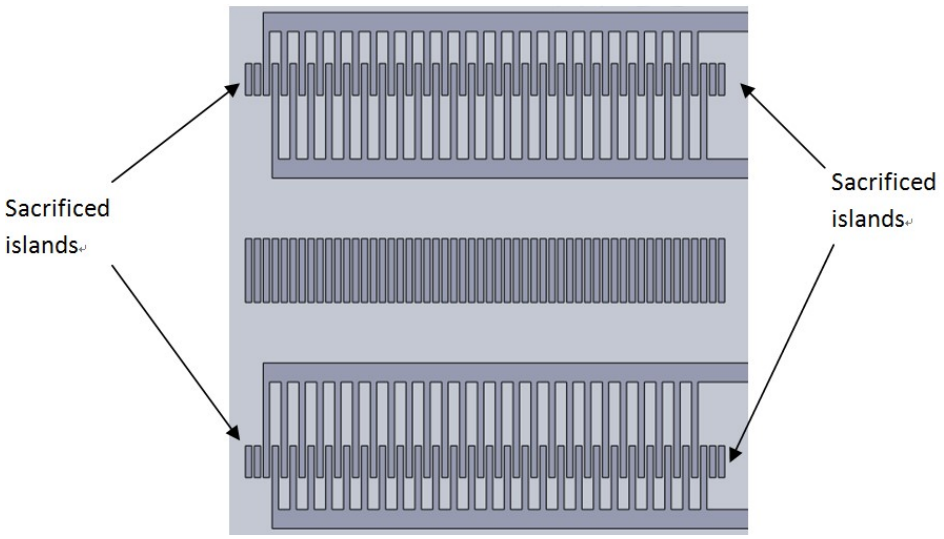

Figure 4.16 A detailed drawing in the wire bonding area

The *figure 4.17* shows the fabricated final bond wire capacitor design after being embedded in PDMS.

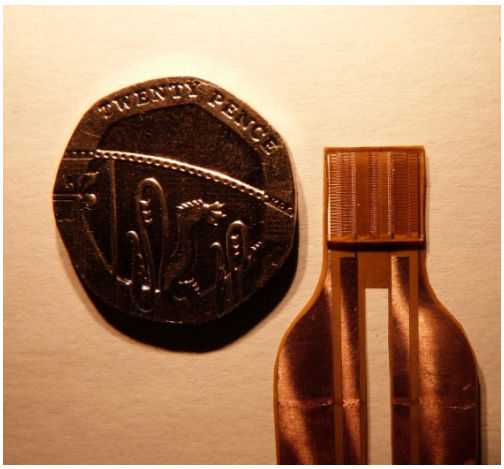

(a)

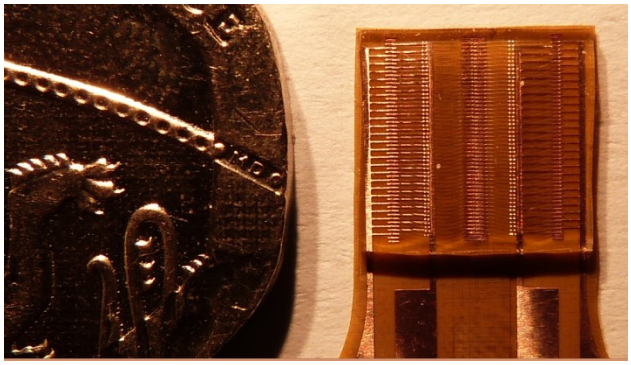

(b)

Figure 4.17 The fabricated final bond wire capacitor design compared with a 20 pence coin (a) and the zoomed in image (b)

4.5 Conclusions

This chapter presented the fabrication process on the bond wire capacitor design. Wet etching, wire bonding and PDMS embedding process was employed as the first attempting method to achieve the original design. However, it is difficult to generated parallel wire arrays in the original design due to the long bonding distance and it is also difficult to control the isotropic wet etching process in multiple etching gaps in different dimensions. So, for the stability, reliability and the possibility of introducing the process to a mass production, the original design was developed to a new design that sharing the same concept. In the fabrication of new design, the bonding distance and bond height were both reduced to reasonable values to ensure the parallelism of wire arrays and laser machining process was combined with the wet etching process to achieve isolated fingers and islands in an condensed area. The fabricated sensor was also shown in *figure 4.17*. In the next chapter, adhesion methods for the sensor and tyre rubber will be investigated and the sensor will be calibrated and measured by different methods.

Reference

1. Lum, I., M. Mayer, and Y. Zhou, *Footprint study of ultrasonic wedge-bonding with aluminum wire on copper substrate.* Journal of Electronic Materials, 2006. **35**(3): p. 433-442.
2. Harman, G.G., *Wire bonding in microelectronics : materials, processes, reliability, and yield*. 2nd ed. Electronic packaging and interconnection series. 1997, New York: McGraw-Hill. xiv, 290 p.
3. *DuPont™ Pyralux® AP, Technical Data Sheet*. p. 1.
4. Branson, J., J. Naber, and G. Edelen, *A simplistic printed circuit board fabrication process for course projects.* Education, IEEE Transactions on, 2000. **43**(3): p. 257-261.
5. Park, J.M., L.J. Matienzo, and D.F. Spencer, *Adhesion and XPS studies on a fluoropolymer-metal interface.* Journal of Adhesion Science and Technology, 1991. **5**(2): p. 153-163.
6. Adaikkalam, P., G.N. Srinivasan, and K.V. Venkateswaran, *The electrochemical recycling of printed-wiring-board etchants.* JOM, 2002. **54**(6): p. 48-50.
7. *HP Color LaserJet CP2025 Printer series*. 29/07/2014]; Available from: http://h10010.www1.hp.com/wwpc/uk/en/sm/WF10a/18972-18972-3328060-236268-236268-3673580.html.
8. Rao, P.N. and D. Kunzru, *Fabrication of microchannels on stainless steel by wet chemical etching.* Journal of Micromechanics and Microengineering, 2007. **17**(12): p. N99-N106.

9. *InfiniteFocus Alicona*. Available from: http://www.alicona.co.uk/home/products/infinitefocus.html.

10. Farson, D.F., et al., *Femtosecond laser micromachining of dielectric materials for biomedical applications.* Journal of Micromechanics and Microengineering, 2008. **18**(3).

11. Zheng, H.Y. and Z.W. Jiang, *Femtosecond laser micromachining of silicon with an external electric field.* Journal of Micromechanics and Microengineering, 2010. **20**(1): p. 017001.

12. Amer, M.S., et al., *Femtosecond versus nanosecond laser machining: comparison of induced stresses and structural changes in silicon wafers.* Applied Surface Science, 2005. **242**(1–2): p. 162-167.

13. Chryssolouris, G., N. Anifantis, and S. Karagiannis, *Laser Assisted Machining: An Overview.* Journal of Manufacturing Science and Engineering, 1997. **119**(4B): p. 766-769.

14. *LS4 A compact precision micromachining machine*. Available from: http://www.lasea.eu/en/machines/ls4-2/.

15. Heyl, P., T. Olschewski, and R.W. Wijnaendts, *Manufacturing of 3D structures for micro-tools using laser ablation.* Microelectronic Engineering, 2001. **57-8**: p. 775-780.

16. Pham, D.T., et al., *Laser milling as a 'rapid' micromanufacturing process.* Proceedings of the Institution of Mechanical Engineers Part B-Journal of Engineering Manufacture, 2004. **218**(1): p. 1-7.

17. Pham, D.T., et al., *Laser milling.* Proceedings of the Institution of Mechanical Engineers Part B-Journal of Engineering Manufacture, 2002. **216**(5): p. 657-667.

Chapter Five.
Experiments and Calibration of the Strain Sensor

5.1 Introduction

The fabrication process of the bond wire strain sensor was introduced in the last chapter. To investigate the changes of the capacitance in different strain conditions, experiments on the strain sensor will be carried out, discussed and analyzed in this chapter.

In order to transfer the strain behaviour of sensing area in the tyre to the sensor without any influence, an adhesive bonding method will be developed first. Vulcanization fluid, PDMS and silicone adhesive with/without primers will be tested for attaching the sensor on a tyre rubber sample. Among them, vulcanization fluid is a commercial adhesive in the tyre rubber industry, which is also used for tyre repairing while PDMS is considered as an effective adhesive for bonding PDMS materials [1-3]. The theory and the bonding process for each adhesive bonding method will be also presented and discussed. Manual peeling tests will be given to each adhesive bonding method and the silicone adhesive from Smooth-on with the primer NO 3 from ACC-silicone is determined as the final adhesive bonding method.

Following on from the adhesive bonding methods, there will be three calibration methods introduced for the strain sensor: the tensile test, the bending test and the cantilever test. The equipments employed in each test will be explained. Theory about the bending test and the cantilever test will also be presented in details. The results of each testing method will be

illustrated in tables and figures. Discussions and analyses on the measurements will be given and the deficiencies in each calibration method will be discussed as well. Thanks to the stability and reliability, the cantilever test was determined as the best calibration method for the strain sensor, the relationship between the capacitance and the strain is nearly linear, which meets the results from the calculation and simulation in Section 3.3.3. The changing rate is approximately 0.090 pF per 10000 micro-strain.

5.2 The investigation on adhesive bonding method

Since the sensor is measuring the strain of the tread part of a tyre, the adhesion between the tread and sensor is vital. The adhesive layer not only has to be thin enough compared with the thickness of the senor in case of any stress/strain absorption from the sensing area, but also has the similar elasticity as (or more elasticity than that of) the sensor and the tyre rubber to prevent any effects and disturbance when the sensing area is strained. Hence, in this section, several adhesives methods will be introduced and tested for bonding tyre rubber and PDMS surfaces , which are vulcanization fluid, PDMS and silicone adhesive with special primers.

5.2.1 Vulcanization fluid

For the material of the tyre, the main components consist of natural rubber (NR), styrene-butadiene rubber (SBR) or poly-butadiene rubber (BR), and also compounded with carbon black and chemicals for a better hardness, strength and abrasion performance [4]. While NR, SBR and BR are all polymer material, the chemical structures are shown in *figure 5.1*.

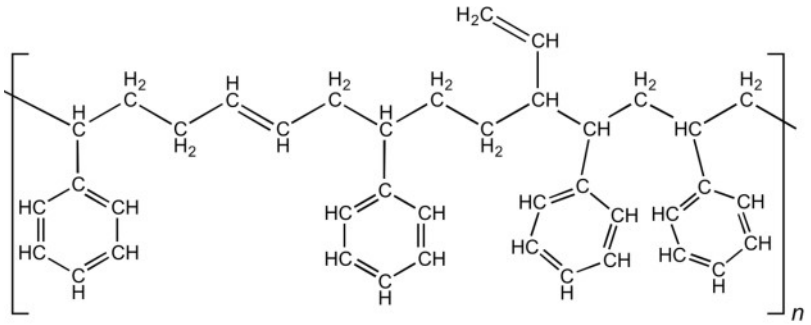

(a)

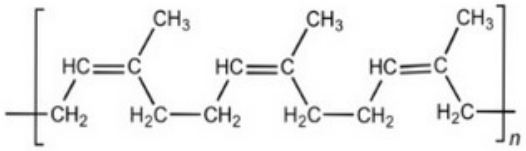

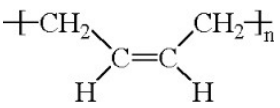

(b) (c)

Figure 5.1 Chemical structure of styrene-butadiene rubber (a) [5], natural rubber (b) [6], poly-butadiene rubber (c) [7]

For polymer material, vulcanization is one of the most effective methods for bonding two individual chains together [8, 9]. Normally it can produce junctures by inserting a sulphur atom (-S-), a group of sulphur atoms ($-S_n-$), a carbon to carbon bond (C-C) or a polyvalent organic radical to generate cross-links between two polymer chains [9]. Hence, vulcanization was determined for the adhesive bonding method between the tread and the sensor as the first attempt.

Vulcanizing fluid from REMA TIP TOP [10] was selected as the bonding material. As mentioned in Section 3.3.1, it was employed as the adhesion for interdigital capacitor design.

Firstly, both of the bonding surfaces were cleaned by isopropanol alcohol (IPA).[5] The surface of the tyre rubber was then granulated by the sand paper for more contacting area with the vulcanizing fluid. After the vulcanizing fluid applied on the granulated surface of the tyre rubber, the PDMS sample was pressed on the bonding area and kept pressed under a constant force of 200 g over night.

Although the vulcanizing fluid works well between surfaces of tyre rubber, it could not achieve a strong bond between surfaces of PDMS and tyre rubber and the PDMS sample could be peeled off manually from the tyre surface. Moreover, as shown in *figure 5.2 (a)* and *(b)*, it was found that the vulcanizing fluid could also bend the PDMS surface, which might generate some interior stresses in the sensor and results of inaccuracies of the measurement.

(a) *(b)*

Figure 5.2 The PDMS sample before applying the vulcanizing fluid (a) and after applying the vulcanizing fluid (b)

5.2.2 Polydimethylsiloxane (PDMS)

As the vulcanising fluid may result of some bending effects on the surface of the PDMS, it

[5] Acetone is usually employed as the cleaning solvent, however it was found that acetone can dissolve the tyre rubber. Hence, IPA was employed as an alternative cleaning solvent.

can be inferred that the adhesive material has to be friendly to both of the bonding surfaces. Hence, as a low chemical activity material, PDMS was tested as a potential adhesive. In fact, PDMS is also employed as an adhesive in some micro-fluidics research [1-3], and it is a good bonding material between surfaces of PDMS-PDMS, PDMS-glass and silicon-silicon wafer. Different from vulcanization, PDMS will neither change the chemical structure of the bonding surface nor create chemical bonds between them. So the bonding generated by PDMS is physical, rather than chemical.

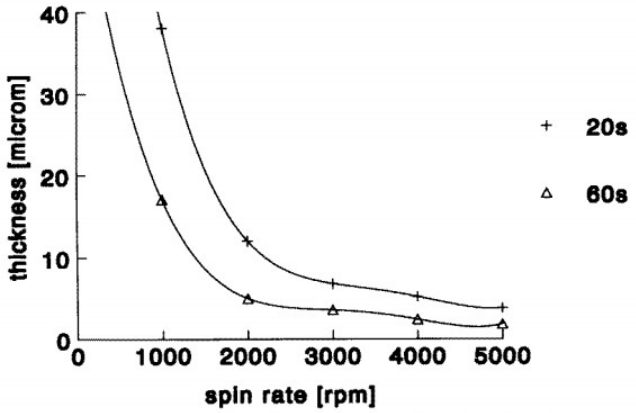

Figure 5.3 The thickness of PDMS at different spinning speeds and spinning durations [11]

When employing PDMS for bonding two surfaces in micro-fluidics, a PDMS adhesive layer with known thickness is generated by spinning PDMS on a transfer wafer at a specific speed. The thickness of PDMS at different spinning speeds and spinning durations is shown in *figure 5.3*. One of the bonding surface is brought into contact with the adhesive layer, then the surface with transferred PDMS is attached to the other bonding surface. After curing the PDMS into solid, a firm connection between these two surfaces will be created.

The two bonding surfaces were cleaned by IPA firstly. A PDMS adhesive layer was spun on a wafer at 3000 rpm for 60s. Then the PDMS sample was brought into contact with the

adhesive layer and attached to the tyre sample. After that, the two bonding pieces were placed on the hot plate at 60℃ for 20 min and then left at room temperature over night. However, there was no actual bonding between the tyre and PDMS surfaces. The PDMS sample could be easily peeled off manually from the tyre sample.

5.2.3 Primer method

From the two adhesive bonding methods tested in the last two sections, it can be noticed that the normal adhesive bonding methods for tyre rubber and PDMS are not suitable for bonding tyre and PDMS surfaces together and there are huge differences in chemical properties for the tyre rubber and PDMS. It is difficult to generate a strong chemical or physical bond between these two surfaces. Therefore, a primer is needed to adapt one of surface to have a similar property with the other one. Since silicone adhesive not only has similar properties with PDMS but also can provide a strong and flexible bond, primer for silicone adhesive was determined as the testing target.

Hence, there were two primer products from ACC-silicones selected as the test primers for the tyre rubber, which are primer NO 3 and primer OP2N-1. Primer NO3 is silicone based while primer OP2N-1 is a silicone resin based and both of them are for use with silicone adhesive. Meanwhile, Sil-Poxy® silicone adhesive from Smoot-on was selected as the bonding material.

There were three tests carried out, as shown in *table 5.1*, all of them were employing

Sil-Poxy® silicone adhesive as the bonding material and test 1 was applying with primer NO 3, test 2 was applying with primer OP2N-1 while the test 3 was only applying without any primer. For the test 1, after cleaning the bonding surfaces with IPA, the primer NO 3 was applied on either both of the bonding surfaces or only the surface of tyre rubber sample by a brush and left for curing in the fume cabinet for 45 min. After that, the silicone adhesive was applied on the tyre rubber sample and then the PDMS piece was placed on the bonding area and pressed by flat-end tweezers to move away the extra adhesive between bonding surfaces. Then these two bonding pieces were left in the fume cabinet for 2 hours at room temperature for fully curing the adhesive. For test 2 and 3, the process for bonding the tyre rubber and PDMS pieces was basically the same as test 1, but the curing duration of primer OP2N-1 was 30 min in test 2[6] and there was no primer applying in test 3.

[6] The curing durations for primer NO3 and primer OP2N-1 was following the instructions in the data sheets from ACC silicone

Table 5.1 The bonding test on different primer situations with silicone adhesive

Test No.	Primer	Adhesive	Applying surfaces	Manual peel test
1	Primer NO 3	Sil-Poxy silicone adhesive	On both bonding surfaces	Passed
			Only on the surface of tyre rubber sample	Passed
2	Primer OP2N-1	Sil-Poxy silicone adhesive	On both bonding surfaces	Not passed
			Only on the surface of tyre rubber sample	Not Passed
3	No Primer	Sil-Poxy silicone adhesive	N/A	Not passed

The results for these three tests were also given in *table 5.1*, the bonding with primer NO 3 had the best bonding strength. Although in test 2 and 3, the bonding was strong, PDMS pieces still could be peeled off manually from tyre rubber piece. In test 1, PDMS piece could not be peeled off even if the PDMS piece was broken. However, it was also found that similar with vulcanizing fluid, the primers could also bend PDMS samples so applying primers on the PDMS samples did not help building a stronger bonding while might weaken the bonding. So the primer NO 3 is selected as the primer and it will only be applied on tyre rubber surface to obtain the best bonding strength.

5.2.4 The summary of adhesive bonding methods

In the previous sections, vulcanizing fluid, PDMS and silicone adhesive with primers were tested for bonding tyre rubber and PDMS surfaces. As commercial adhesive bonding method

for tyre rubber and traditional adhesive bonding method for PDMS, vulcanizing fluid and PDMS cannot achieve a strong bond between the tyre rubber and PDMS. The silicone adhesive from Smooth-on with primer NO 3 from ACC-silicones had the best bond strength and the bonding was even stronger than the PDMS sample itself. What has to be mentioned is, only applying the primer on the tyre rubber surface can bring a stronger bond than applying on both bonding surfaces. Meanwhile, the bonding is flexible and will not influence any strain behaviour of either the sensor or the tyre. Hence, this adhesive bonding method was employed between tyre and sensor surfaces.

5.3 Measurements and calibration of the strain sensor

In this section, the strain sensor will be measured and calibrated in tensile test, bending test and cantilever test. In each test, the capacitance of the sensor with respect to the strain will be presented and discussion and analysis will be given as well. Since the adhesive bonding method that is employed for attaching the sensor on the tyre rubber substrate is irreversible, the strain sensors can only be used once. Hence, each test method uses a new sensor sample, so the initial capacitance in these three methods are different from each other due to the manufacturing tolerance.

5.3.1 Tensile test

To measure the capacitance variations with respect to strain, the strain has to be known when the sensing area is stretched or compressed. Therefore, a tensile test on a tyre rubber sample with known dimensions, which is the most direct method, was carried out.

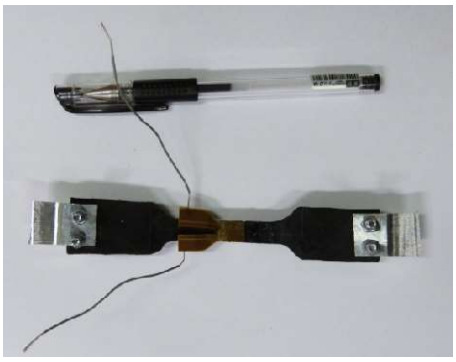

Figure 5.4 The bond shaped tyre rubber sample with the strain sensor bonded on and two aluminium clampers at two ends

Different from metallic material that usually tested in the tensile machine, tyre rubber is a flexible material, it has a relaxation effect in a compression or stretch condition, which means that when the tyre rubber is stretched, the material will relax by itself even when the two ends are clamped. Meanwhile, areas at two ends of the tyre rubber sample that are clamped on the machine will be compressed and deformed, which make these areas easier to rupture during the tensile test. Hence, the tyre rubber sample was cut into a bone-shape to strengthen the two ends, as shown in *figure 5.4*. Two aluminium clampers were also machined for clamping both ends of the sample for minimizing the self relaxing effect of the sample. For one side of the clamper, there were two M4 thread holes for bolting and fixing on the end of the sample while for the other side of the clamper, a boss was made for being fixed by the tensile machine.

(a)

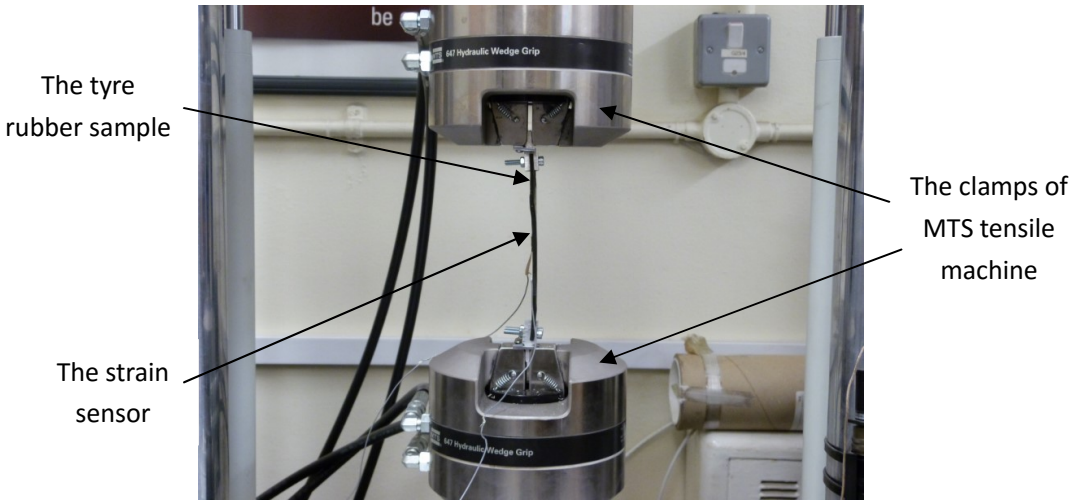

(b)

Figure 5.5 The tensile test for the strain sensor under the MTS tensile machine (a) and a close view of tyre rubber sample in the machine (b)

After applying primer NO3 on the surface of the bone shaped sample, the sensor was bonded on at the middle of the sample by the silicone adhesive. Then the sample was clamped on the MTS tensile machine, as shown in *figure 5.5 (a)* and *(b)*. The distance between the two fixed ends was 12 cm in original. And the sensor was connected out to WAYNE KERR Precision Component analyser 6425 by two wires that soldered on the connecting pads of the sensor. The analyser can measure the capacitance directly, so the variation of capacitance of the

sensor can be measured if the sample is under a specific strain which can be calculated with the displacements between the clamps on the tensile machine. The frequency of the analyser was set up as 5 kHz and 1 volt alternating voltage was applied on a 2 volt direct voltage.

The results of the tensile test are given in *table 5.2* and *figure 5.6 (a)* and *(b)*.

Table 5.2 The results of the tensile test for the strain sensor

		Capacitance (pF)						
Displace-ment (mm)	**Strain**	**Test 1**	**Test 2**	**Test 3**	**Test 4**	**Test 5**	**Average**	**Standard deviation**
0	0	10.8580	10.6500	10.7415	10.6500	10.6515	10.7102	0.0819
1	0.0083(0.83%)	10.8535	10.7400	10.7200	10.6400	10.7120	10.7331	0.0690
2	0.0167(1.67%)	10.8495	10.7280	10.8575	10.6140	10.6910	10.7480	0.0937
3	0.0250(2.50%)	10.8395	10.6540	10.6700	10.5975	10.6040	10.6730	0.0878
4	0.0333(3.33%)	10.8340	10.5840	10.6380	10.5800	10.5900	10.6452	0.0967
5	0.0417(4.17%)	10.6280	10.5695	10.5795	10.5735	10.5735	10.5848	0.0218
6	0.0500(5.00%)	10.5580	10.5515	10.5600	10.5600	10.5595	10.5578	0.0032
7	0.0583(5.83%)	10.5380	10.5375	10.5440	10.5375	10.5475	10.5409	0.0041
8	0.0667(6.67%)	10.5235	10.5220	10.5320	10.5340	10.5415	10.5306	0.0072
9	0.0750(7.50%)	10.5120	10.5195	10.5295	10.5300	10.5360	10.5254	0.0085
10	0.0833(8.33%)	10.5040	10.5100	10.5240	10.5235	10.5195	10.5162	0.0079

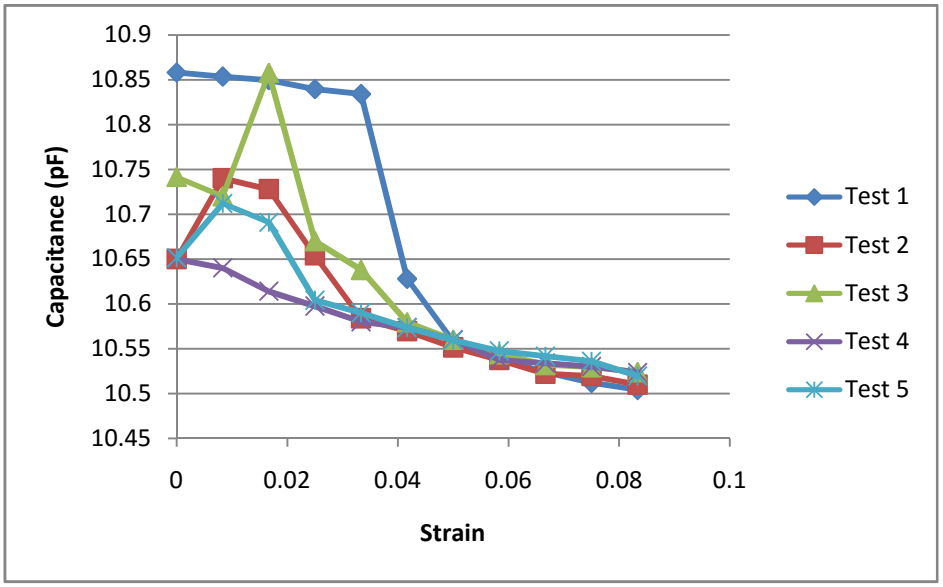

(a)

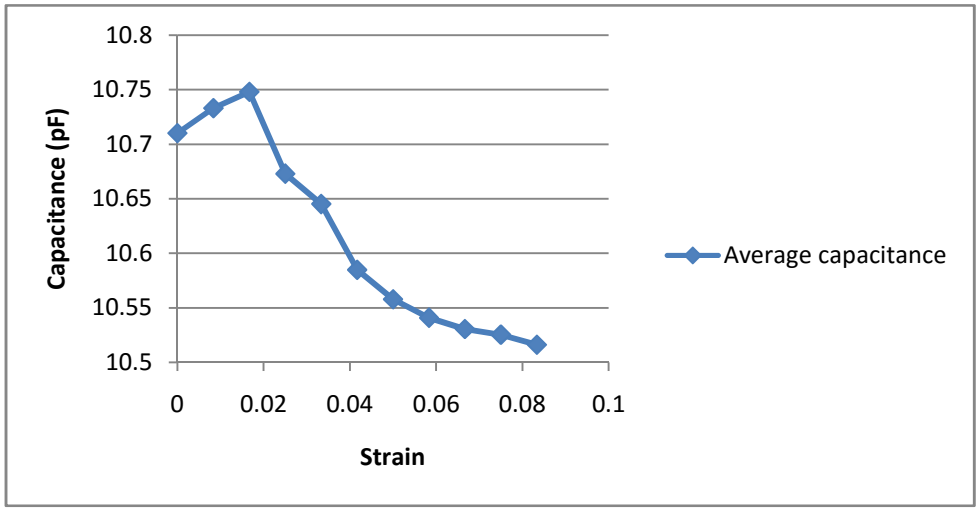

(b)

Figure 5.6 The diagram for the values of capacitance of the strain sensor in each tensile test (a) and in average (b)

From *table 5.2* and *figure 5.6 (a)*, it can be seen that when the displacements are smaller than 5mm, the capacitance does not have a clear relationship with the strain (which should have been in a linear-like relationship from the simulation and calculation). It also can be noted that the standard deviations at the displacements from 0 to 5mm are almost thirty times than that at the displacements from 6 to 10mm. However, when the displacements were larger than

5mm, the capacitance in all of five tests were going in the same trend and more linear. Hence, values of capacitance after this point are more reliable to evaluate the sensor. Also from *table 5.2*, the average capacitances for five tests at strain of 0.05 and 0.083 strain are 10.5575 pF and 10.5155 pF respectively. So, the capacitance decreased by 0.042 pF when the strain increased by 0.033 (which is 33000 micro-strain), which is 0.0127 pF per 10000 micro-strain. Compared with the results from calculation and simulation in Section 3.3.3.2, the changing rate from the tests is smaller, the capacitance decreased 0.036 pF and 0.018 pF per 10000 micro-strain, respectively.

Even if two aluminium clamps were using for both ends of the sample, the self relaxing of the tyre rubber in the tensile test still is the main problem for the measuring process. It is also the main reason for the smaller changing rate compared with the results in the theory and simulation. The self relaxing of the sample could be also noticed during measurements, capacitance dropped instantly and grew back to a stable value when the sample was applied with a quick change in displacement. Additionally, it was difficult to determine the initial point at the beginning of tests. In these five tests, the capacitances at 'zero strain' had significant differences with each other, the largest difference was 0.35 pF from test 1 and test 2, it also can be reflected by the measurements in the beginning of displacements in each test. There were some dramatic decreases in test 1, test 2 and test 3 and even some unexpected increases in test 2, test 3 and test 5. So it can be concluded that the tensile test cannot obtain meaningful and stable results when the strain is less than 5% and even when the strain is higher than 5%, there is no accurate measurements can be taken due to the self-relaxing

effects. However, from the literature review, the measurement range for the strain sensor is about -10000 micro-strain to 20000 micro-strain (-1% to 2%), which has to be the measuring range for calibrating the strain sensor. Therefore, the tensile test does not satisfy the requirements of sensor calibration.

5.3.2 Bending test on a rod with various diameters

As the tyre rubber sample in the tensile test have self relaxing, it is difficult to obtain the actual capacitance at every strain condition. A bending test on a rod with various diameters was carried out for the strain sensor. A stretching condition was achieved by firmly attaching the polyimide side of the sensor to the surface of the rod in the direction that is vertical to the axial direction of the rod, which is shown in *figure 5.7* (the axial direction of the rod is vertical to the paper). Due to the curved surface of the rod, the top surface of the sensor will be stretched. From the radius of the rod and the thickness of the sensor, the stretched strain can be calculated.

In the *figure 5.7*, it can be obtained that:

$$\frac{l_w}{l_w + \Delta l_w} = \frac{R_r}{R_r + h} \qquad Eq\ 5.1$$

where l_w is the length of the strain sensor, Δl_w is the length increase because of bending on the rod, R_r is the radius of the rod and h is the height of the sensor. When the sensor is in a flat condition, the length of polyimide side and PDMS side are both l_w , when the sensor is in a bended condition, the PDMS side is stretched for Δl_w. While the strain $\varepsilon_{\text{bend}}$ can be given by:

$$\varepsilon_{bend} = \frac{\Delta l_w}{l_w} \qquad Eq\ 5.2$$

Hence, the equation $Eq\ 5.1$ can be transferred to:

$$\frac{1}{1+\frac{\Delta l_w}{l_w}} = \frac{1}{1+\varepsilon_{bend}} = \frac{1}{1+\frac{h}{R_r}} \qquad Eq\ 5.3$$

So,

$$\varepsilon_{bend} = \frac{h}{R_r} = \frac{2h}{D_r} \qquad Eq\ 5.4$$

where D_r is the diameter of the rod

Therefore, the strain is only related to the height of the sensor and the radius of the rod. From the fabrication process in Chapter 4 and the datasheet of the flexible PCB, the height of the sensor can be calculated, which is 0.5858 mm.

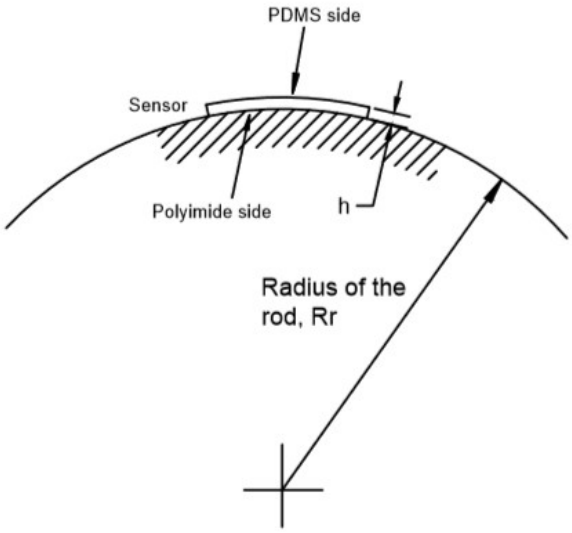

Figure 5.7 A schematic diagram for the bending test with a rod

As shown in *figure 5.8*, an aluminium rod with various diameters was machined to acquire different strain conditions. The WAYNE KERR analyser was also employed for measuring the capacitance and the set up remained the same as that in the tensile test. The polyimide side of the sensor was bonded on a long polyimide tape, when the two ends of the tape was pulled with force manually, the polyimide side of the sensor was firmly attached and by wrapping on

the surface of the rod. Hence, a variation of the capacitances can be obtained by wrapped the sensor on the rod with different diameters, which is given by *table 5.3*. What has to be mentioned is, when the sensor was wrapped on the rod with diameter that smaller than 17.91 mm, the PDMS was starting to be peeled off from the polyimide substrate, which is a situation that would not occur for the sensor in use bonded to tyre. Hence, any larger strain that is over 6.54% was not recorded in the table. Additionally, five tests were conducted to check the repeatabilty of the meansurement.

Figure 5.8 The machined aluminium rod with various diameters that was used in the bending test

Table 5.3 The results of the bending test for the strain sensor

		Capacitance (pF)						
Diameter of the rod, D_r (mm)	**Strain**	**Test 1**	**Test 2**	**Test 3**	**Test 4**	**Test 5**	**Average**	**Standard Deviation**
N/A	0	11.7530	11.7280	11.7360	11.7385	11.7400	11.7391	0.0081
49.76	0.0235(2.35%)	11.2120	11.2165	11.1230	10.9375	10.9550	11.0888	0.1212
39.78	0.0295(2.95%)	11.1215	11.1200	11.0570	10.8365	10.9110	11.0092	0.1154
33.02	0.0355(3.55%)	10.9000	10.9635	10.9165	10.7245	10.7480	10.8505	0.0959

28.36	0.0413(4.13%)	10.5420	10.9070	10.8875	10.6210	10.6545	10.7224	0.1475
24.69	0.0475(4.75%)	10.8170	10.615	10.6640	10.5245	10.5970	10.6435	0.0976
21.88	0.0535(5.35%)	10.6190	10.5655	10.6165	10.4235	10.3970	10.5243	0.0954
19.7	0.0595(5.95%)	10.5855	10.4800	10.5830	10.4085	10.5310	10.5176	0.0669
17.91	0.0654(6.54%)	10.5090	10.4380	10.5385	10.3990	10.5040	10.4777	0.0513

Figure 5.9 is also illustrated based on the results in *table 5.3*.

It can be seen from the *figure 5.9*, the capacitance is almost in a linear relationship with the strain in all five tests. Compared with the results in the tensile test, the change of the capacitance is much larger. Based on the average capacitances from the five tests, the changing rate can be calculated, which is approximately 0.146 pF per 10000 micro-strain.

However, from the results, it can be seen that there are evident errors in the test. The standard deviation at each strain condition is approximately 0.1, which is much larger than the standard deviation at the initial condition (which is only 0.0081). At the same strain condition, e.g. 2.35%, there is approximately 0.27 pF difference between test 1 and test 4. In test 3, the capacitance at strain of 6.54% is 10.5385 pF, which is larger than the capacitance at strain of 5.35% and 5.95% in test 2 (10.5655 pF and 10.48 pF, respectively). There are also unexpected decreases of the capacitance at strain of 4.13% in test 1 and at strain of 5.35% in test 5. Even for the initial value of the sensor, the difference is still considerable compared with the changing rate, the largest difference is 0.025 pF (from test 1 and test 2).

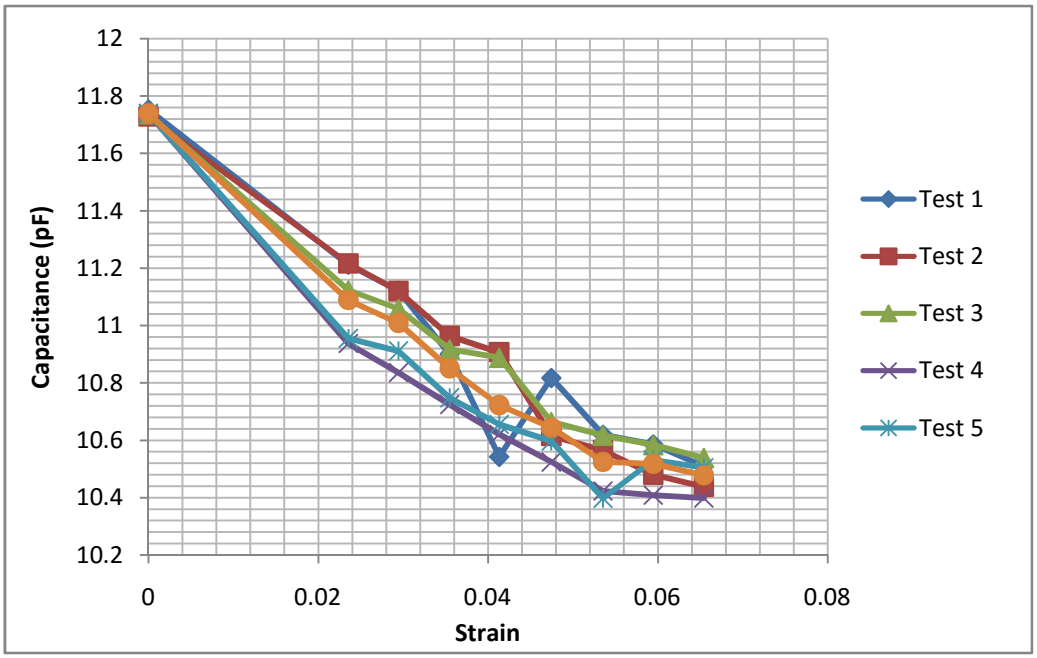

Figure 5.9 The diagram for the values of capacitance of the strain sensor in each bending test

It is inferred that operating the test manually is the main reason for causing the errors. The sensor had to be frequently switched to different layers of the rod to obtain different strain conditions manually and the sensor were connected to the WAYNE KERR analyser by wires, so the distance between the external connecting wires were changing in every measurement. Meanwhile, the capacitive sensor is very sensitive to the medium surrounded, which can cause a huge difference during manual measuring process. Any changes of the surrounding environment can cause a distinct change of the capacitance. As shown in *figure 5.10 (a)*, *(b)* and *(c)*, when a human finger gets close to the surface of the sensor, the capacitance was decreased from 11.0130 pF to 10.5965 pF. While when a 5 pence coin put over the surface of the senor, the capacitance was increased to 11.6355 pF.

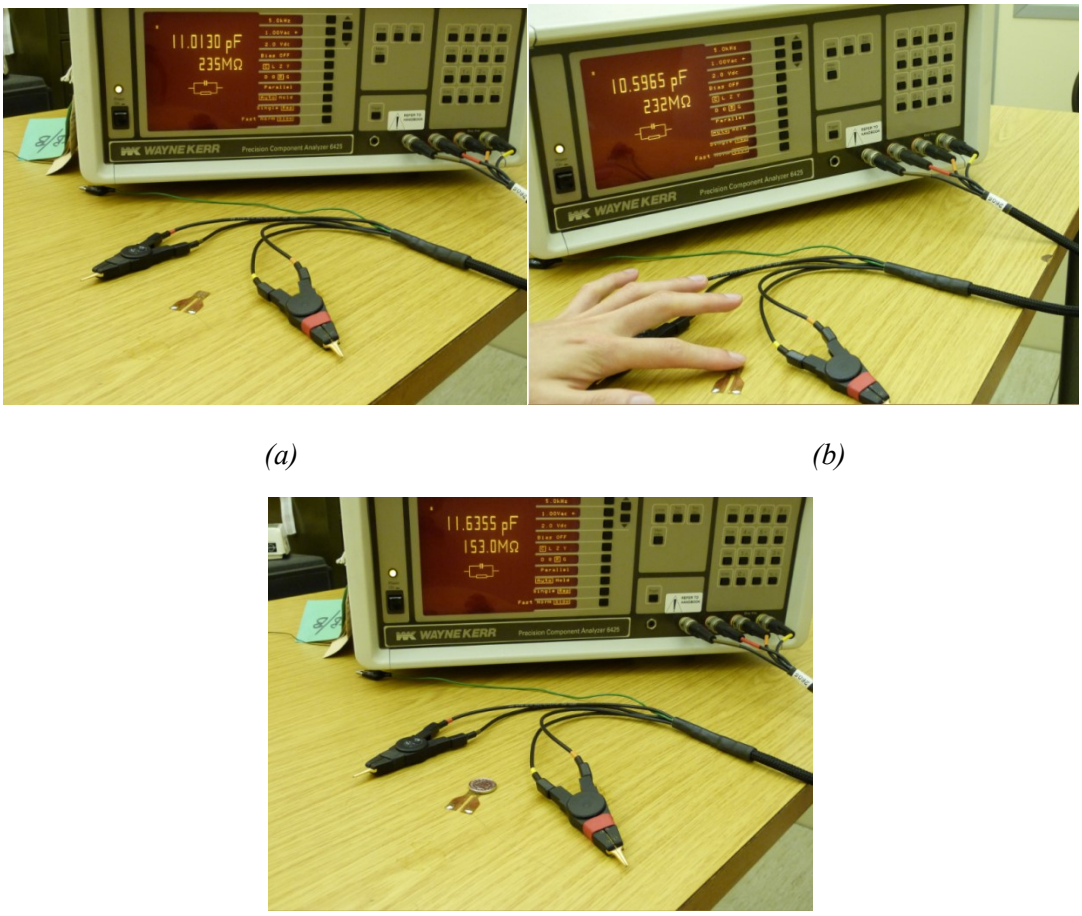

(a) *(b)*

(c)

Figure 5.10 The capacitance of the strain sensor without anything around (a), with a human finger upon (b) and with a 5 pence coin covered (c)[7]

Although the bending test can obtain some better results than that in the tensile test, there are still many defects. Apart from the errors in the test, this method cannot satisfy the measurements for a strain that is smaller than $\pm 1\%$. If the strain is 0.5%, from the equation *Eq* 5.4, the diameter of the rod will have to be approximately 230mm, while if the strain is 0.1%, the diameter will be over 1m. Additionally, similar with the tensile test, the bending test cannot give a compressive strain. So, an alternative test is still desired to fully calibrate the strain sensor.

[7] The sensor was connected to the WAYNE KERR analyser by single wires, which can hardly be seen from the figure.

5.3.3 Cantilever test

In the last two sections, tensile test and bending test were introduced. However, there are no stable measurements recording and both of them cannot give a small strain condition. So, a cantilever test that aims at stable measurements at small strain ($\pm 1\%$) was carried out.

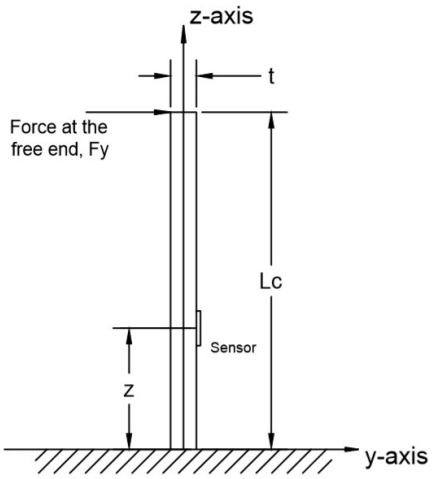

Figure 5.11 A schematic diagram for cantilever test for the strain sensor

As show in *figure 5.11*, one end of the cantilever is fixed. In *figure 5.11*, the z-axis is along the direction of the cantilever, y-axis is perpendicular to the z-axis and parallel with the paper and the x-axis is vertical to the yz-plane, which is vertical to the paper. The sensor is bonded on one side of the cantilever, and the distance between the bonding point and the fixed end is z. When a force $F = \begin{bmatrix} F_x \\ F_y \end{bmatrix}$ is applied to the free end of the cantilever, the surfaces of both sides of the cantilever will either in a compressed or stretched condition. From the Saint-Venant's bending theory, the stress at the sensor σ_z can be given by [12]:

$$\sigma_z = -\left(\frac{F_x}{I_y} \cdot x + \frac{F_y}{I_x} \cdot y\right)(l_c - z) \qquad Eq\ 5.5$$

where F_x and F_y are the forces in direction of x-axis and y-axis, I_X and I_y are the moments of inertia for the cantilever cross section for directions of x-axis and y-axis while x and y stand for a point (x, y) at the cantilever cross section, respectively. l_c is the length of

the cantilever.

If the force is only in y-axis direction, equation $Eq\ 5.5$ can be simplified:

$$\sigma_z = -\frac{F_y}{I_x} \cdot y \cdot (l_c - z) \qquad Eq\ 5.6$$

so, the strain at the sensor ε_z is given by:

$$\varepsilon_z = \frac{\sigma_z}{E_c} = -\frac{F_y}{E_c I_x} \cdot y \cdot (l_c - z) \qquad Eq\ 5.7$$

Compared with the force, the deflection in y-axis D_y is easier to be measured in the experiment, while D_y also has a relationship with the Young's modulus of the cantilever E_c and the moment of inertia I_x [13]:

$$D_y = \frac{F_y l_c^3}{3E_c I_x} \qquad Eq\ 5.8$$

then,

$$\frac{F_y}{E_c I_x} = \frac{3D_y}{l_c^3} \qquad Eq\ 5.9$$

So,

$$\varepsilon_z = -\frac{3D_y}{l_c^3} \cdot y \cdot (l_c - z) \qquad Eq\ 5.10$$

While for a sensor that is bonded on the surface of the cantilever, the value of y can be given by:

$$y = \pm\frac{t}{2} \qquad Eq\ 5.11$$

where t is the thickness of the cantilever. From *figure 5.11*, the sensor is positioned at right hand side, so:

$$y = \frac{t}{2} \qquad \text{Eq } 5.12$$

Hence,

$$\varepsilon_z = \mp\frac{3D_y}{l_c^3} \cdot \frac{t}{2} \cdot (l_c - z) \qquad Eq\ 5.13$$

when the deflection is from the left to the right, D_y will be positive, ε_z will be negative and the strain sensor is under a compressed condition while when the deflection is from the right to the left, D_y will be negative, ε_z will be positive and the strain sensor is under a tensile condition.

The deflection at the free end and the thickness of the cantilever have to be big enough to achieve the measuring range, which is approximately about -1% to 1% (-10000 micro-strain to 10000 micron strain). So, a flexible ruler that is made from ultra flexible polyvinyl chloride (PVC) with 2.23 mm thickness (which was measured by micro-calliper) was selected as the cantilever. Compared with normal materials that employed for cantilever, e.g. steel or aluminium, PVC is much easier to be bent and has a wider elastic region. Meanwhile, PVC is capable of being bonded with the strain sensor by using the adhesive bonding method introduced previously.

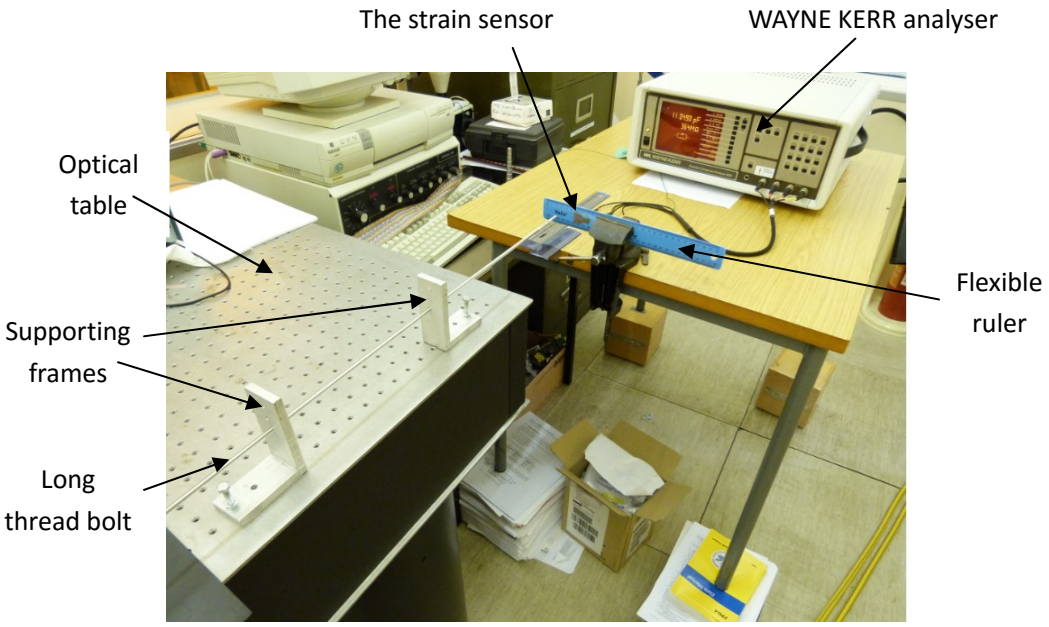

Figure 5.12 The experiment set up for cantilever test for the strain sensor

A long thread bolt was select as the bending force, and two aluminium frames for supporting and fix the bolt were machined while these two frames were fixed on the optical table by two M6 bolts, as shown in *figure 5.12*. The sensor was bonded on the flexible ruler by the silicone adhesive with primer NO 3 and connected out by two single wires, and the connecting wires were fixed either on the ruler or on the table to minimize the influence that might be brought by any movements of the wires. One end of the long bolt was pushing the free end of the cantilever by threading in from the other end. The deflection could be measured directly or was equivalent to the depth of the bolt threading in. The same with previous tests, the capacitance of the sensor was still measured by the WAYNE KERR analyser with the same set up. The distance between the fixed and free ends of the cantilever was 10.5 cm and the strain sensor was bonded to the point that was 2 cm away from the fixed end of the cantilever. The results of the experiments were given by *table 5.4*.

Table 5.4 The results of the cantilever test for the strain sensor

		Capacitance (pF)				
Deflection, D_y (cm)	**Micro-strain, ε_z**	**Test 1**	**Test 2**	**Test 3**	**Average**	**Standard Deviation**
4	-9824.43	11.1505	11.1495	11.1500	11.1500	0.0004
3.5	-8596.37	11.1455	11.1460	11.1430	11.1448	0.0013
3	-7368.32	11.1325	11.1375	11.1330	11.1343	0.0022
2.5	-6140.27	11.1200	11.1210	11.1220	11.1210	0.0008
2	-4912.21	11.1090	11.1085	11.1105	11.1093	0.0008
1.5	-3684.16	11.0970	11.0970	11.0980	11.0973	0.0005
1	-2456.11	11.0865	11.0860	11.0880	11.0868	0.0008
0.5	-1228.05	11.0760	11.0755	11.0765	11.0760	0.0004
0	0	11.0680	11.0675	11.0675	11.0677	0.0002
-0.5	1228.05	11.0580	11.0605	11.0620	11.0602	0.0016
-1	2456.11	11.0475	11.0475	11.0455	11.0468	0.0009
-1.5	3684.16	11.0390	11.0415	11.0395	11.0400	0.0011
-2	4912.21	11.0310	11.0345	11.0345	11.0333	0.0016
-2.5	6140.27	11.0275	11.0300	11.0300	11.0292	0.0012
-3	7368.32	11.0235	11.0265	11.0250	11.0250	0.0012
-3.5	8596.37	11.0160	11.0250	11.0200	11.0203	0.0037
-4	9824.43	11.0095	11.0200	11.0200	11.0165	0.0049

Based on the results in these three test, *figure 5.13 (a)* and *(b)* are also illustrated.

As the measurements were very close to each other in every strain condition, there were three instead of five tests carried out. Along with the increase of the strain from compressed condition to tensile condition, the capacitance is decreasing gradually and basically follows a linear relationship with the strain. Three straight lines are fitted to the average capacitance in *figure 5.13 (b)*.

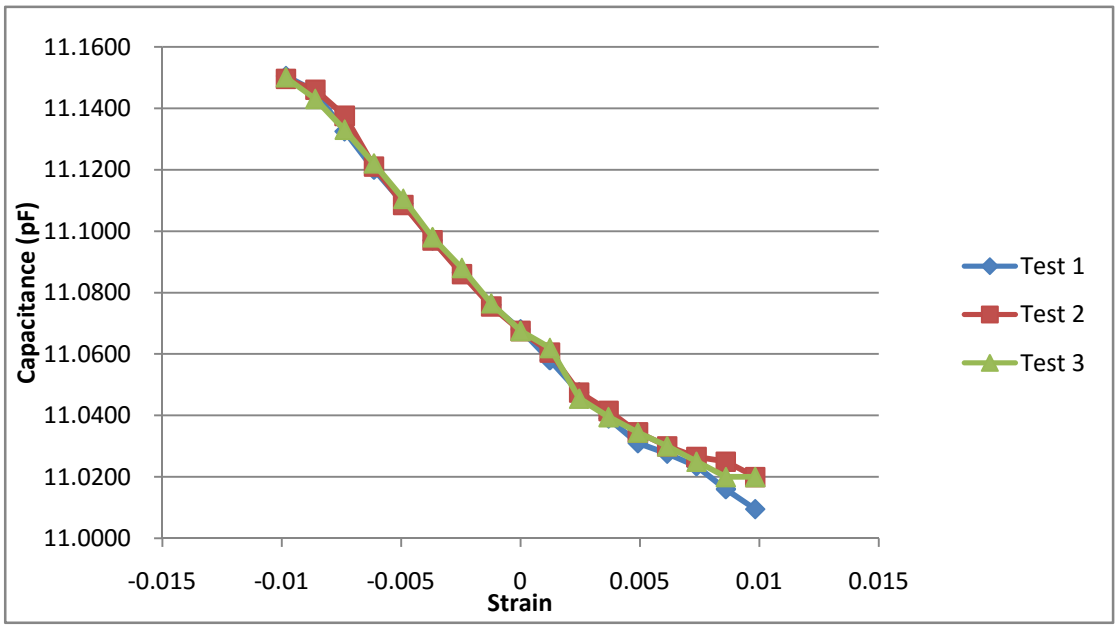

(a)

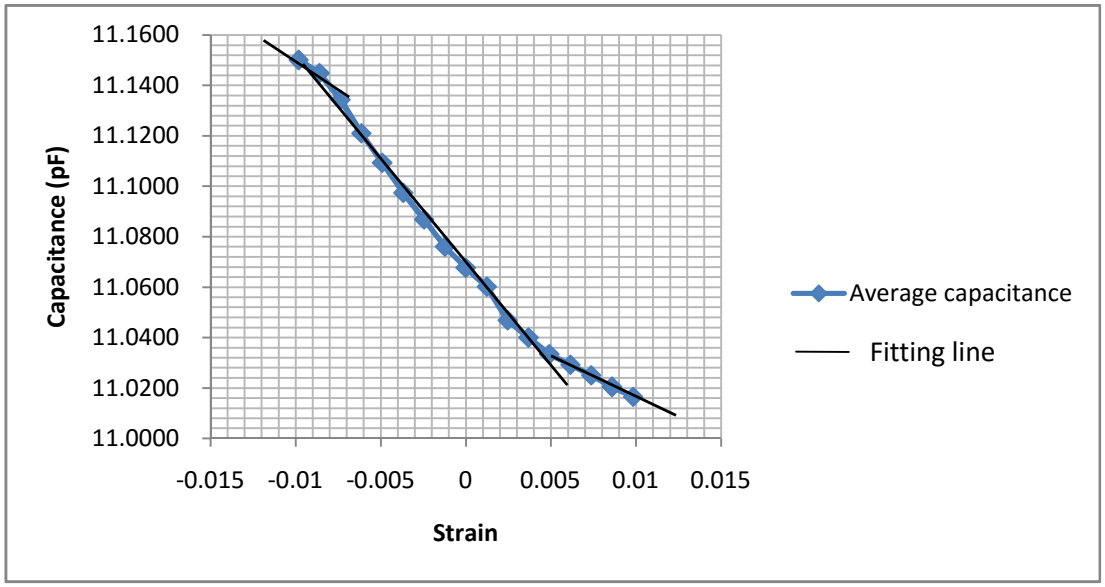

(b)

Figure 5.13 The diagram for the values of capacitance of the strain sensor in each cantilever test (a) and in average (b)

It can be seen that from the results in the three tests, the capacitance in each strain condition were close to each other and at initial point the capacitance in all the tests were basically the same. Most of the standard deviations are approximately 0.001, which means that compared with the tensile test and bending test, the cantilever test can give a more stable and reliable measurement.

However, there are some limitations for the cantilever test. It can be noticed that the capacitance chang is relatively smaller and has larger standard deviation at large deflection, e.g. in test 1, the difference of the capacitance at deflection of 4cm and 3.5cm was 0.005 pF while between deflection of 1.5cm and 1cm was 0.0105 pF. The standard deviation at deflection -4mm is 0.0049 while at deflection -1mm is only 0.0009. It probably was affected by the change of the strain condition. In fact, when the deflection was larger than 4 cm, the

long thread bolt could hardly apply a force that was only in y-axis direction due to the over-bended cantilever. This is also the reason for fitting three straight lines for the average capacitance. It is also believed that values in the middle of the table, which are at the deflection from 3 to -3 mm, are most reliable and the strain can be reflected by equation $Eq\ 5.13$ that given above factually. So, fitting line in the middle is selected to calculate the changing rate, which is 0.090 pF per 10000 micro-strain. While when the deflection is higher than 4mm, the actual strain at the strain sensor is no longer able to be calculated from the equation E*q 5.13*. Therefore, the cantilever test is not capable with any larger strain condition that is over $\pm 1\%$ except a thicker cantilever is found. However, it also can be found from the equation that the strain is in a linear relationship with the thickness of the cantilever, so if the thickness of the flexible ruler is doubled, which is 4.43 mm, the strain that can be achieved by this method will be approximately $\pm 2\%$.

5.3.4 The discussion on the results from tests, calculation and simulation

The changing rates from tensile test, bending test and cantilever test are 0.0127 pF, 0.146 pF and 0.090 pF per 10000 micro-strain, respectively. While based on the results from the calculation and simulation, the changing rate are 0.036 pF and 0.018 pF per 10000 micro-strain.

There are many factors that might cause the different results between tests, calculation and simulation. As mentioned in Section 5.3.1, due to the self-relaxing of the tyre rubber sample, it is difficult to obtain the actual strain information of the sample. The every strain condition

that calculated from the displacement of two clamps is in fact larger than the actual strain, which probably is the main reason for the low changing rate that obtained from the tensile test. While for the bending test, the manual operating measurement has already brought large errors to the experiment. Meanwhile, the force that wrapping the sensor around the aluminium rod also can influence the spacing in the sensor, which might expand the changing rate in the bending test as well.

Although the testing process of the cantilever test is stable, the result of the cantilever test is still different from the results from calculation and simulation. It is believed that the results acquired from the cantilever test are accurate and reliable. While in the calculation, the wires in the design were equivalent to the coplanar electrodes, although the assumption can match the linear-like relationship between the strain and the capacitance, it still can hardly describe the changing rate correctly, which is inferred to be the main reason for the difference between the test and calculation. Meanwhile, as mentioned in Section 3.3.3.3, limited by the memory of the computing, one side of the tyre rubber substrate was fixed, which resulted that the compressed/expanded gaps between the wires were not uniform, the wires that were closed to the fixed boundary moved little from the original position while the wires at the far-ends had distinguished movements. In a real strain condition, however, the spacing was compressed/expanded uniformly. In addition, in the cantilever test, the strain was generated by bending the flexible ruler and was different from the boundary conditions that was set as tensile or compression in the simulation, which also results the difference of the changing rate. Nonetheless, the calculation and simulation can still provide a linear-like relationship between

the capacitance of the sensor and the strain, which matches the results from the cantilever test.

5.3.5 The summary of the calibration methods

Tensile test, bending test and cantilever test were carried out to calibrate the strain sensor and the capacitance changing rates in each methods were also calculated. However, the results from tensile test and bending test were less reliable than that from cantilever test.

In tensile test, as a stretching substrate, the tyre rubber sample had an evident self-relaxing phenomenon, which had a significant effect on the strain behaviour of the sample during the test. Hence, the measurements in the test were smaller than the actual values. That is also the main reason for the low changing rate in the capacitance in this test method. A much larger capacitance changing rate was obtained in bending test. However, the unstable manual measuring process resulted many errors in the records. Additionally, in both tensile test and bending test, the capacitance changes in compressed condition could not be measured and it was also difficult to acquire the capacitance when the strain was smaller than $\pm 1\%$. While the cantilever test solved the problems that occurred in the tensile test and bend test and obtained reliable measurements. Although it could not manage to achieve any strain condition that is over $\pm 1\%$, the measurements at the small strain conditions were very stable.

The cantilever test succeeded in calibrating the strain sensor and the changing rate was approximately 0.090 pF per 10000 micro-strain. If the capacitance of the sensor can be measured up to 0.001 pF (which is 1 fF and can be achieved by the WAYNE KERR

analyser), the resolution of strain that can be measured will be 111 micro-strain. The tensile test and the bending test could not obtain meaningful results, but still showed that the capacitance of the sensor has a linear-like relationship with the strain and also proved that the strain sensor has the capacity of measuring large strain (up to 6% at least) and measuring in bending condition.

5.4 Conclusions

In this chapter, the experiments based on the fabricated strain sensor from Chapter 4 was presented. The adhesive bonding method between the sensor and tyre rubber was firstly investigated. While the commercial method for bonding the tyre rubbers and the traditional method for bonding silicone rubbers were not suitable for this case. It was finally found that a primer has to be employed for bonding PDMS and tyre rubber. So the final adhesive bonding method was determined as using the silicone adhesive from Smooth-on with the primer NO 3 from ACC-silicone.

The calibration of the senor was also presented. There were three calibration methods introduced, which were tensile test, bending test and cantilever test. Due to the stability in the measuring process, the cantilever test was the best calibration method for the strain sensor in the small strain range (from -1% to 1%). From Section 3.3.3, it was determined that the capacitance of the sensor varied almost linearly in accordance with the calculation and simulation results for the strain sensor. *Figure 5.13 (a)* generated from measurements in the cantilever test had the similar relationship, which proved the reliability of the calibration

method. From *figure 5.13 (b)* and calculation, the changing rate was approximately 0.090 pF. Although the tensile test and bending test could give less meaningful results due to the self-relaxing of the tyre rubber in the tensile test and manual operation in the bending test. It could also be concluded that the sensor is capable of measuring large strains (up to $\pm$6% at least) and measuring in a bending condition.

Reference

1. Wu, H., B. Huang, and R.N. Zare, *Construction of microfluidic chips using polydimethylsiloxane for adhesive bonding.* Lab on a Chip, 2005. **5**(12): p. 1393-1398.
2. Eddings, M.A., M.A. Johnson, and B.K. Gale, *Determining the optimal PDMS–PDMS bonding technique for microfluidic devices.* Journal of Micromechanics and Microengineering, 2008. **18**(6): p. 067001.
3. Satyanarayana, S., R.N. Karnik, and A. Majumdar, *Stamp-and-stick room-temperature bonding technique for microdevices.* Microelectromechanical Systems, Journal of, 2005. **14**(2): p. 392-399.
4. Rodgers, B. and W. Waddell, *14 - Tire Engineering*, in *Science and Technology of Rubber (Third Edition)*, J.E.M.E.R. Eirich, Editor. 2005, Academic Press: Burlington. p. 619-II.
5. *Chemical structure of styrene-butadiene rubber*. Available from: https://upload.wikimedia.org/wikipedia/commons/0/0e/SBRwithexplicitC.png.
6. *Chemical structure of natural rubber*. Available from: https://upload.wikimedia.org/wikipedia/commons/b/b2/PolyIsopreneCorrected.png.
7. *Chemical sturcture of Polybutadiene*. Available from: http://pslc.ws/macrog/pb.htm.
8. Hertz Jr, D.L., *Theory & practice of vulcanization.* Elastomerics, November, 1984.
9. Coran, A.Y., *7 - Vulcanization*, in *Science and Technology of Rubber (Third Edition)*, J.E.M.E.R. Eirich, Editor. 2005, Academic Press: Burlington. p. 321-366.
10. *F0-F Vulcanizing cement*. [cited 2015 Aug 19]; Available from:

http://www.rematiptop.com/part.php?pid=59&cid=7&sid=4.

11. Lötters, J., et al., *The mechanical properties of the rubber elastic polymer polydimethylsiloxane for sensor applications*. Journal of Micromechanics and Microengineering, 1997. **7**(3): p. 145.

12. Lurie, A. and A. Belyaev, *Theory of elasticity. Foundations of engineering mechanics.* Springer, Berlin. http:// link. springer. com/ book, 2005. **10**(1007): p. 978-3.

13. LD Landau, E.L., *Theory of Elasiticity 3rd Edition*. Course of Theoretical Physics Volume 7. Vol. 7. 1959: Insitude of Physical Problems, USSR Academy of Sciences, Moscow USSR.

Chapter Six.
Conclusions and Future Work

6.1 Conclusions

It has been found out that the friction between the tyre and road surfaces is the key physical quantity for improving the safety and manoeuvrability, developing the drive experience, increasing the tyre lifetime and controlling the fuel consumption of the vehicles. It was believed that the evaluation of the strain in the tyres can provide accurate and significant information for analyzing the friction, which makes the strain become a possible alternative parameter to be measured because of the difficulties for measuring the friction directly. The strain behaviour was studied and it was also found that finite element analysis was the most popular research method for investigating the strain in the tyres. Based on the information in FEA models, the sensing area, speed and range were determined. The literature review also presented most of strain sensing technologies and the sensors that were developed specially for the measuring the strain in tyres. However, the research on the tyre strain sensor was very limited and there was few development in recent years. A novel tyre strain sensor is still desired to be designed, which has the advantages of small stiffness, easy for installation and fabrication, capable of wireless transmitting and possible for introducing to mass production. Capacitive sensor was determined as the sensing technology after studying the pros and cons of previous research. Additionally, an investigation on a compliant material, polydimethylsiloxane (PDMS), was also presented as the last part of the literature review.

In the next chapter, three designs that shared the same design concept were carried out, which

were interdigital capacitor design, coplanar capacitor design and bond wire capacitor design. MATLAB and COMSOL Multiphysics were employed to calculate and simulate the initial capacitance of the designs and sensitivity with respect to the strain. It was found that the bond wire capacitor design could provide a reasonable capacitance and sensitivity. Meanwhile, the bond wire structure minimized the stiffness of the sensor and obtained a linear-like relationship with the strain from compressed to tensile condition.

After testing the limits of the wet etching process and laser machining process on the flexible PCB, these two machining methods were hybridized to achieve the small dimensions in the copper pattern for the wire bonding process. Some wire bonding trials were also made to investigate the parallelism of the wire arrays in different bond heights and bond lengths. For the stability of the fabrication, the bond wire capacitor design was also developed. PDMS was employed for embedding and packaging the bond wire structure, which can not only provide a small stiffness compared to the tyre rubber but also protect the wires from potential damages.

The adhesive bonding method between inner tyre tread and sensor surfaces was critical for measuring the strain in tyres. The adhesive should have similar or less Young's modulus compared with tyre rubber and PDMS to ensure that the strain in the tyre can be detected by the sensor without any disturbance. The commercial adhesive, e.g. cyanoacrylate, which is also known as superglue, is not suitable for this case due to the high stiffness after curing. Oxygen plasma treatment might be a solution for bonding tyre rubber and PDMS surfaces together, however, considering the cost of the process and the difficulties in operation for the

tyres, it will not be a good option. Meanwhile, the common adhesive bonding methods that are employing in tyre rubber industry and PDMS applications were tried but could not create a strong bond. It was finally found out that a primer had to be employed due to the huge chemical and physical differences between these two bonding surfaces. Silicone adhesive from Smooth-on with Primer NO3 from ACC-silicones was selected as the final adhesive bonding method.

There were three testing methods carried out to measure and calibrate the strain sensor. In which, tensile test and bending test were unable to acquire stable measurements. In addition, the compressed strain condition and a small range strain (less than $\pm 1\%$) could hardly achieve by these two methods. Cantilever test was found to be the best method to calibrate the strain sensor, which could provide the best stability of the measurements. However, limited by over-bended situation of the cantilever, this method was not suitable for calibrating the strain condition that was higher than $\pm 1\%$. It was estimated that the calibration range could be doubled if a cantilever with doubled thickness was found. From the tests, it could be found that the strain sensor was capable of measuring the strain of a flexible substrate and had high flexibility during the measurements.

6.2 Specific outcomes of the study

A novel bond wire capacitive strain sensor with a measuring range up to at least $\pm 6\%$ and 111 micro-strain (0.01%) resolution that can measure the strain in tyres without any influence and disturbance to the sensing area was designed and fabricated. The bond wire technology

was first developed into sensor fabrication system in this research. With 3000 micron bond length and 500 micron bond height, an aluminium wire array with 50 loops that has high parallelism was fabricated, which generated 49 pair of electrodes for the capacitive strain sensor. Laser machining hybridized with wet etching process was also a new attempt to fabricate patterns with dimension around 40-50 microns on the flexible PCB. Moreover, the whole fabrication process also has a possibility to be introduced to industry for mass production. The adhesive bonding method for the surfaces of the tyre and PDMS based device was first investigated and it was proved that employing the silicone adhesive from Smooth-on with Primer NO3 from ACC-silicones could achieve the best bonding strength. In addition, it was found that the cantilever test with a flexible beam was an alternative calibration method instead of the tensile test due to the self relaxing phenomenon for the soft substrate of the latter, which could bring more stable and reliable measurements.

6.3 Future work

Although the strain sensor has been designed and developed from the previous research and it is capable of measuring the strain in tyres, there are still some parts of the research that needs to be improved.

It was found that the results from the calculation and simulation can describe the trend of the changing of the capacitance with respect to strains, but there was an evident difference from the measurements in the cantilever test. The coplanar structure was equivalent to bond wire structure in the calculation, which could not describe the actual capacitive situation precisely.

Meanwhile, the multiple wires in the design brought many difficulties in simulation. Limited by the memory and computing speed of PC, the model and boundary conditions had to be simplified as much as possible, so the accuracy of the simulation was more or less affected. Therefore, it is still expected to find a more appropriate theoretical model to describe the bond wire structure properly and a super computer is desired to be employed to fully simulate the behaviour of the strain sensor in a tyre.

In the fabrication process, although the laser machining process and wet etching process are both employed in industry nowadays. However, the hybrid of both process for fabricating the copper pattern appears to be complicated. Choosing one of the process to finish the copper pattern will not only simplify the fabrication process but also control the cost. To achieve the features in the copper pattern, better wet etching process for multiple gaps in different dimensions needs to be developed if wet etching process is selected. Alternatively, if the laser machining is selected, controlling the machining depth in the process is becoming desired, which might be achieved by investigating different combinations of the strength of the laser and machining layers.

As mentioned in the Chapter five, the cantilever test was the best method for calibrating the strain sensor but it could hardly achieve any strain condition that was larger than $\pm 1\%$. A flexible substrate with larger thickness can be an solution if the measuring range of the strain sensor needs to be determined. Meanwhile, although it has been proved that the strain sensor is capable of measuring the strain of a soft substrate, it has to be applied on the inner surface

of a tyre to be tested in a real tyre strain system. The static test will be the first step and the dynamic test will also be followed. In the static test the strain sensor will be positioned in different places along the contact patch, different loads will be applied to the tyre to obtained different strain conditions of the contact patch. In the dynamics test, the sensor will have to be enclosed in a tyre wheel, which means the strain sensor has to be connected to the external system wirelessly. Hence, a wireless transmitting method is desired to be designed.

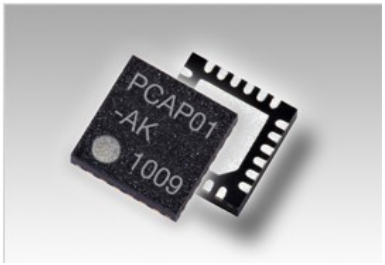

(a)

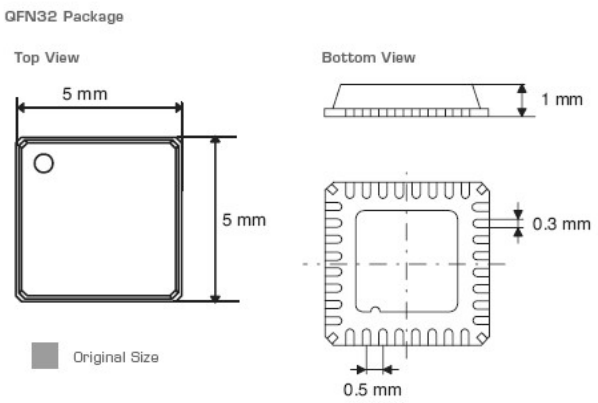

(b)

Figure 6.1 The picture (a) and the package outline (b) of the PICOCAP chip

There are many possibilities and challenges to develop the wireless transmitting system. The signal-to-noise ratio (SNR), the transmitting distance and speed, the power supporting method and the cost of the wireless transmitting system are all the aspects that have to be considered. Radio frequency identification (RFID) technology is one of the solution, which has the

advantages of cheap and powerless, while the transmitting distance and the SNR might be the potential problems. In addition, it could be an alternative solution if a system converts the capacitance into a digital signal and transmits the digital signal wirelessly. A conversion chip in a very small scale (5×5 mm) called PICOCAP has been found in the market [1], as shown in *figure 6.1*. It claims that the chip is capable of converting the capacitance that in a resolution of fF, which means that the chip can be totally integrated with the strain sensor. However, an appropriate powering method has to be found to power the chip, which because a normal battery cannot support the chip for working constantly in a long duration inside a tyre wheel.

Once the improvements that were introduced previously can be achieved, a complete tyre strain sensing system can be developed. The strain sensor with both theoretical and practical supports can measure the strain in the tyres in a range of at least ±60000 micro-strain (6%) with a resolution of 111 micro-strain. While the stain information can be transmitted wirelessly from the inside of a enclosed tyre to the external systems for analyzing the forces between surfaces of the tyre and road. What is also worth mentioning is, the fabrication process of the strain sensor and the transmitting system have the possibility to be industrialized to mass production in a reasonable cost.

Reference

1. *PICOCAP - The most flexible solution in direct Capacitance-to-Digital Conversion*. Available from: http://www.pmt-fl.com/picocap/picocap-capacitance-measurement.php.

Appendix I：Standard format for the pneumatic tyres

There is a standard format for the pneumatic tyres. In the form 175/70 R14, 175 means the width of the tyre is 175mm, the aspect ratio is 70%, the tyre is in a radial construction and the rim diameter is 14 inches, which is also shown in the figure below.

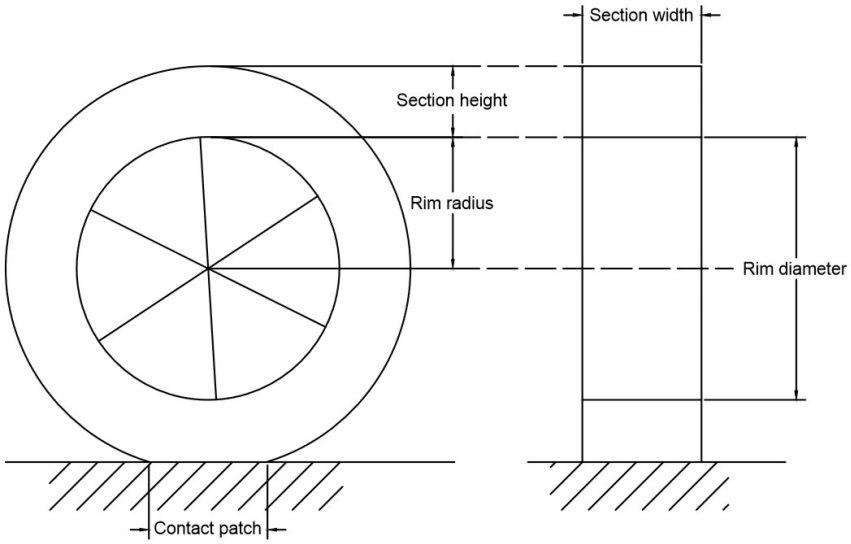

Figure I A schematic diagram to explain the standard format for the pneumatic tyres

Where the aspect ratio is given by:

$$Aspect\ ratio = \frac{Section\ height}{Section\ width} \times 100\%$$

Hence, the radius of the tyre 175/70 R14 can be calculated:

$$The\ diameter\ of\ the\ tyre = rim\ diameter + 2 \times section\ width \times aspect\ ratio$$

$$= 600.6\ mm$$

Hence, if the belt angle is $\pm 20°$, the length of the contact patch is given by:

$$The\ length\ of\ the\ contact\ patch = 2 \times The\ radius\ of\ the\ tyre \times sin20° \approx 205\ mm$$

Appendix II: MATLAB code for the interdigital capacitor design

The MATLAB code for calculating the relationship between the capacitance of the interdigital capacitor design and the strain is shown below:

```
%%The calculation of interdigital capacitor design
clear
c=10*10^-3; a=0.3*10^-3; d=1.2*10^-3; f=1*10^-3; n=5; sig=2.75;
sig0=8.854*10^-12
x=[-0.3*10^-3:0.001*10^-3:0.3*10^-3];
y=[-0.28*10^-3:0.001*10^-3:0.28*10^-3];
C1=sig*sig0*(c*d*n./(a+x)+c*d*(n-1)./(a-x)+f*d*(2*n-2)./a);
C2=sig*sig0*((c-y)*d*((2*n-1)./a)+f*d*(n-1)./(a+y)+f*d*(n-1)./(a-y));
StrainX=x./(2*n*f+(2*n-1)*a);
StrainY=y./(c+2*a+2*f);
figure
plot(StrainX,C1)
grid minor
xlabel('Strain in x direction');
ylabel('Capacitance(pF)');
figure
plot(StrainY,C2)
grid minor
xlabel('Strain in y direction')
ylabel('Capacitance(pF)')
```

Appendix III: MATLAB code for the coplanar capacitor design

The MATLAB code for calculating the relationship between the capacitance of the coplanar capacitor design and the strain is shown below:

```
%%The calculation of the coplanar capacitor design
clear
s=150; l=1000; StrainX=-0.03:0.0001:0.03; sig0=8.854187817*10^-12;
sig=2.75; c=10*10^-3;n=5
x=StrainX*s
k=(s+x)./(s+2*l+x)
if k<0.7
    F=pi^-1*log(2*(1+(1-k.^2).^0.25)./(1-(1-k.^2).^0.25));
else
    F=pi./log(2*(1+k.^0.5)./(1-k.^0.5));
end
C=(2*n-1)*sig0*sig*F*c;
figure
plot (StrainX,C)
grid minor
xlabel('Strain in x direction')
ylabel('Capacitance(pF)')
```